ABSTRACT

NEUTRON-NUCLEUS TOTAL CROSS SECTIONS
IN THE 10 TO 30 GEV/c MOMENTUM RANGE

by

Thomas Patrick McCorriston Jr.

Co-chairmen: Lawrence W. Jones and Michael J. Longo

The total nuclear cross sections for neutrons on protons, carbon, copper and lead were measured at mean neutron momenta of 11.8 GeV/c, 16.9 GeV/c and 25.4 GeV/c. Also measured were the total cross sections for neutrons on deuterium at 16.9 GeV/c and on beryllium, aluminum, cadmium and tungsten at 25.4 GeV/c. The experiment was conducted at the Alternating Gradient Synchrotron at Brookhaven National Laboratory. A total absortion spectrometer was used to select only the most energetic neutrons from the incident spectra.

The measured nuclear cross sections are compared to the predictions of the Glauber multiple scattering model and are found to agree. A comparison of the momentum dependence of the measured cross sections with that predicted by two models of the inelastic shadow effect shows that this effect is too small to be resolved at the energies at which this experiment was performed.

UM-HE 72-11

NEUTRON-NUCLEUS TOTAL CROSS SECTIONS IN THE 10 TO 30 GEV/c MOMENTUM RANGE

by
Thomas Patrick McCorriston Jr.

A dissertation submitted in partial fulfillment
of the requirements for the degree of
Doctor of Philosophy
(Physics)
in The University of Michigan
1972

Doctoral Committee:

Professor Lawrence W. Jones, Co-Chairman
Professor Michael J. Longo, Co-Chairman
Professor David R. Bach
Assistant Professor Frank S. Henyey
Professor Oliver E. Overseth

ACKNOWLEDGEMENTS

I am very pleased to have this opportunity to thank the people who have contributed so much to both the performance of this experiment and to my graduate education.

I have been doubly fortunate in having two admirable men as my thesis advisors, Michael Longo and Lawrence Jones. Aside from being grateful to them for having me as a student and teaching me a great deal, I would also thank them for their understanding, personal encouragement and willingness to stand up for me at those times when I would otherwise have despaired of ever becoming a decent physicist.

To three others who helped bear the burden of my thesis experiment I also give my thanks: to Chris Burch for working long hours and for being an indian when everybody else was a chief; to Smith Powell for the same first reason and for his general good humor; and to Everett Parker for helping to get the experiment started while trying also to settle into a new home, a new job and parenthood.

There are many people on the AGS staff to whom I am grateful. Chief among them is Jack Detweiler who was liaison engineer for this experiment. I must also thank J. W. Glenn for his expertise in changing the AGS energy for our low energy running.

My thanks also go to Orman Haas and Don O'Brien for helping to set up the experiment, to Jim Pluta for build-

ing some of the equipment on very short notice, to Mike Davis for helping with the surveying, and to Michael Kreisler for lobbying with the AGS administration and staff on behalf of this experiment.

TABLE OF CONTENTS

LIST OF TABLES

LIST OF FIGURES

CHAPTER I

INTRODUCTION

A. OBJECTIVES

We sought in the experiment described in this thesis to determine the total nuclear cross sections for neutrons on various nuclei at energies available at the Brookhaven Alternating Gradient Synchrotron (AGS). In addition to determining the dependence of these cross sections on atomic mass number, we were particularly interested in studying their energy dependence to see: 1) whether there were truly large decreases in the heavy element cross sections at high energies as had been reported;[1] and 2) whether the neutron-proton total cross section departed from equality with the proton-proton total cross section at AGS energies as had been suggested by previous data.[2]

B. THE TRANSMISSION TECHNIQUE OF MEASURING TOTAL CROSS SECTIONS

In this experiment we employed the traditional transmission technique for measuring total cross sections. In Figure 1 we show a schematic layout of a transmission experiment. For the present let us assume we are measuring the total cross section for a charged particle and ignore those parts of the figure which refer to neutral particles. There are three basic components to the experiment: 1) a device to monitor the number of particles in the beam; 2)

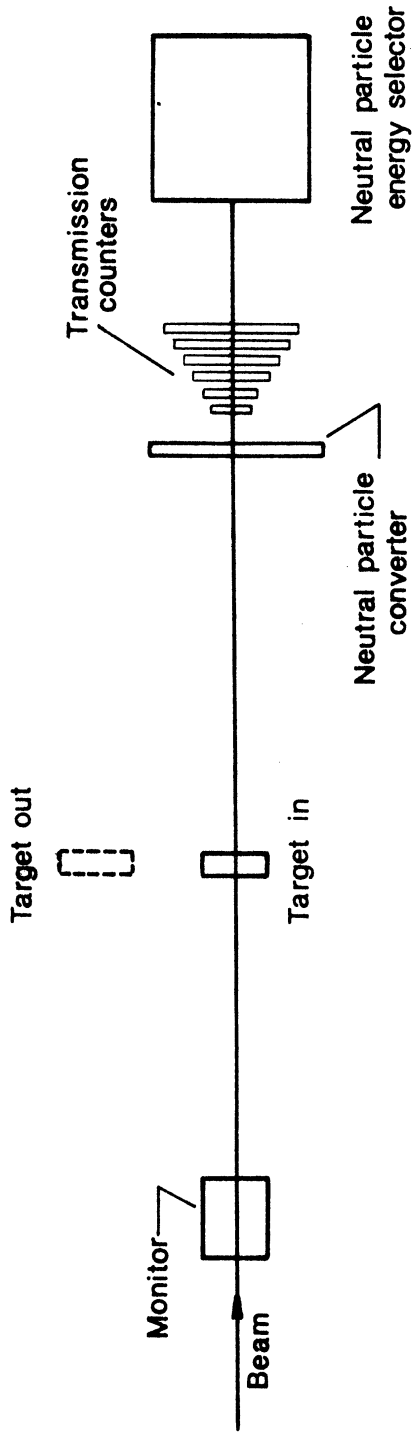

Fig. 1.--Typical transmission experiment layout

a target to be studied which attenuates the beam; and 3) a series of scintillation counters, usually circular, called "transmission counters". The target, made of the material on which the incident particle's total cross section is to be determined, is moved out of the beam for measurement of the unattenuated flux of particles incident on the transmission counters. These counters, which we assume to be circular, are of several radii. The radius of the smallest counter is large enough so that the entire unscattered beam is seen by that counter.

The apparent cross section--called the partial cross section--measured by a transmission counter depends on the solid angle, $\Delta\Omega$, subtended at the target by the counter. The partial cross section, $\sigma(\Delta\Omega)$, is given by

$$\sigma(\Delta\Omega) = -(1/nx)\ln[I(\Delta\Omega)/I_o],$$

where nx is the number of scatterers per unit area in the target, and $I(\Delta\Omega)/I_o$ is the fraction of the beam transmitted through the target for a given value of $\Delta\Omega$. The partial cross section is expected to vary with $\Delta\Omega$ roughly as indicated by the solid curve in Figure 2. This variation can be understood when one realizes that the target not only absorbs but also scatters the incident beam. For charged particles (and neutral particles with a nonzero magnetic moment) $\sigma(\Delta\Omega)$ turns sharply upward at small solid angles ($\Delta\Omega \lesssim \Delta\Omega_a$) in Figure 2 because of Coulomb scattering of the otherwise transmitted fraction of the beam. Were

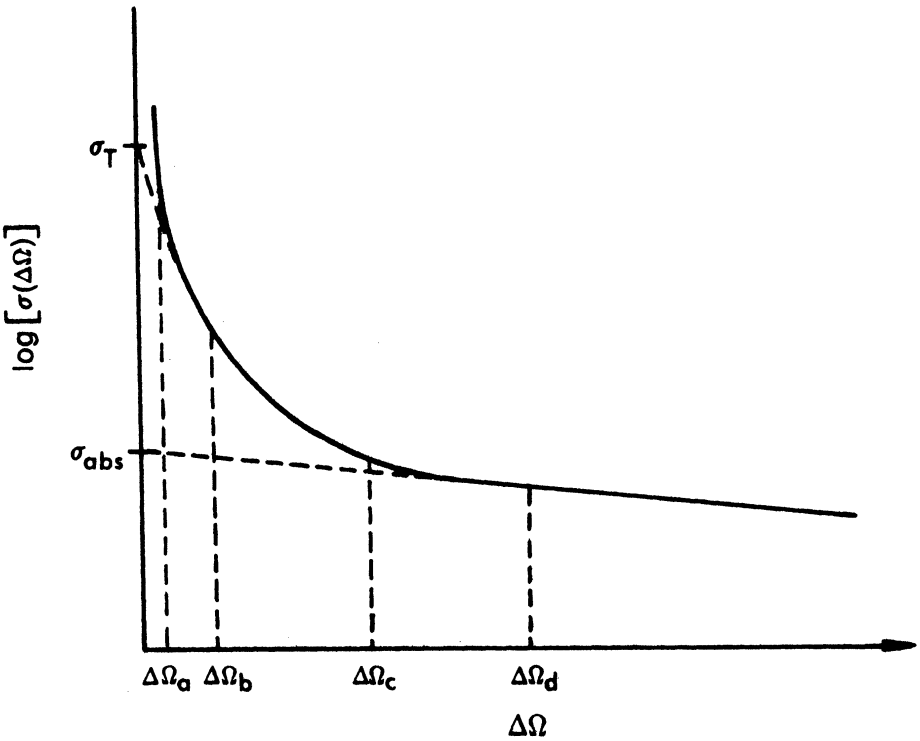

Fig. 2.--Expected variation of the partial cross section with solid angle

the Coulomb force absent, $\sigma(\Delta\Omega)$ would intersect the ordinate at the total cross section, σ_T. For counters of large enough solid angles ($\gtrsim \Delta\Omega_b$ in Figure 2) most of the Coulomb-scattered particles are collected. Nuclear scattering causes the partial cross section measured by a counter to be less than the total cross section, since by collecting such scattered particles a counter is collecting more than just the transmitted fraction of the beam. The nuclear scattering is of two kinds, elastic and inelastic. At $\Delta\Omega=0$ the differential elastic cross section is larger than the differential inelastic cross section. However, the elastic cross section drops much more rapidly with increasing solid angle than does the inelastic cross section. Eventually the latter becomes dominant. In Figure 2 $\Delta\Omega_b \lesssim \Delta\Omega \lesssim \Delta\Omega_c$ is the region where the slope of $\sigma(\Delta\Omega)$ versus $\Delta\Omega$ is determined principally by elastic scattering.

An experiment in which the transmission counters cover solid angles such that $\sigma(\Delta\Omega) \approx \sigma_T$ is said to be a "good geometry" experiment. With such an arrangement an extrapolation to "zero solid angle" of the set of partial cross sections--after Coulomb contributions are removed--yields an accurate measurement of the total nuclear cross section. If the set of solid angles covered by the counters falls in the region $\Delta\Omega \gtrsim \Delta\Omega_d$ of Figure 2, the experiment is said to be in "poor geometry". In this case extrapolation to zero solid angle provides not the total cross section but the inelastic or absorption cross section,

σ_{abs}.

For neutral particles the basic method is altered somewhat. One places some material in the beam before the transmission counters, as shown in Figure 2, to convert a fraction of the neutral particles to charged ones for detection by the counters. At high energies the shower of particles from a conversion usually goes along the direction of the incident neutral particle. The angular information is thereby preserved.

C. NEUTRON ENERGY DETERMINATION

In both charged particle and neutral particle transmission experiments one starts out with a beam of particles whose energies cover a wide range. This "secondary" beam is obtained by letting an accelerator's primary beam strike a "production" target. An example of a neutron spectrum so produced is shown in Figure A.1 of Appendix A. A secondary proton spectrum should look much the same except for being a little more abundant at the high momentum end. (For an atlas of secondary particle spectra see reference 3.) In the case of charged particles, selection from the secondary spectrum of particles with energies falling within a narrow range is readily and precisely accomplished with magnets. For the case of neutral particles the energy selection process is much cruder. We will talk about neutrons in particular at high energies, which we arbitrarily take to be greater than 1 GeV/c.

One method of neutron energy determination recently employed in two experiments[4,5] has made use of time-of-flight measurements between the production targets and the transmission counters. Such a method, however, is limited to accelerators such as the Stanford Linear Accelerator or the Princeton-Pennsylvania Accelerator where the primary beam strikes the production target in bursts of short duration ($\lesssim$ 1 nanosecond) with intervals between bursts long ($\sim$60 nanoseconds) compared with the burst width. A range requirement in an absorber was also used to discriminate against slow neutrons which arrived at the transmission counters at the same time as fast neutrons from the next burst.

For accelerators, such as the AGS, which have much higher duty cycles, it is not feasible to employ the method described in the last paragraph. What has been most often done is to try to reject neutrons below a certain energy, E_{min}, so that a neutron must have an energy lying in a band between E_{min} and E_{max}, the primary particle's energy. At momenta of about 1 to 2 GeV/c some experimenters have required the neutrons to have a minimum range in an absorber placed after the transmission counters.[6,7,8] At higher energies most groups have employed detectors in which the neutron interacts inelastically, creating a shower of charged particles, which are "counted" by the detector. The higher the energy of the incident neutron, the larger the number of charged particles that should be produced

eventually in the succeeding generations of showers in the detector. For example, Pantuev et al.[9] used a lead glass Cerenkov counter preceded by a block of aluminum in which a predominantly pionic shower was initiated. About a third of the pions produced in such a process could be expected to be neutral. The π^0 decay photons then produced electron pairs in the lead glass Cerenkov counter. The number of Cerenkov photons radiated by these electrons was roughly proportional to the energy of the incident neutron. Thus those neutrons whose energy release in the Cerenkov counter was below a certain mimimum could be rejected.

The energy selecting device we used was also of the type in which the neutron gave up its energy to the detector. The device consisted of plastic scintillators interleaved with iron plates. Of its exact construction we will say more in Chapter III. Just as in the device described in the last paragraph, most of the incident neutron's energy was eventually dissipated through electromagnetic showers in the iron and in the scintillator. It was expected that the number of photons produced in the scintillator would be roughly proportional to the incident neutron's energy.[10] The height of a voltage pulse from a phototube viewing the scintillator would, therefore, also be approximately proportional to the incoming particle's energy. Thus neutrons below a certain minimum energy could be rejected by requiring the pulse height to exceed a certain threshold. Such a device as we have just described has

been used in several neutron total cross section experiments in the last few years.[1,2,4,11-16]

In practice the devices we have described in the last two paragraphs cannot determine the incident neutron's energy exactly. They do not have infinitely good resolution. Thus some low energy neutrons will not be rejected, while some high energy ones will be. The energy resolution of the detector we used will be discussed in Appendix A.

D. SUMMARY OF PREVIOUS RESULTS

The proton-proton total cross section has been measured with good precision ($\lesssim 0.5\%$) from 1 GeV/c to 60 GeV/c with generally good agreement among the different experiments.[17-26] The total cross section for protons on deuterium has also been measured over the same range of momenta.[17,19,20,27] The only significant disagreement among the various sets of data on the proton-deuteron cross section occurs near 20 GeV/c where the data of Galbraith *et al.*[19] differs by more than the statistical errors from the data of Denisov *et al.*[20]

The number of neutron-proton total cross section data points reported in the literature has more than doubled in the last two years, so that the momentum range from 1 GeV/c to 60 GeV/c has been fairly well explored.[2,6-9,12,13,15,20,29] The data on the neutron-deuteron total cross section is still rather sparse, however, with only 10 data

points above 900 GeV/c.[2,8,12,15,17,29-31]

The total cross sections for nucleons on heavy elements have not been so thoroughly measured as the nucleon-nucleon cross sections. Only for a few elements--beryllium, carbon, aluminum, copper and lead--is the momentum range from 1 GeV/c to 27 GeV/c reasonably well covered.[1,4,6-8,11,14,16,21,24,30-33] Most of the data above 5 GeV/c have been reported in only the last few years. The data of Engler et al.[14] at momenta of 8, 11, 14 and 21 GeV/c were reported only after our experiment was completed. The measurements of Pantuev et al.[33] at 9.2 GeV/c, Atkinson et al.[32] at 5.8 GeV/c and Jones et al. at 27 GeV/c disagree with the trends indicated by the other data.

Graphs of the data we have just discussed as well as of our results will be presented in Chapter V.

CHAPTER II

THEORY

A. INTRODUCTION

In this section we will consider some recent theoretical work on total cross sections. Principally, we will look at the Glauber multiple scattering formulation, some "optical models", and the effect of intermediate inelastic states on the total cross section.

In general, the models we examine calculate the elastic scattering amplitude. The total cross section is then obtained via the optical theorem. Throughout we will work in the LAB frame and use amplitudes, F, normalized such that

$$\frac{d\sigma}{d|t|} = \frac{\pi}{p_{LAB}^2} F(t)F^*(t) \qquad \text{(II.1)}$$

where t is the square of the four momentum transfer to the target and p_{LAB} is the momentum of the incident particle in the laboratory frame. The optical theorem then has the form

$$\sigma_T = \frac{4\pi}{p_{LAB}} \mathrm{Im}F_{el}(0) \qquad \text{(II.2)}$$

Here and in what follows, we use the convention that $h/2\pi = 1$ and $c = 1$. The subscript "T" means total, and "el", elastic.

B. GLAUBER THEORY

The amplitude for scattering an incident hadron by a nucleus of mass number A as given by the Glauber theory[35,36] is

$$F_{fi}(q) = \int d^2b\Big\{e^{i\vec{q}\cdot\vec{b}}\int \varkappa_f^*(\vec{\xi}_1,\vec{\xi}_2,\ldots,\vec{\xi}_A)\Big[\exp\Big(i\sum_{j=1}^{A}\chi_j(\vec{b}-\vec{s}_j)\Big)-1\Big]$$

$$\times\varkappa_i(\vec{\xi}_1,\vec{\xi}_2,\ldots,\vec{\xi}_A)d\vec{\xi}_1 d\vec{\xi}_2\cdots d\vec{\xi}_A\Big\}[p/(2\pi i)] \qquad \text{(II.3)}$$

where b is the impact parameter, $\vec{q}$ is the three momentum transfer to the target nucleus in the laboratory, and $\varkappa_f(\vec{\xi}_1,\vec{\xi}_2,\ldots,\vec{\xi}_A)$ and $\varkappa_i(\vec{\xi}_1,\vec{\xi}_2,\ldots,\vec{\xi}_A)$ are respectively the final and initial state wave functions of the nucleus whose constituent nucleons have coordinates $\vec{\xi}_1,\vec{\xi}_2,\ldots,\vec{\xi}_A$. The $\vec{s}_j$ are the components of the $\vec{\xi}_j$ transverse to the beam direction. The phase shift functions $\chi_j(\vec{b}_j-\vec{s}_j)$ are related to the Fourier transforms of the hadron-nucleon scattering amplitudes, $f_j(\vec{q})$, by

$$1-\exp[i\chi_j(\vec{b})] = (1/2\pi ip)\int e^{-i\vec{q}\cdot\vec{b}}f_j(q)d^2q \qquad \text{(II.4)}$$

so that (II.3) becomes

$$F_{fi}(\vec{q}) = (ip/2\pi)\int d^2b\Big\{e^{i\vec{q}\cdot\vec{b}}\int \varkappa_f^*(\xi_1,\xi_2,\ldots,\xi_A)\Big\{1-\prod_{j=1}^{A}\Big[1-(2\pi ip)^{-1}$$

$$\times\int e^{-i\vec{q}'\cdot(\vec{b}-\vec{s}_j)}f_j(\vec{q}')d^2(q')\Big]\Big\}\varkappa_i(\vec{\xi}_1,\vec{\xi}_2,\ldots,\vec{\xi}_A)$$

$$\times d\xi_1 d\xi_2\cdots d\xi_A\Big\}. \qquad \text{(II.5)}$$

To get the total cross section we use the optical theorem and obtain

$$\sigma_T = +2\mathrm{Re}\int d^2b\Big\{1-\prod_{j=1}^{A}\Big[1-(2\pi ip)^{-1}\int e^{-i\vec{q}\cdot(\vec{b}-\vec{s}_j)}f_j(\vec{q})d^2q\Big]$$

$$\times|\varkappa_i(\vec{\xi}_1,\vec{\xi}_2,\ldots,\vec{\xi}_A)|^2 d\vec{\xi}_1 d\vec{\xi}_2\cdots d\vec{\xi}_A\Big\}. \qquad \text{(II.6)}$$

Thus the theory requires as input the hadron-proton and the hadron-neutron scattering amplitudes, and the absolute value of the ground state wave function of the

nucleus. Franco[37] and Czyż and Lesniak[38] make the simplifying assumption that the ground state wave function is a simple product of single particle wave functions, and that all of the single particle densities, $\rho_j(\vec{\xi}_j)$, are equal; i.e.,

$$|\varkappa_i(\vec{\xi}_1,\vec{\xi}_2,\ldots,\vec{\xi}_A)|^2 = \prod_{j=1}^{A}\rho_j(\vec{\xi}_j) = \prod_{j=1}^{A}\rho(\vec{\xi}_j). \qquad \text{(II.7)}$$

(We reserve until Section E a discussion of errors introduced here by ignoring correlations in the target nucleon positions.) These authors further suggest that one take the hadron-neutron and hadron-proton amplitudes to be equal, and assume that the density functions are spherically symmetric. We then obtain from (II.6)

$$\sigma_T = 4\pi \mathrm{Re}\int_0^\infty bdb\left\{1-\left[1-(1/ip)\int_0^\infty J_0(qb)f(q)S(q)qdq\right]^A\right\}, \qquad \text{(II.8)}$$

where $S(q)$ is the nuclear form factor (equation (II.16)) and J_0 is the zeroth order Bessel function of the first kind.

If we assume for $f(q)$ the familiar small angle expression

$$f(q) = [p\sigma_N(i+\alpha)/4\pi]\exp(-\tfrac{1}{2}\beta q^2), \qquad \text{(II.9)}$$

where α is the ratio of the real to the imaginary part of the elastic scattering amplitude, σ_N is the hadron-nucleon total cross section, and β is the slope of the hadron-nucleon differential cross section near the forward direction, we get

$$\sigma_T = 4\pi \mathrm{Re}\int_0^\infty bdb\Big\{1-\Big[1-(1-i\alpha)(\sigma_N/4\pi)\int_0^\infty J_0(qb)S(q)$$

$$\times\exp(-\tfrac{1}{2}\beta q^2)qdq\Big]^A\Big\} \qquad \text{(II.10)}$$

We need now only set the form of the nuclear density function $\rho(\xi)$, so that the nuclear form factor can be calculated. Czyż and Lesniak[38] and Abul-Magd[39] use a Gaussian density distribution, $\rho = \rho_0\exp(-\xi^2/R^2)$, where $R^2=2R^2_{rms}/3$. Choice of this distribution allows one to perform all of the integrals in (II.10), so that (II.10) becomes upon expansion in a binomial series

$$\sigma_T = 2\pi \mathrm{Re}(R^2+2\beta)\sum_{j=1}^{A} \frac{A!}{j!(A-j)!}(-1)^{j+1}(1-i\alpha)^j(1/j)$$

$$\times[\sigma_N/2\pi(R^2+2\beta)]^j. \qquad \text{(II.11)}$$

One can see here explicitly the effect of single, double, and other orders of multiple scattering up to the Ath in terms of the powers of σ_N which appear in the summation. Note that in the Glauber theory a particle incident on a nucleus of mass number A never undergoes more than A scatters. This result follows from the fact that the theory restricts the particle to moving only in the forward direction, or at very small angles to that direction.

For heavy nuclei the Gaussian density distribution is really not a good approximation to the shape of the nucleus. A more realistic distribution is the Woods-Saxon or Fermi distribution[37]

$$\rho(\xi) = \rho_o \Big/ \Big[1 + \exp[(\xi - c)/(d/4.394)]\Big]. \qquad \text{(II.12)}$$

Unfortunately, with this distribution it is necessary to evaluate the integrals in (II.10) numerically.

In Figure 3 we show the Woods-Saxon densities for various nuclei. The parameters c, the half-density radius, and d, the skin-depth (the distance over which the density falls from 90% to 10% of its maximum value) have been taken from electron scattering experiments and are listed in Table 1. These latter experiments measure, of course, the electromagnetic radii of nuclei, which may be different from the strong interaction radii. A more recent experiment has measured these last radii from the photoproduction of neutral rho mesons on nuclei.[40] We list these results also in Table 1.

Results of calculations using the models described above will be presented in the last chapter.

C. OPTICAL MODELS

The Glauber theory is in a sense a solution to the many-body problem in nuclear scattering. Optical models on the other hand seek to replace the nucleus by a static potential which would scatter the incident particle in the same way as the actual many particle system, thereby effectively reducing the many-body problem to a single-body one. It is this approach which we consider in this section and in the next one.

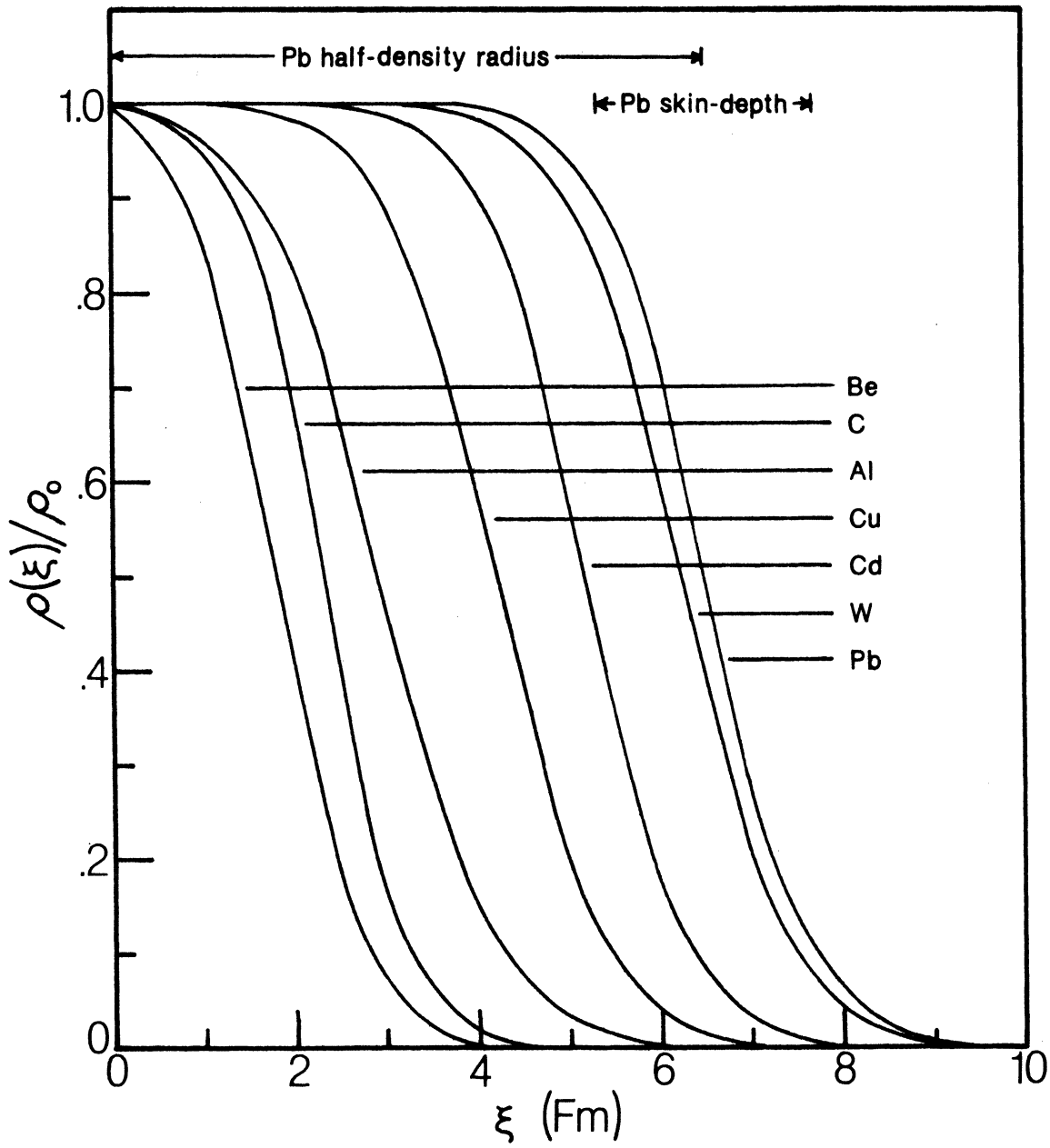

Fig. 3.--Woods-Saxon density distributions for various elements

TABLE 1

WOODS-SAXON NUCLEAR DENSITY PARAMETERS

Nucleus	Electromagnetic		Strong interaction	
	c (Fm)	d (Fm)	c (Fm)	d (Fm)†
Be	1.80 ± .08	2.0 ± .15	2.35 ± .26	2.395
C	2.30 ± .09	1.85 ± .15	2.50 ± .23	2.395
Al‡	2.95 ± .06	2.7 ± .18	3.37 ± .16	2.395
Cu‡	4.20 ± .10	2.5 ± .15	4.55 ± .11	2.395
Cd‡	5.20 ± .13	2.3 ± .15	5.40 ± .14	2.395
W‡	6.25 ± .14	2.5 ± .18	6.30 ± .12	2.395
Pb‡	6.5 ± .13	2.3 ± .13	6.82 ± .20	2.395

†The skin-depth was not a free parameter.
‡Electromagnetic parameters interpolated from the data.

The wave equation is

$$(\nabla^2 + p^2)\psi(\vec{r}) = U(\vec{r})\psi(\vec{r}), \qquad \text{(II.13)}$$

where $U(\vec{r})$ is the optical potential. In reference 35 R. J. Glauber shows that it is possible to write down a potential that will , for elastic scattering, reproduce the Glauber amplitude given in equation (II.5). This potential (on the assumption that it is spherically symmetric) is

$$U(r) = \frac{2p}{\pi r}\frac{d}{dr}\int_r^\infty \chi_{opt}(b)(b^2-r^2)^{-\frac{1}{2}}bdb, \qquad \text{(II.14)}$$

where

$$i\chi_{opt} = \ln \prod_{j=1}^{A}\left\{\int \varkappa_i(\vec{\xi}_1,\vec{\xi}_2,\ldots,\vec{\xi}_A)\left[1 - \frac{1}{2\pi ip}\int e^{-i\vec{q}\cdot(\vec{b}-\vec{s}_j)}\right.\right.$$

$$\times f_j(\vec{q})d^2q\Big]\varkappa_i(\vec{\xi}_1,\vec{\xi}_2,\ldots,\vec{\xi}_A)d\vec{\xi}_1 d\vec{\xi}_2\cdots d\vec{\xi}_A\Big\}.$$

A good approximation to (II.14) when the range of the force between the incident particle and a nucleon is small compared to the nuclear radius is

$$U(r) = \frac{-2A}{\pi}\int_0^\infty \frac{\sin(qr)}{r} f(q)S(q)qdq, \qquad \text{(II.15)}$$

where S(q) is the nuclear form factor

$$S(q) = \int e^{i\vec{q}\cdot\vec{r}}\rho(r)d\vec{r} = \frac{4\pi}{q}\int \sin(qr)\rho(r)rdr \qquad \text{(II.16)}$$

and the scattering amplitude of the incident particle on protons or neutrons is assumed, as before, to be the same and is given by f(q). If we make the further assumption that the nuclear form factor falls much more sharply with increasing momentum tranfer than does f(q)--an assumption that holds best for the heaviest nuclei--then we get

$$U(r) = -4\pi\rho(r)Af(0). \qquad \text{(II.17)}$$

It is interesting to note that one also obtains the result (II.15) when one makes the impulse approximation in the formal Watson expansion for the optical potential.[41]

We may not seem to have gained anything by what we have done in this section. All it appears that we have succeeded in doing is to write (II.3) in a different form. The value of our efforts, however, is seen when we want to introduce additional source terms on the right-hand side of (II.13). We pursue this point in the next section.

D. EFFECTS OF INTERMEDIATE INELASTIC STATES

Suppose that there exists another particle H^* whose quantum numbers are similar enough to those of the incident particle H, that the reaction

$$H + N_1 \rightarrow H^* + N_1 \qquad \text{(Reaction 1)}$$

can take place without disturbing the nucleus of which nucleon N_1 is a part. We will make clearer what we mean by "disturbing" a bit later. The reverse reaction can also occur:

$$H^* + N_2 \rightarrow H + N_2. \qquad \text{(Reaction 2)}$$

Now further suppose that the nucleons N_1 and N_2 are in the same nucleus. If the nucleus stays in the ground state, there is no way to know that the process in reactions 1 and 2 occurred "inside" the nucleus--the overall process looks to the experimenter like a simple elastic scattering. Hence, the amplitudes for the usual elastic scattering process and that for the scattering with "intermediate inelastic states" must be added to give the observed elastic scattering amplitude. From the optical theorem we see then that the total cross section will be affected.

Clearly, one requirement that must be placed on reactions 1 and 2 is that the momentum transferred to the nucleus be not so large that the nucleus leave the ground state. This momentum transfer, Δ, is

$$\Delta = p_H - p_{H^*} \approx (m_{H^*}^2 - m_H^2)/(p_H + p_{H^*}), \qquad \text{(II.18)}$$

where the approximation is for incident momenta large com-

pared to the masses m_H and m_{H^*}. The restriction--called the coherency requirement--on Δ is just the familiar indeterminacy relation

$$\Delta \cdot D \leqslant 1,$$

where D is some characteristic distance over which the process occurs; i.e., D is of the order of the nuclear diameter.

Further requirements on H^* are that it have the same charge and isospin as H. The spin of H^* does not have to be the same as that of H, but the helicity of H and H^* must be equal.[42]

In our particular case the candidates for the role of the H^* discussed above are the isospin $\frac{1}{2}$ isobars of the neutron--$N^*(1470)$, $N^*(1520)$, $N^*(1688)$, $N^*(2190)$, and presumably others of higher mass yet to be discovered. We now turn to some realizations of the ideas sketched above.

G. von Bochmann and B. Margolis[43], following the work of K. Gottfried and D. R. Yennie[44], suggest a coupled channel optical model approach. Equation (II.13) becomes the set of coupled differential equations:

$$(\nabla^2 + p^2)\psi_\alpha(\vec{r}) = \sum_\beta U_{\alpha\beta}(\vec{r})\psi_\beta(\vec{r}), \qquad \text{(II.19)}$$

where the optical potentials $U_{\alpha\beta}(\vec{r})$ are the potentials corresponding to the coherent production of particle α by particle β on the nucleus, A, under consideration; i.e., the $U_{\alpha\beta}(\vec{r})$ describe the process

$$\alpha + A \rightarrow \beta + A$$

The potentials $U_{\alpha\beta}$ may be written in direct analogy with those for elastic scattering by replacing the particle-nucleon elastic scattering amplitude by the amplitude, $f_{\alpha\beta}$, for the process

$$\alpha + \text{nucleon} \rightarrow \beta + \text{nucleon}.$$

For example (II.17) becomes

$$U_{\alpha\beta}(r) = -4\pi\rho(r)Af_{\alpha\beta}(0) \qquad \text{(II.20)}$$

Let

$$\psi_\alpha(\vec{r}) \equiv \exp(ip_\alpha z)\varphi(\vec{b},z),$$

where $\vec{b} = \vec{r}-\vec{z}$--$\vec{b}$ is therefore the impact parameter--and where p_α is the magnitude of the three momentum of particle α in the laboratory frame. Now make the eikonal approximation, i.e., the approximation that a particle traversing the nucleus is very little deflected from its initial direction and that φ_α varies but little in a wavelength. Then derivatives in x and y can be ignored compared to those in z, and, further, second derivatives in z can be ignored compared to first derivatives in z. Then equations (II.14) become

$$\frac{d}{dz}\varphi_\alpha(\vec{b},z) = \frac{1}{2ip_\alpha}\sum_\beta U_{\alpha\beta}(\vec{r})\exp[i(p_\beta-p_\alpha)z]\varphi_\beta(\vec{b},z). \qquad \text{(II.21)}$$

The differences $p_\beta - p_\alpha$ in the exponentials of equations (II.21) are given by equation (II.18).

Let us use the convention that $\alpha=1$ denotes the incident particle. The amplitude for outgoing particle β is then[45]

$$F_{\beta 1}(\vec{q}) = \sqrt{p_\beta/p_1}\; p_\beta (2\pi i)^{-1} \int e^{i\vec{q}\cdot\vec{b}} [\varphi(\vec{b},\infty) - \delta_{\beta 1}] d\vec{b}, \qquad \text{(II.22)}$$

where $\vec{q} \equiv \vec{p}_\beta - \vec{p}_1$, and $\delta_{\beta\epsilon}$ is the Kronecker delta. For elastic scattering (II.22) becomes simply

$$F_{11}(\vec{q}) = p_1 (2\pi i)^{-1} \int e^{i\vec{q}\cdot\vec{b}} [\varphi_1(\vec{b},\infty) - 1] d\vec{b}, \qquad \text{(II.23)}$$

so that the optical theorem gives

$$\sigma_T = 2\,\mathrm{Re} \int [1 - \varphi_1(\vec{b},\infty)] d\vec{b}. \qquad \text{(II.24)}$$

The set of differential equations (II.21) can be integrated numerically for the $\varphi_a(\vec{b},\infty)$ under the initial conditions $\varphi_\alpha(\vec{b},-\infty) = \delta_{\alpha 1}$.

Pumplin and Ross[46]--whose work preceded that of Bochmann and Margolis described above--have suggested that instead of letting only the discrete nucleon resonances be the intermediate inelastic states described above, one should include effects of regeneration of nucleons from the entire mass spectrum of $N\pi$ systems produced in the reaction

$$N + N \rightarrow N + N\pi,$$

regardless of the stability of the $N\pi$ system. These authors take an eikonal-optical approach to this idea. In

order to connect their work with what we have already done, we derive their results by approximate solution of equations (II.21) in Appendix G. These results are that

$$\Delta\sigma^{A}_{regn} = \int dm_{N\pi}(d^2\sigma/dtdm_{N\pi})_0 F(p,m_{N\pi}), \qquad \text{(II.25)}$$

where $\Delta\sigma^{A}_{regn}$ is the change in the total cross section due to regeneration of a nucleon from intermediate inelastic states on a nucleus of mass number A, $(d^2\sigma/dtdm_{N\pi})_0$ is the doubly differential cross section for $N + N \rightarrow N + N\pi$ at $t=0$, and

$$F(p,m_{N\pi}) \equiv 18A^2R^{-6}\Delta^{-1}\mathrm{Im}\left\{[\zeta(\lambda)-\zeta(\lambda+2i\Delta)](1-i\eta)/(1+i\eta)\right\},$$

$$\zeta(\lambda) \equiv [(1+\lambda R)e^{-\lambda R}-1+\tfrac{1}{2}\lambda^2R^2]\lambda^{-3},$$

$$\lambda \equiv 3(1-i\alpha)\sigma_N A/4\pi R^3,$$

$$\eta \equiv \mathrm{Re}[f_{NN\rightarrow NN\pi}]/\mathrm{Im}[f_{NN\rightarrow NN\pi}],$$

$$\alpha \equiv \mathrm{Re}[f_{NN\rightarrow NN}]/\mathrm{Im}[f_{NN\rightarrow NN}].$$

R is the equivalent uniform density radius of the nucleus, and σ_N is the nucleon-nucleon total cross section. Δ is given by equation (II.18).

It turns out that equation (II.25) produces decreases in the total cross section much too large to be consistent with the experimental data. We have found, however that this latter result does not necessarily follow from Pumplin and Ross's basic idea. Rather, it simply

turns out that approximations necessary to obtain equation (II.25) from equations (II.21) are apparently not very good ones. They have the effect of making--in Pumplin and Ross's language--the "weight function" $F(p,m_{N\pi})$ cut off too slowly with the mass $m_{N\pi}$. We have, therefore, solved the set of equations (II.21) numerically to calculate the predictions of their model. In Figures 4 and 5 we show plots of $(d\sigma/dtdm_{N\pi})_0$ for the reaction

$$p + p \rightarrow p + p\pi$$

at 15 GeV/c and 30 GeV/c.[46,47] These data are part of the input to Pumplin and Ross's model. To get around the problem of a continuum of masses, we have considered each bin in the histograms to represent a single $N\pi$ system with mass given by the center of the bin. $(d\sigma/dt)_{t=0}$ for this system was then taken to be $(d\sigma/dtdm_{N\pi})_0$ x(width of bin). The absolute value of the amplitude for each bin was then determined from equation (II.1). We then input these data into the set of equations (II.21). In other words we treated the problem as though we had a number of discrete resonances equal to the number of histogram bins coupled to the nucleon. (In actual fact we redivided the data in Figures 4 and 5 into 15 bins to cut down on computer time.) By this process, of course, we have added nothing new to Pumplin and Ross's ideas. All we assert we have done is to realize a better calculation of the model. Results are presented in the final chapter.

Fig. 4.--$(d\sigma/d|t|dm_{N\pi})_0$ at 15 GeV/c

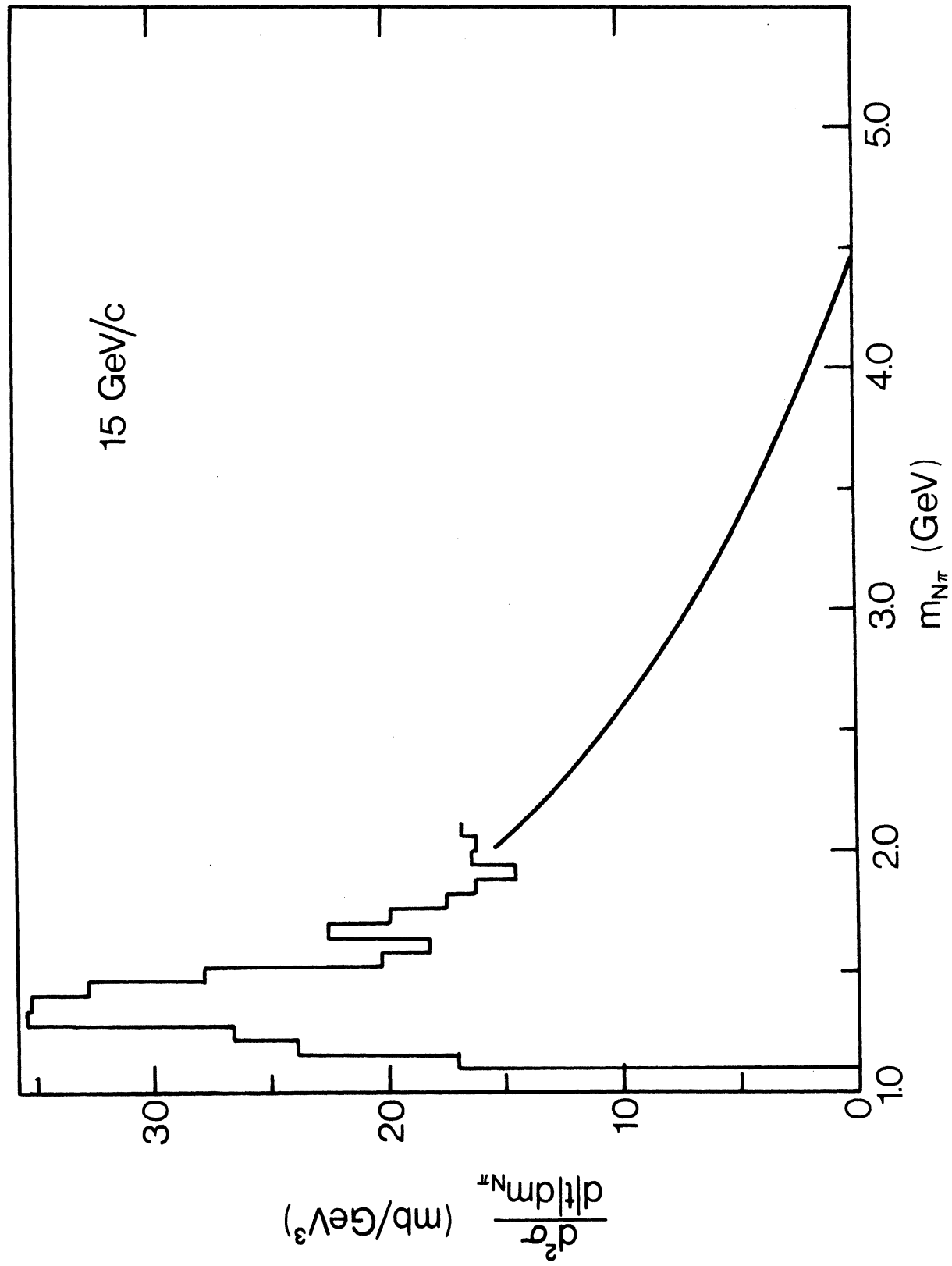

Fig. 5.--$(d\sigma/d|t|dm_{N\pi})_0$ at 30 GeV/c

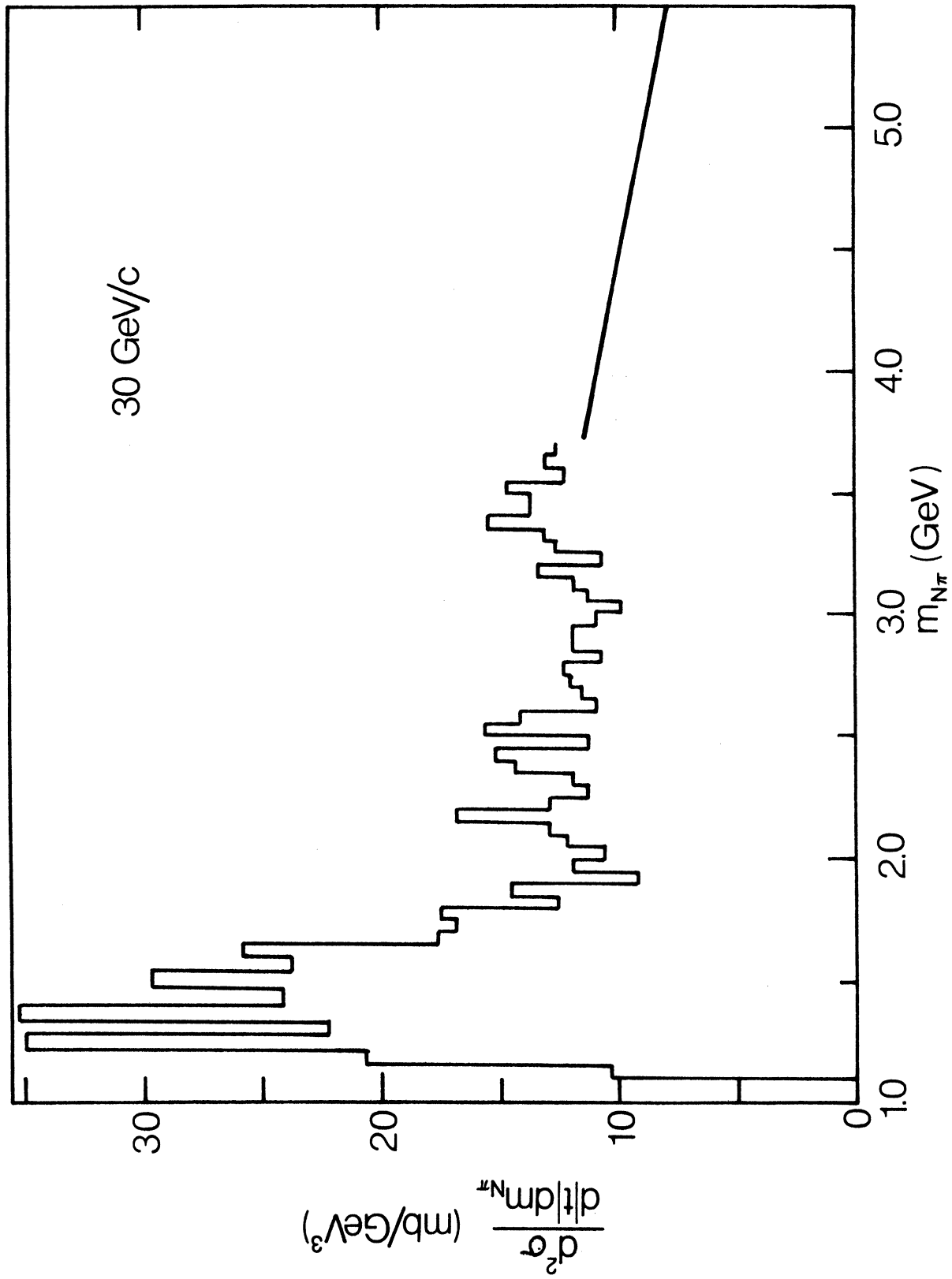

E. EFFECTS OF CORRELATIONS ON THE TOTAL CROSS SECTION

The assumption made in equation (II.7) that the positions of nucleons within the target nucleus are uncorrelated is obviously an idealization. Both the exclusion principle and the strong and Coulomb forces are at work to produce correlations in the positions of the target nucleons. (We can ignore here the fact that our projectile particle is a nucleon.[35]) We will consider only pair correlations here. Triplet and higher order correlations are expected to be small compared to these latter. The place where the effect of pair correlations is probably most easily seen is the optical potential. For example, to the same order of approximation to which equation (II.15) for the optical potential is valid, the change in the optical potential caused by pair correlations is given by[35,48]

$$(2ip)^{-1}\delta U(r) = -(2\pi Af(0)/p)^2\rho^2(r)R_c, \qquad \text{(II.26)}$$

with the "correlation length" R_c defined by

$$R_c \equiv (8\pi\beta)^{-1}\left\{\int[g(|\vec{\zeta}|)-1]\exp(-s^2/4\beta)d^3\zeta\right\}, \qquad \text{(II.27)}$$

where the pair correlation function $g(|\vec{\zeta}|)$ is given by

$$\rho(\vec{\xi}_j)\rho(\vec{\xi}_k)g(|\vec{\zeta}|) = \int|\varkappa_i(\vec{\xi}_1,\vec{\xi}_2, \ldots ,\vec{\xi}_A)|^2 d\vec{\xi}_1$$
$$\times d\vec{\xi}_2 \cdots d\vec{\xi}_{j-1}d\vec{\xi}_{j+1} \cdots d\vec{\xi}_{k-1}d\vec{\xi}_{k+1} \cdots d\vec{\xi}_A, \qquad \text{(II.28)}$$

and $\vec{\zeta}\equiv\vec{\xi}_k-\vec{\xi}_j$ and $\vec{s}\equiv\vec{\zeta}-\hat{z}(\hat{z}\cdot\vec{\zeta})$. As before, β is the slope of the forward projectile-nucleon amplitude (see equation

(II.9)). The single particle densities $\rho(\vec{\xi}_j)$ have the same meaning as previously:

$$\rho(\vec{\xi}_j) \equiv \int |\varkappa(\vec{\xi}_1,\vec{\xi}_2,\ldots,\vec{\xi}_A)|^2 d\vec{\xi}_1 d\vec{\xi}_2 \cdots d\vec{\xi}_{j-1} d\vec{\xi}_{j+1} \cdots d\vec{\xi}_A . \tag{II.29}$$

The pair correlation function is not very well known from experiment. Some theories yield predictions however. Figure 6 shows a pair correlation function from K. A. Brueckner's theory of nuclear matter.[49] This figure yields a correlation length $R_c = +0.05$ fm for $\beta = 8\ (\mathrm{GeV}/c)^{-2}$.

From (II.26) we see that for f(0) predominantly imaginary $\delta U(r)$ is almost pure imaginary and has the same sign as R_c. From (II.17), assuming f(0) has a positive imaginary part (see equation (II.9)), we note then that a positive correlation length decreases the radial extent of the optical potential, whereas a negative R_c increases it. We expect, therefore, that the total cross section will be made larger for R_c negative and smaller for R_c positive than it would be in the absence of correlation effects.

F. REMARKS ON THE NP TOTAL CROSS SECTION

In the preceding sections of this chapter we concentrated on models for the amplitudes for elastic scattering of neutrons by nuclei. We now address ourselves to a very simple discussion of nucleon-nucleon elastic scattering. Unfortunately, there exist no satisfactory theories yet

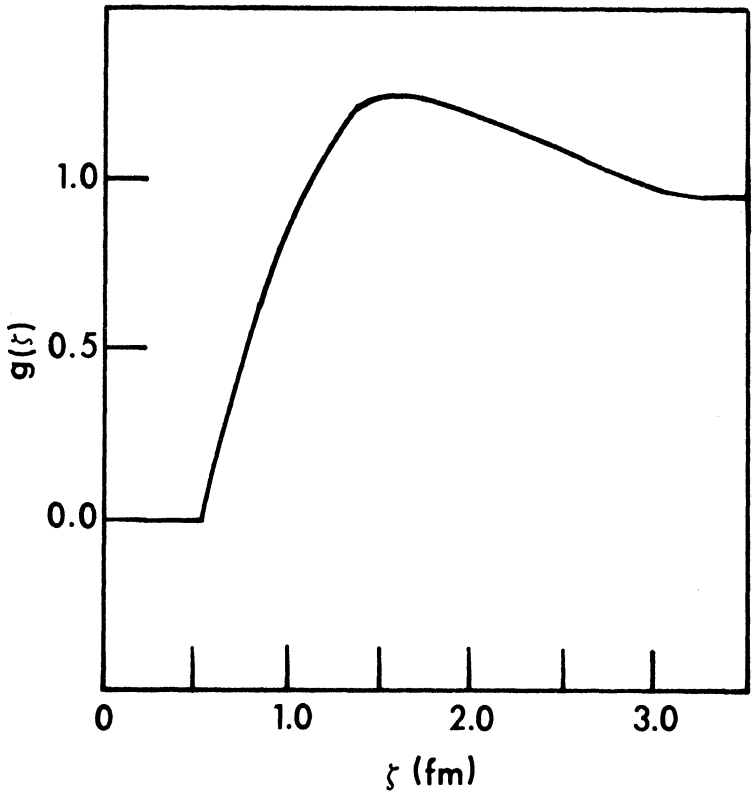

Fig. 6.--A pair correlation function from K. A. Brueckner's theory of nuclear matter.

that yield the amplitude for this process. We can, however, make some general remarks about our expectations for the relations between the np, pp and nn amplitudes from isotopic spin considerations.

The neutron and proton are respectively the $I_3 = -\frac{1}{2}$ and $I_3 = +\frac{1}{2}$ components of an isospin $I = \frac{1}{2}$ doublet called the nucleon. A two nucleon state vector can be written in the total isotopic spin basis via the usual Clebsch-Gordan series:

$$|N_a N_b\rangle \equiv |I_a, I_b; I_{a3}, I_{b3}\rangle$$

$$|N_a N_b\rangle = \sum_I |I_a, I_b; I, I_3\rangle\langle I, I_3 | I_a, I_b; I_{a3}, I_{b3}\rangle,$$

where N_a and N_b are the two nucleons and $\vec{I} = \vec{I}_a + \vec{I}_b$. Thus,

$$|pp\rangle = |\tfrac{1}{2}, \tfrac{1}{2}; 1, +1\rangle \equiv |1, +1\rangle,$$

$$|nn\rangle = |\tfrac{1}{2}, \tfrac{1}{2}; 1, -1\rangle \equiv |1, -1\rangle,$$

$$|np\rangle = \sqrt{\tfrac{1}{2}}\left\{|\tfrac{1}{2}, \tfrac{1}{2}; 1, 0\rangle + |\tfrac{1}{2}, \tfrac{1}{2}; 0, 0\rangle\right\} \equiv \sqrt{\tfrac{1}{2}}\left\{|1, 0\rangle + |0, 0\rangle\right\}.$$

Let us now make the postulate of charge independence; i.e., that if electromagnetic effects are ignored the interaction between two nucleons depends only on their total isospin but not on their individual charges. The operator, G, describing nucleon-nucleon scattering then commutes with all three components of the total isospin I:

$$\left[G, \vec{I}\right] = 0.$$

This last fact implies that G is an isoscalar operator, or

that total isospin is conserved as well as its third component. G will have two matrix elements corresponding to scattering in the triplet (symmetric) isospin state and to scattering in the singlet (antisymmetric) state. Let us designate these two parts of G as G_S and G_A respectively.

Then the amplitudes for pp, nn and np elastic scattering are respectively

$$f_{pp} = \langle 1,+1|G_S|1,+1\rangle$$

$$f_{nn} = \langle 1,-1|G_S|1,-1\rangle$$

$$f_{np} = \tfrac{1}{2}[\langle 1,0|G_S|1,0\rangle + \langle 0,0|G_A|0,0\rangle].$$

From our discussion above we have $\langle 1,+1|G_S|1,+1\rangle = \langle 1,0|G_S|1,0\rangle = \langle 1,-1|G_S|1,-1\rangle \equiv M_S$ if charge independence holds. Let us also define $M_A \equiv \langle 0,0|G_A|0,0\rangle$. We see that $f_{pp} = f_{nn}$, so that from the optical theorem $\sigma_T(pp) = \sigma_T(nn)$. Note that charge independence does not imply $\sigma_T(pp) = \sigma_T(np)$ or $\sigma_T(nn) = \sigma_T(np)$. If we should find from experiment that these last relations do hold true, then we can say that $\mathrm{Im}[M_S(t=0)] = \mathrm{Im}[M_A(t=0)]$, where t is the square of the four momentum transfer.

A final point is that by implying that the pp and nn scattering amplitudes are equal, isospin conservation implies that for deuterium the elastic scattering amplitudes for protons and neutrons should be equal. Therefore, we expect our neutron-deuteron total cross sections to equal the proton-deuteron total cross sections at the same ener-

gies in the center of mass system. (Since the masses of the neutron and proton are practically equal, we can also the make the comparison at the same energies in the laboratory system.) It is not necessary to invoke charge independence, however, to show that the pd and nd total cross sections should be equal. The much weaker principle of charge symmetry, i.e. that the force between two neutrons is the same as the force between to protons when electromagnetic effects are ignored, also implies this result.

CHAPTER III

EXPERIMENTAL APPARATUS AND TECHNIQUE

A. GENERAL DESCRIPTION OF THE EXPERIMENTAL LAYOUT

Figure 7 shows a schematic plan view of the experimental layout. Starting at the left, we have the production target - an 18 cm x .25 cm x .50 cm piece of beryllium mounted in the slow extracted proton beam of the AGS. About 15 meters downstream of this target are several magnets and a collimator which were used respectively to extract and to define charged beams for other experiments on the AGS floor. The magnets also acted as our sweeping magnets and removed charged particles from the beam. This process left a neutral beam which consisted primarily of neutrons and gamma rays. A lead filter then removed part of the photon component of the beam. The beam was collimated to 1.25 cm in diameter by a 150 cm long brass and lead collimator. The beam then passed through a channel in a concrete shielding wall , and charged particles produced in the last collimation were removed by another sweeping magnet. The first of the beam intensity monitors then followed. Between this beam monitor and the next one--about 25 meters downstream--was initially an experiment to measure the differential cross section for neutron-proton charge exchange and later an experiment to investigate the production of nucleon isobars on heavy nuclei. These experiments placed very little material in the beam, so that it was possible to run simultaneously with them. A final lead filter in the beam re-

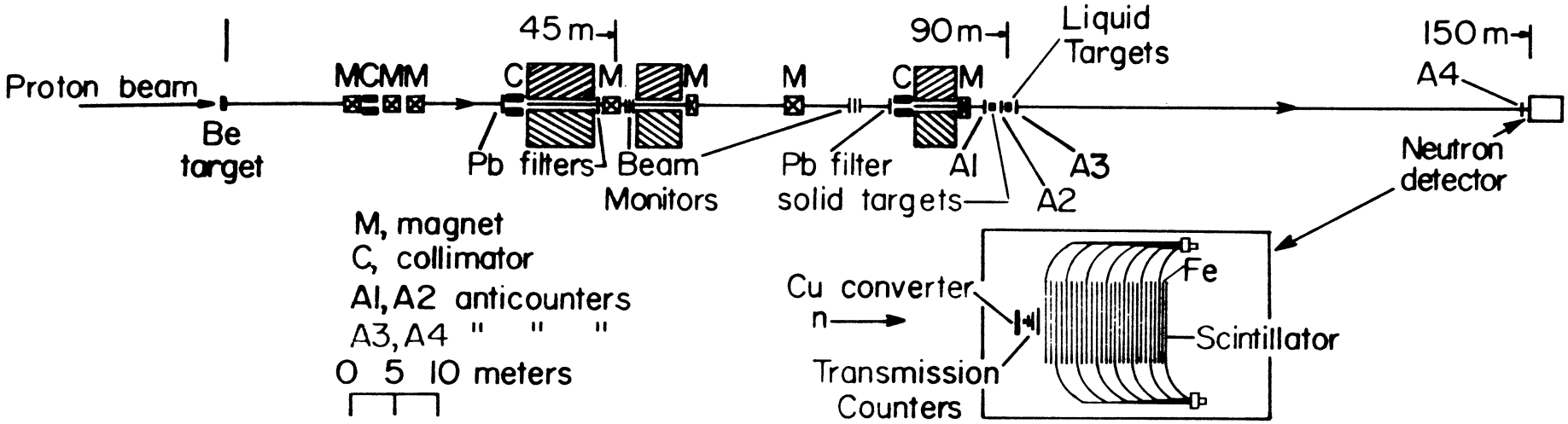

Fig. 7.--Plan view of experimental layout

duced gamma contamination to a negligible level. A 125 cm brass and lead collimator, adjustable in diameter, gave final definition to the beam. A C-type magnet of 125 cm pole length--run typically at a field strength of 7 kilogauss--removed the last of the charged particles. This magnet was also filled with lead except for a 5 cm x 5 cm channel centered on the beam line to reduce any halo of uncharged particles around the collimated beam.

The beam then passed through an area where the targets to be studied could be placed. The solid targets were mounted on a transport that moved them laterally into or out of the beam. This transport was contolled remotely from the experimental trailer. The liquid target assembly was fixed permanently immediately behind this transport. Anticoincidence counters were placed before and after the targets to veto charged particles that might enter or be created in the target and continue downstream. The last anticounter was preceded by 1.25 cm of lead to remove most of the gammas formed in inelastic events in which neutral pions were produced. The neutron detector was located about 60 meters downstream from this anticounter.

(During part of the experiment a 30 cm diameter vacuum pipe was mounted along this 60 meter line. It was removed near the end of our running to see whether rescattering from it of particles scattered by the targets had any effect on our results. Anti-counter A4 was then used to veto charged particles formed in the air between the target and

the neutron detector. See Appendix E.)

B. THE PRODUCTION TARGET AND THE BEAM

Ideally, since the cross sections to be measured in this experiment can be expected to have an energy dependence, one should like to have a beam of monoenergetic neutrons for this experiment. Such a beam, however, is not currently (or foreseeably) available. As a compromise, one seeks to produce a neutron beam whose spectrum is peaked at its high energy end. One normally chooses a light element on which to produce such a neutron beam from a proton beam rather than a heavy one. This choice follows from considerations of the likelihood of further interactions of the neutron secondary in the same target nucleus. One would prefer the neutron not to interact again with that nucleus, since in doing so it is likely to lose energy and to produce an unwanted background of lower energy neutrons. In a simple optical model, the probability that the secondary does not undergo an interaction in the same nucleus is proportional to the transparency of the nucleus, i.e., to $1 - \sigma_{abs}/(\pi R^2)$, where σ_{abs} is the absorption cross section, and R is the equivalent uniform density radius of the nucleus. Experimentally the transparency is found to be proportional to $A^{-2/3}$, where A is the atomic mass number.[34] Thus, beryllium is about 8 times "better" than lead as a production target. From energy and momentum conservation considerations one expects the best takeoff angle from the

production target for a strongly peaked secondary beam to be zero degrees, and this is indeed the case.

One also requires that the beam profile be as sharp as possible--that it have steep tails and negligible halo--and that in order to facilitate geometrical efficiency calculations for counters in the neutron detector, it be circular. To accomplish this send we excercised great care in aligning the defining collimator so that it was parallel to the beam. Small deviations of the collimator from true parallel to the beam line produced a noticeably elliptical beam spot at the detector, and also introduced halo from small angle scattering from the collimator wall. After a survey alignment, final positioning was accomplished by taking Polaroid exposures of the beam at the detector assembly and adjusting the collimator's position until the pictures showed a round spot. During most of the experiment either a 0.32 cm or 0.48 cm diameter defining collimator was used. We did, however, use both larger and smaller diameter collimators than these at times to increase or to reduce the beam intensity.

C. BEAM MONITORS

Two telescopes, each consisting of three counters, monitored beam intensity. The first counter in a monitor was used to veto any charged particles in the neutral beam. The second counter was preceded by a block of lucite to produce charged particles which the second and third counters

were required to detect in coincidence. The counting rate from a monitor was therefore proportional to beam intensity. (We can safely ignore questions of dead time loss and accidental coincidences in the monitors, since, in the calculations we make, only the ratio of monitor counts during target-out data collection periods to the counts during target-in data collection periods is necessary. We are assuming, of course, that the beam intensity and the duty cycle were the same during target-out and target-in counting periods.) Two monitors were used to provide a check on one another. They tracked quite well. (The error introduced into our cross sections by disagreement between the two monitor normalizations was $\lesssim 0.15\%$ on the average.)

D. TARGETS

The solid targets were selected so that impurities in them introduced no more than two tenths of a percent uncertainty into the measured cross sections. The lead and copper targets were obtained from the metals stores at Brookhaven and were known to be at least 99.5% pure by weight, with contaminants that were close in atomic number to them. The other targets, excluding aluminum, had been used before in a similar experiment at lower energies and were known to contain impurities that would introduce less than a 0.2% uncertainty into the cross sections.[50] The aluminum target was composed of type 6061 aluminum.

The liquid targets, hydrogen and deuterium, were contained in a mylar flask which was 121.9 ± 0.16 cm long at 20°C with equal pressures outside and inside it. This flask had an inside diameter of 7.6 cm. The flask was enclosed in an aluminum vacuum jacket with 0.027 cm thick mylar end windows. A schematic drawing of the liquid target assembly is shown in Figure 8.

It would have been desirable to have two identical flasks - one of which would have contained the target liquid and the other of which would have been evacuated - and mechanically put one or the other into the beam for "target-in" and "target-out" data collection. We were, however, unable to obtain such an arrangement from the target group at Brookhaven. As a result we settled for a single flask target which was filled or emptied for in or out runs respectively. Such an arrangement had several disadvantages. First, since it was desirable to keep target-in and target-out runs short and to cycle between them quickly, the target required continual supervision by an operator. Second, because of the fast cycling requirement, one could not wait for the target to become quiescent after a change in its state. The pressure in the flask was still changing during the data collection periods, thereby introducing uncertainties into the density of the liquid inside. Finally, one had to make corrections to the data for the residual gas left in the target, these corrections bringing additional uncertainties into the measured attenuations. All of the

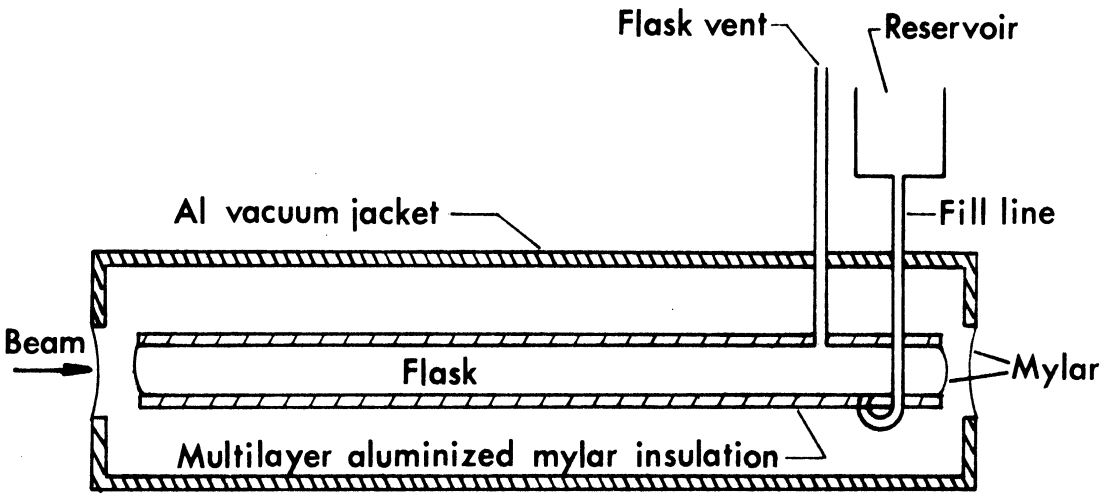

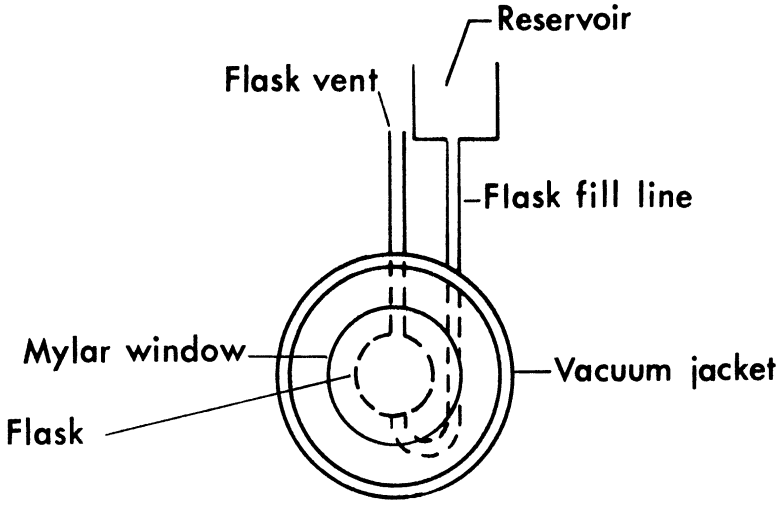

Fig. 8.--Liquid target assembly

aforementioned corrections are discussed in Chapter IV.

E. THE NEUTRON DETECTOR

Figure 9 is a schematic representation of the neutron detector. It had two principal parts: the converter plate – transmission counter assembly and the ionization calorimeter or total absorption spectrometer (TAS). The former was used to determine the attenuations of the neutron beam by the experimental targets, and the angular distributions of neutrons scattered from those targets. The latter was used to determine the neutron energy. For a discussion of transmission techniques in total cross section measurements, see reference 56. References 10 and 51 give more detailed discussions of the properties of ionization calorimeters.

The four transmission counters were disks of 0.64 cm thick plastic scintillator. Their radii and the solid angles subtended by them at the targets are given in Table 2. These counters were mounted in order of increasing diameter, with the largest counter farthest downstream. Immediately preceding the counters was a 1.6 cm thick sheet of copper which was used to convert a fraction of the incident neutrons to charged particles for detection by the transmission counters. At the high energies at which this experiment was performed, the shower of particles created by a conversion usually goes along the direction of the incident neutron with a very small opening angle. Thus the

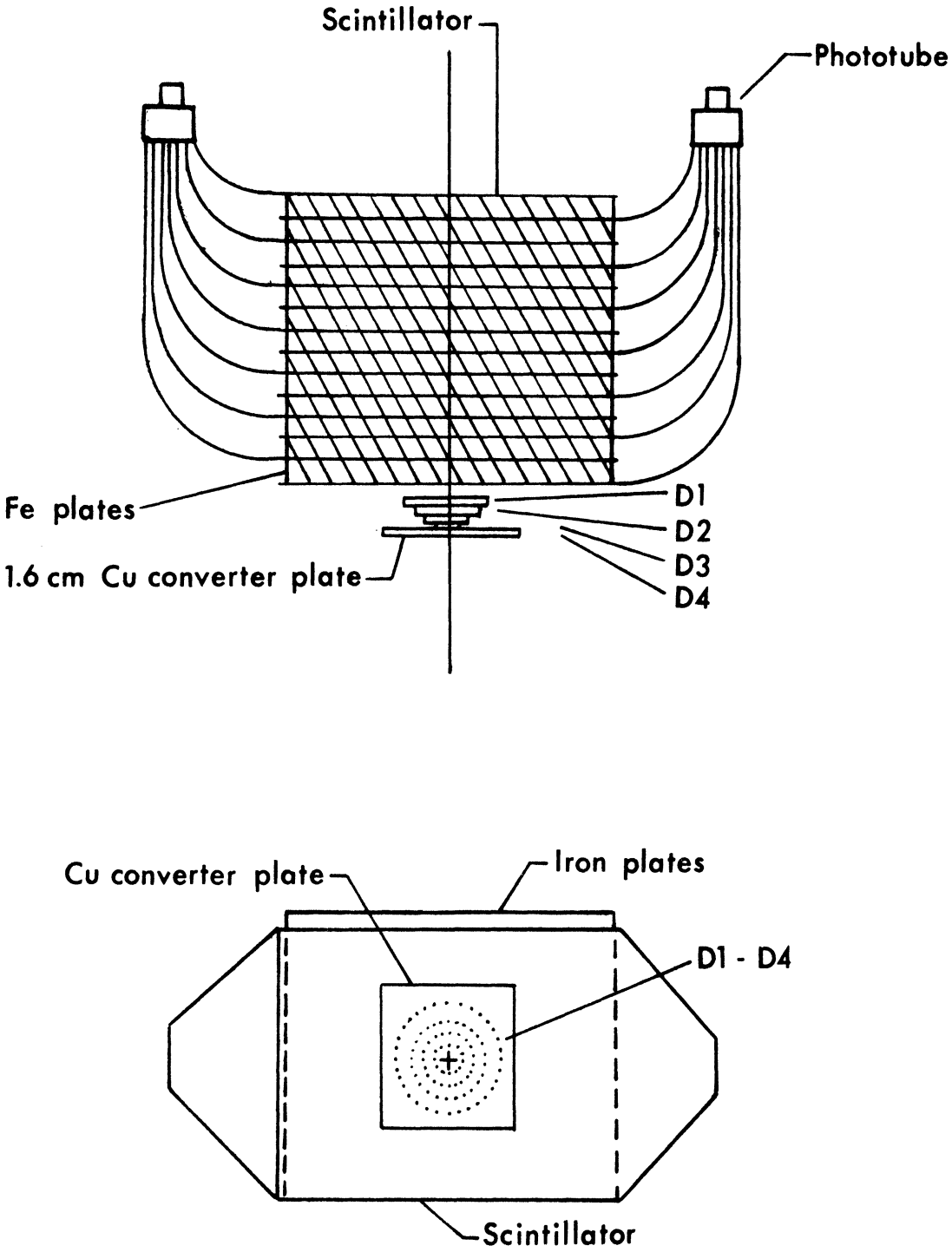

Fig. 9.--Neutron detector

transmission counters gave a fairly good determination of the neutron's scattering angle. In order that each point on a counter saw the same amount of conversion material before it as every other point, we fitted each of the three upstream counters into lucite sheets which entirely covered the last counter. Each of the four counters was viewed by its own RCA 6810 photomultiplier tube. Alignment of the axis of the counter centers with the center of the incident beam was done by exposing beam Polaroids.

TABLE 2

TRANSMISSION COUNTER SIZES
AND SOLID ANGLES

Counter	Radius (cm)	Solid Angle (μsr)	
		Liquid targets	Solid Targets
D4	9.84	0.32	0.30
D3	5.72	0.88	0.83
D2	3.18	2.8	2.7
D1	1.91	8.4	8.0

The TAS was the energy selecting part of the detector. It consisted of 14 scintillator plates, 56 cm x 82 cm x 0.64 cm, interleaved with 13 iron plates 3.8 cm thick. The light from the first, third, fifth, seventh, ninth, eleventh and thirteenth scintillators was summed optically and viewed by a 56AVP photomultiplier tube. The light from the other seven scintillators was similarly summed and

viewed by a second 56AVP phototube. The ouput of the two tubes was then passively added to give a pulse roughly proportional to the energy of the incident neutron. We discuss the response characteristics of the TAS in Appendix A.

F. ELECTRONICS AND LOGIC

In Figure 10 we show a schematic of the neutron detector electronics and logic. All the discriminators, coincidence circuits and fanouts used were of the Chronetics 150 series, except for the secondary TAS 20% discriminator (the one indicated in the diagram as having only one output used). This discriminator was of the Chronetics 100 series and served, therefore, as a check against any idiosyncrasies peculiar to the primary TAS 20% discriminator. A pulse from any of the anticounters A1, A2, A3 or A4 vetoed charged particles. (The effect of backscatter from the TAS or the converter plate into A4 is discussed in Appendix E.) The output from each transmission counter phototube was fed to a discriminator which generated a 15 nanosecond logic pulse when triggered. The output from the TAS was split and fed to amplifiers as shown in the figure to give seven different channels, each of which was fed to a discriminator. The triggering levels on the discriminators were set so that only a certain fraction of the larger TAS pulses would fire them. For example, the discriminators marked "TAS 20%" counted only 1/5 of the total number of pulses from the calorimeter. Clearly,

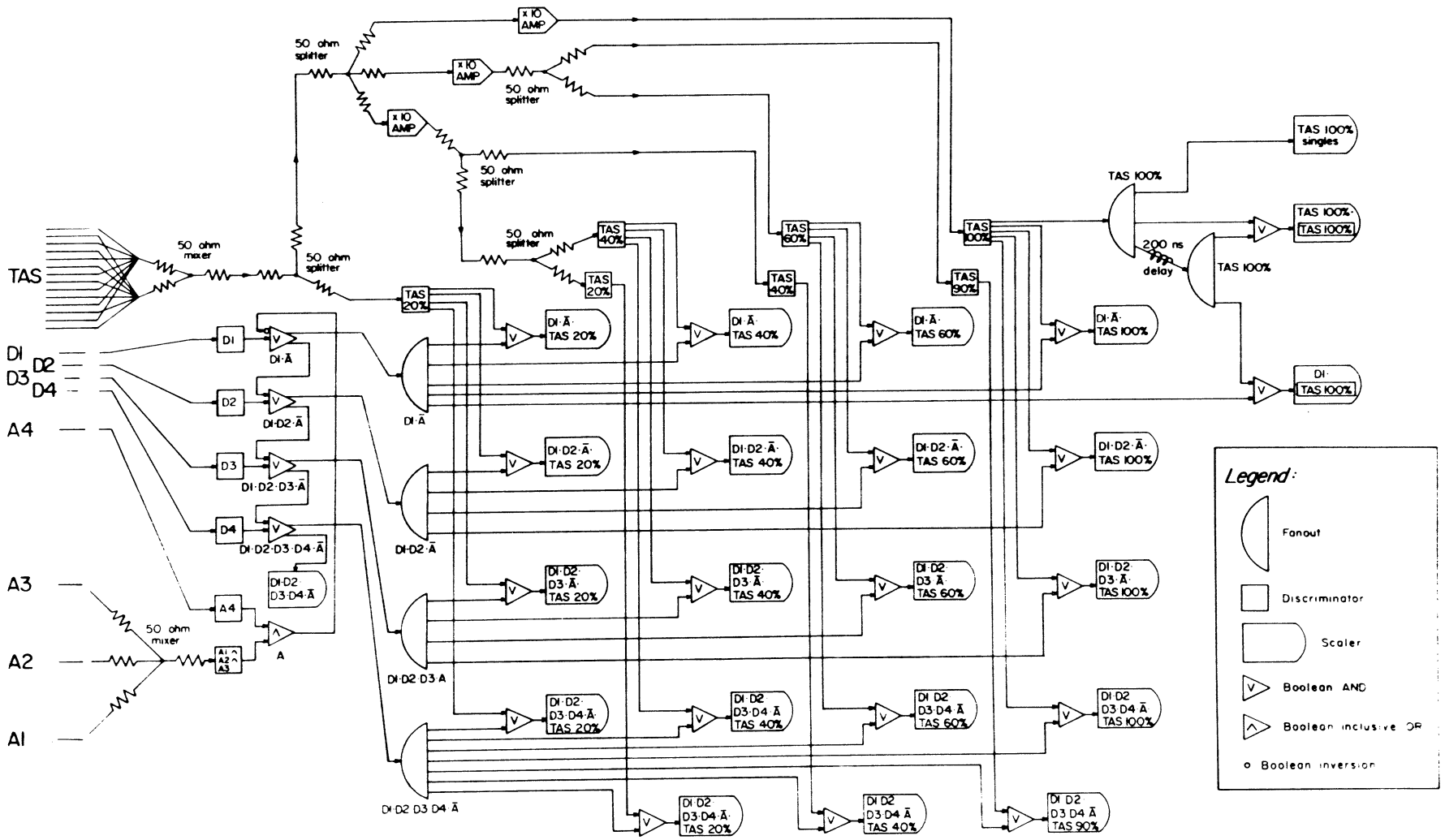

Fig. 10.--Electronics and logic for the experiment

since a discriminator is a minimum threshold device, these were the 20% largest pulses from the TAS. The other discriminators were set to trigger on the upper 20%, 40%, 40%, 60%, 90% and 100% of the TAS output pulses. The duplicated channels were used as checks on one another and on the effects of the amplifiers on the data. (The "90%" TAS channel was set to 90% only during part of the experiment. We actually varied it from 65% to 90% during the experiment. We call it "90%" only to give it a label.) The largest pulses from the TAS generally corresponded to the most energetic neutrons (see Appendix A).

The coincidences $D1 \cdot \overline{A} \cdot TAS$, $D1 \cdot D2 \cdot \overline{A} \cdot TAS$, $D1 \cdot D2 \cdot D3 \cdot \overline{A} \cdot TAS$, and $D1 \cdot D2 \cdot D3 \cdot D4 \cdot \overline{A} \cdot TAS$ were formed in the logic and scaled for the 100%, 60%, and one each of the 20% and 40% channels or "cuts". For the remaining three (secondary) channels only the $D1 \cdot D2 \cdot D3 \cdot D4 \cdot \overline{A} \cdot TAS$ coincidence was formed and scaled.

In addition the quantities $D1 \cdot D2 \cdot D3 \cdot D4 \cdot \overline{A}$, TAS 100% singles, $D1 \cdot TAS\ 100\%_{delayed}$, and $TAS\ 100\% \cdot TAS\ 100\%_{delayed}$ were scaled. The first of these provided a convenient running check on the stability of the transmission counters, and the last three provided information on the beam structure and the accidentals rate (see Appendix D).

G. DATA COLLECTION

The target-in and target-out data collection periods were cycled rather quickly to minimize any possible biases

in the data caused by drifts in the electronics. For the solid targets the cycles were kept to about three minutes target-in and three minutes target-out with approximately thirty seconds needed after each change of target condition to type out the scaler data and to punch it on paper tape. For the liquid targets the target-in and target-out periods were lengthened to twelve to fifteen minutes each for two reasons. First, it took longer to change the state of the target--about two minutes on the average to fill it. And second, it was desirable to take target-full data after the pressure in the flask had settled down. In each of the target-out or target-in periods for a liquid target, we recorded the scaler data four times at equally spaced intervals to see whether we could find evidence of any time dependence in the data.

CHAPTER IV

DATA ANALYSIS

A. INTRODUCTION

Each of the four transmission counters measured a slightly different value for the ratio of target-out counts to target-in counts, with the smallest counter yielding the largest such value. As discussed in Chapter I, this effect is due to small angle scattering from the target. Since each counter subtended a nonzero solid angle at the target, each counted, in addition to unscattered neutrons, scattered neutrons which left the target at sufficiently small angles. The larger the counter, the more scattered neutrons it counts. The attenuation, or partial, cross section for the ith counter is defined as

$$\sigma(\Omega_i) \equiv \frac{-1}{nx} \ln\left[(I^i_{in}/M_{in})/(I^i_{out}/M_{out}) \right], \qquad \text{(IV.1)}$$

where Ω_i is the solid angle subtended at the target by the counter, n is the density of the scatterers (nuclei) in the target, x is the target thickness, I^i_{in} and I^i_{out} are the numbers of target-in and target-out counts respectively, and M_{in} and M_{out} are the number of beam monitor counts during the target-in and target-out periods respectively. $\sigma(\Omega_i)$ will then decrease with increasing Ω_i. At $\Omega_i=0$ equation (IV.1) gives the usual expression for the total cross section, σ_T. Therefore, using a suitable parametrization, one extrapolates the several measured partial cross sections to zero solid angle to obtain the total cross section.

B. CORRECTIONS TO THE CROSS SECTIONS

The partial cross sections as measured required a small correction before they could be used in the extrapolation procedure, since they were somewhat dependent on the instantaneous beam flux or rate. This statement may sound puzzling, since it appears in equation (IV.1) that, by normalizing to the beam monitor counts, we should have removed this dependence. Actually, equation (IV.1) is good only as long as the counting rate is low. Second-order effects are important when the counting rate becomes large. While the time-averaged counting rate in this experiment was low, the instantaneous rate was often large because of "spikes" in the beam spill associated with the RF frequency of the AGS. There were three such possible effects in this experiment. The first was that it was possible for two neutrons to pass through the transmission counters closely enough in time (about 15 nanoseconds), so that they could be counted as only one neutron. The second was that the two low energy neutrons could pass into the TAS sufficiently close in time (about 30 nanoseconds) to be counted as only one higher energy neutron. Finally, the third effect was that the pulse height from the TAS phototubes varied as the rate went up, so that--aside from questions of TAS energy resolution--the pulse height from the TAS phototubes was a function of the instantaneous intensity. The first and third effects usually make a partial cross section calculated from equation (IV.1)smaller than its actual value, while the second

will make it larger. As we show in Appendix D, all of these effects, if they are small, can be accounted for by the simple procedure of measuring the partial cross sections at different rates and fitting the result to

$$\sigma_m(\Omega_i) = \sigma_r(\Omega_i)(1 + \alpha R), \qquad \text{(IV.2)}$$

where $\sigma_r(\Omega_i)$ is the true partial cross section, $\sigma_m(\Omega_i)$ is the measured partial cross section at rate R, and the parameter α is to be determined from the fit. The rate R was taken to be equal to TAS 100%·TAS $100\%_{\text{delayed}}$/(TAS 100% singles) (see Appendix D). α will be positive if the second effect is dominant, or negative if the first and third effects are. In Table 3 we list the values of α we found for counter D4 for the TAS cuts for which we will report results. The values of α for the other counters were the same as those for D4 to within 15%. Since the rate data were taken simultaneously for all four transmission counters, such a difference indicates that not all of the rate dependence could be attributed to the TAS. There had to be some rate dependence in the transmission counters also.

TABLE 3

VALUES OF THE RATE CORRECTION PARAMETER

AGS Energy (GeV)	TAS Cut (%)	α	Typical Value of αR
14.5	70	-3.9 ± 1.5	-0.005
21.3	90	-2.2 ± 0.4	-0.004
28.1	20	-3.5 ± 4.1	-0.009

In the case of the liquid targets it was also necessary, as noted in Chapter III, to take into account variations in the liquid density during target-full periods and correct for gas left in the target during the empty periods. We were able to monitor the pressure in the target, and data are available[52,53,54,55] which accurately relate the specific volumes of liquid hydrogen and liquid deuterium to pressure for the liquids in equilibrium with their respective gaseous states (as they were in the target), so that the first correction could be made with confidence.

In Figures 10 and 11 we show typical plots of the pressure inside the target as a function of the time after the flask was filled. We took such data several times during the course of the experiment and found that the plots were reasonably reproducible. The average value of the pressure in the flask during a target-full run from all these data was 18 ± 1 psi for hydrogen and 6.8 ± 0.5 psi for deuterium. These pressures correspond to densities of 0.07013 ± 0.00024 gm/cm^3 for hydrogen[52,54,55] and 0.1709 ± 0.0004 gm/cm^3 for deuterium[53], or a systematic error in the measured cross sections of 0.4% and 0.25% respectively. To be certain that we were not underestimating this source of errors, took double the latter values as the systematic uncertainties.

To make the corrections for residual gas in the target during target-empty data periods, it was necessary to know the pressure and the temperature of the gas. We had,

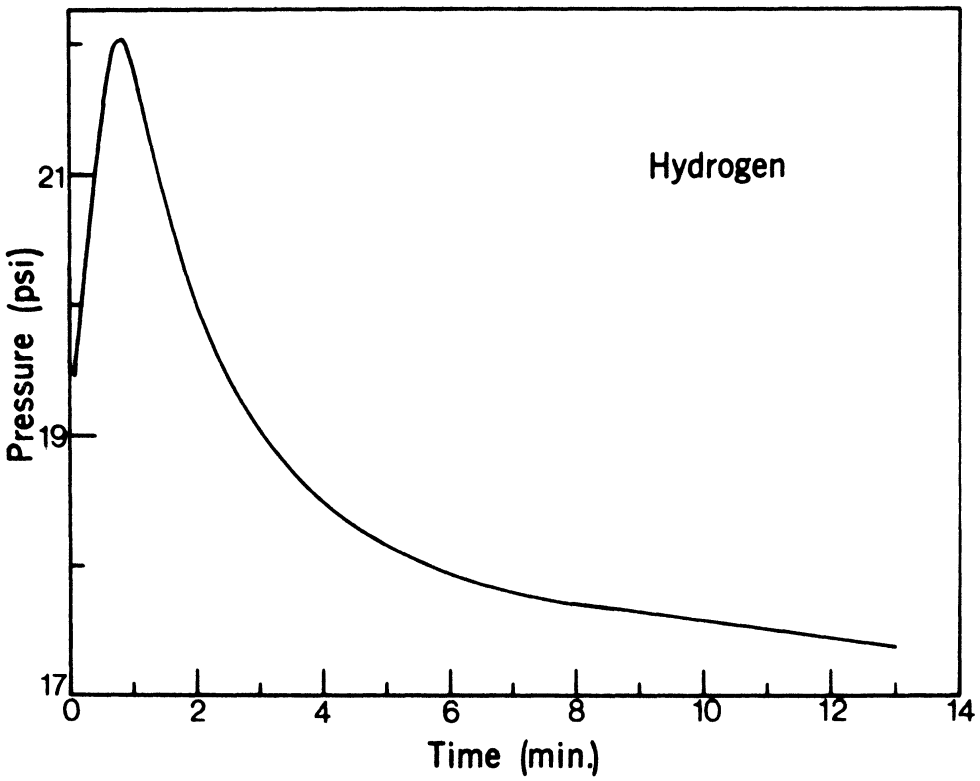

Fig. 11.--Pressure in the full hydrogen target as a function of time

Fig. 12.--Pressure in the full deuterium target as a function of time

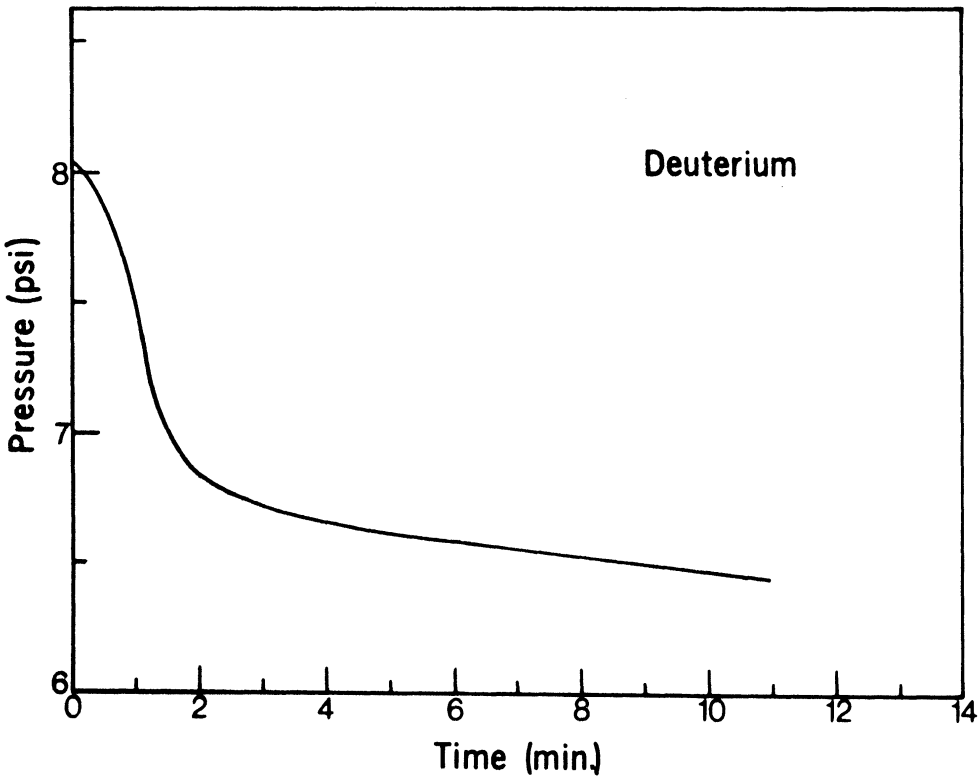

however, no way of measuring the temperature, and therefore had to make an estimate. This procedure was further complicated by the fact that, to empty the target quickly, room temperature hydrogen (or deuterium) gas was pumped in to force the liquid hydrogen (or deuterium) from the flask, so that the gas left in the flask could not be assumed to be at the liquid temperature (~20° K). Following Parker[50], who had a similar target, we assumed that the gas temperature was initially 50° K and took its pressure at that time as the average of the initial pressures recorded during several runs. This latter pressure was 19 ± 2 psi for hydrogen and 6.5 ± 0.5 psi for deuterium. We allowed the generous errors of $^{+250^\circ K}_{-\ 25^\circ K}$ on the estimated temperature. From National Bureau of Standards tables[55], one then finds a residual thickness of hydrogen of $0.078\ ^{+0.078}_{-0.063}$ gm/cm^2 and of deuterium of $0.052\ ^{+0.052}_{-0.039}$ gm/cm^2. From Table 4, which gives the thicknesses of the targets used in the experiment, we see that the corrections amount to $+0.9\ ^{+0.9}_{-0.7}\%$ for hydrogen and $+0.25\ ^{+0.25}_{-0.2}\%$ for deuterium.

Finally, a small correction for Coulomb scattering of the neutrons via their magnetic moment by the targets was made. This effect is discussed in Appendix C. In Table 5 we list examples of the corrections to be subtracted from the partial cross sections for various elements at several different mean neutron momenta. This effect has been overlooked in earlier experiments, although it would have necessitated corrections of the same size as ours in one case.[14]

TABLE 4

TARGET DENSITIES AND THICKNESSES

Element	Density (gm/cm^3)	Thickness (cm)	Thickness (nuclei/barn)
H_2	0.07013 ± 0.00024	122.61† ± 0.16	5.137 ± 0.038
D_2	0.1709 ± 0.0004	121.94† ± 0.16	6.221 ± 0.033
Be	1.848	9.373	1.158
C	1.751	10.16	0.8922
Al	2.699	7.493	0.4514
Cu	8.97	3.170	0.2692
Cd	8.65	3.749	0.1737
W	19.3	2.088	0.134
Pb	11.35	3.810	0.1257

†The liquid target flask contracted 0.39 cm in cooling from 293° K to 20° K. It also had a coefficient of pressure expansion of 0.89 cm/atmosphere.

C. ANALYSIS OF THE PARTIAL CROSS SECTION DATA

When one measures a set of partial cross sections by the technique which we have described, the values obtained for those cross sections are not statistically independent. One can easily see why: a particle passing through one of the transmission counters will (in most cases) also pass through the next largest counter. The measured partial cross sections will therefore exhibit a high degree of correlation.

TABLE 5

EXAMPLES OF COULOMB CORRECTIONS TO THE PARTIAL CROSS SECTIONS

Element	Mean Momentum (GeV/c)	Correction (mb)	
		Counter D4	Counter D1
C	11.8	0.07	0.03
	16.9	0.06	0.03
	25.4	0.05	0.02
Cu	11.8	1.52	0.56
	16.9	1.15	0.40
	25.4	0.97	0.21
Pb	11.8	9.41	3.31
	16.9	8.07	1.99
	25.4	6.53	0.50

The only independent information obtained from each of the successively larger counters comes from the annular region of the counter lying between its perimeter and that of the preceding counter. This fact implies that the differences between the partial counters measured by successive transmission counters are (roughly) statistically independent quantities.[56] Thus a measurement of n partial cross sections produces a set of n statistically independ-

ent quantities which consists of one partial cross section and n-1 differences between partial cross sections: $[\delta\sigma]_1$, $[\delta\sigma]_2$, . . . , $[\delta\sigma]_{n-1}$.

The total cross section is related to a partial cross section through

$$\sigma_i = \sigma_T - \int_{\Omega_i} \frac{d\sigma}{d\Omega} E_i(\theta,R)d\Omega \ , \qquad \text{(IV.3)}$$

where σ_i is the partial cross section measured by the ith transmission counter, σ_T is the total cross section, Ω_i is the solid angle subtended at the target by the ith counter, and $(d\sigma/d\Omega)$ is the differential cross section describing nuclear scattering--both elastic and inelastic--of neutrons by the target. $E_i(\theta,R)$ is the geometrical efficiency for detection by the ith counter of a neutron scattered at an angle θ out of a beam whose radius is R at the transmission counter (see Appendix B). We assume that at fixed momentum $(d\sigma/d\Omega)$ is a function of θ only. The set of differences between the partial cross sections gives us a set of points on the differential cross section: $[\delta\sigma(\langle\theta_1^2\rangle)]_1/[\delta\Omega]_1$, $[\delta\sigma(\langle\theta_2^2\rangle)]_2/[\delta\Omega]_2$, . . . , $[\delta\sigma(\langle\theta_{n-1}^2\rangle)]_{n-1}/[\delta\Omega]_{n-1}$, where the $[\delta\Omega]_j$ are the solid angles subtended at the target by the annular regions between the perimeters of successive transmission counters, and $\langle\theta_j^2\rangle$ is the average squared scattering angle for a neutron striking the jth such annulus. $\langle\theta_j^2\rangle$ is itself related to the differential cross section by

$$\langle\theta_j^2(R)\rangle = \left[\int\theta^2 F_j(\theta,R)\frac{d\sigma}{d\Omega}d\Omega\right]\Big/\left[\int F_j(\theta,R)\frac{d\sigma}{d\Omega}d\Omega\right] \qquad \text{(IV.4)}$$

where $F_j(\theta,R)$ is the geometrical efficiency for detection by the jth annular region of scintillator of a neutron scattered at an angle θ (see Appendix B). The other symbols are as before.

The procedure we followed was to propose a parametrization for $(d\sigma/d\Omega)$, assign a set of reasonable starting values to the $\langle\theta_j^2\rangle$, make a fit to the set of measurements $[\delta\sigma(\langle\theta_j^2\rangle)]_j/[d\Omega]_j$ to obtain the parameters of $(d\sigma/d\Omega)$, and then calculate σ_T from (IV.3) using the partial cross section measured by the smallest transmission counter. A next approximation to the set of $\langle\theta_j^2\rangle$ was calculated from (IV.4) with these last parameters, another fit was then performed to obtain a new set of parameters, and σ_T was again calculated. This procedure was iterated until σ_T changed by less than 0.01% from its value on the previous iteration. None of the $\langle\theta_j^2\rangle$ ever differed by more than two percent from the zeroth order estimates one could calculate from (IV.4) by using $(d\sigma/d\Omega) = 1$.

Other experimenters[14,50] have reported that they found that their extrapolations were consistent with considering the nucleus as a "black" disk; i.e, $(d\sigma/d\Omega)$ is given by

$$\frac{d\sigma}{d\Omega} = (p\sigma_T/4\pi)^2\left[J_1(Rp\theta)/(Rp\theta/2)\right]^2 \qquad \text{(IV.5)}$$

the differential cross section for elastic scattering by

such a disk whose radius is R. It is reasonable that, over the small values of t covered in this experiment, it not be necessary to include any inelastic term in the differential cross section in equation (IV.3) for the heavy elements. For example, for lead at the largest value of $|t|$ seen by our counters, we estimate the elastic differential cross section to be $\gtrsim 80$ times larger than the inelastic differential cross section; for beryllium the factor is $\gtrsim 8.5$. (See Appendix H.)

For small values of the argument of the Bessel function, (IV.4) can be written as

$$\frac{d\sigma}{d\Omega} \approx (p\sigma_T/4\pi)^2 \exp\left[-(Rp\theta/2)^2\right]. \qquad \text{(IV.6)}$$

This result can be obtained by considering the power series expansions of $J_1(x)$ and e^{-x}. Since $|t| \approx (p\theta)^2$ for small θ, we have

$$\frac{d\sigma}{d\Omega} \approx (p\sigma_T/4\pi)^2 \exp\left[-R^2|t|/4\right] \qquad \text{(IV.7)}$$

In Table 6 we show the values of $(\sigma_T - \sigma_4)$ expected from such a model. The values of R are taken from the work of Bellettini <u>et al</u>.[34], but the results listed are not strongly dependent on R. (This last fact can be seen by using (IV.6) in (IV.3), performing the integration and then expanding the result in powers of $R^2(p\theta)^2/4$. For small values of this last quantity, $(\sigma_T - \sigma_4)$ is independent of R.) We shall call $(\sigma_T - \sigma_4)$ the defect in σ_4.

TABLE 6

EXPECTED VALUES OF DEFECTS IN THE D^4 PARTIAL CROSS SECTIONS AT SEVERAL MOMENTA

Element	R (fm)	$\sigma_T - \sigma_4$ (mb)		
		11.8 GeV/c	16.9 GeV/c	25.4 GeV/c
Be	3.47			0.1
C	3.24	0.04	0.2	0.3
Al	4.15			1.4
Cu	5.60	1.2	2.3	5.0
Cd	6.2†			11.4
W	7.4†			23.3
Pb	7.50	7.0	13.6	28.8

†Interpolated from the data.

One might object that we should average the integral in (IV.3) over the momentum spectrum of the neutrons for our case. We have instead chosen to use the average value of the neutron momentum in (IV.3), because the difference between the D^4 partial cross section defects calculated the two different ways turns out to be only a negligible percentage of the total cross section.

We have used equation (IV.7) as a guide in parametrizing our extrapolations--namely, we assume the form

$$\ln\left(\frac{d\sigma}{d\Omega}\right) = A + Bt \qquad \text{(IV.8)}$$

To see whether the final extrapolated total cross section is

very dependent on this parametrization, we have also tried

$$\frac{d\sigma}{d\Omega} = C + Dt \qquad \text{(IV.9)}$$

In Tables 7 through 9 we list the partial cross section data we obtained. These data have been corrected for the effects discussed in section B of this chapter. In line with our discussion of our analysis procedure above, we have listed the D4 partial cross sections, σ_4, and the differences between partial cross sections $(\sigma_4 - \sigma_2)$ and $(\sigma_2 - \sigma_1)$. For hydrogen and deuterium the latter two quantities are omitted, since the two smallest counters yielded the same partial cross sections, thereby indicating that the defect in σ_4 was negligible.

(We have had to discard the data from counter D3. Up to a point in the experiment the set of partial cross section differences $[\sigma_4 - \sigma_3]$, $[\sigma_3 - \sigma_2]$, $[\sigma_2 - \sigma_1]$ was consistent with satisfying equation (IV.8). However, at that point the D3 phototube became defective and had to be replaced. After its replacement the D3 partial cross sections were slightly lower than they were before this change. Unfortunately, we did not discover this problem until after the experiment had ended. We think we accidentally set the voltage much too high on the new tube, so that we counted Cerenkov light from the lucite light pipe of the counter. The counter would, therefore, have had a larger effective area than the area of its scintillator disk alone, and would thus have measured smaller partial cross sections

than it should have. As we have no way of confirming this speculation, we have decided that the only valid course to follow is to discard all the data from counter D3.)

TABLE 7

PARTIAL CROSS SECTION DATA. AGS ENERGY = 28.1 GEV.
TAS CUT = 20%

Element	σ_4 (mb)	$\sigma_4-\sigma_2$ (mb)	$\sigma_2-\sigma_1$ (mb)
H	38.8 ± 0.9		
Be	265.7 ± 6.0	0.2 ± 2.4	1.2 ± 1.5
C	328.1 ± 5.3	5.7 ± 2.3	11.4 ± 2.8
Al	653.4 ± 10.8	21.6 ± 1.7	30.1 ± 1.2
Cu	1250.5 ± 19.4	61.9 ± 2.4	81.9 ± 2.3
Cd	1895.0 ± 30.3	135.6 ± 12.9	214.6 ± 12.5
W	2715.0 ± 47.5	219.2 ± 27.1	368.6 ± 14.9
Pb	3018.3 ± 40.2	300.6 ± 16.4	348.4 ± 15.9

TABLE 8

PARTIAL CROSS SECTION DATA. AGS ENERGY = 21.3 GEV.
TAS CUT = 90%†

Element	σ_4 (mb)	$\sigma_4-\sigma_2$ (mb)	$\sigma_2-\sigma_1$ (mb)
H	38.5 ± 0.5		
D	73.6 ± 0.4		
C	341.3 ± 1.1	5.1 ± 0.8	6.6 ± 0.8
Cu	1260.7 ± 4.1	44.5 ± 2.2	61.8 ± 2.6
Pb	3078.9 ± 9.8	221.2 ± 4.2	275.0 ± 5.1

†Only σ_4 is 90%. The differences $\sigma_4-\sigma_2$ and $\sigma_2-\sigma_1$ are determined from the 100% TAS data.

TABLE 9

PARTIAL CROSS SECTION DATA. AGS ENERGY = 14.5 GEV.
TAS CUT = 70%†

Element	σ_4 (mb)	$\sigma_4-\sigma_2$ (mb)	$\sigma_2-\sigma_1$ (mb)
H	39.2 ± 0.5		
C	342.3 ± 1.8	1.8 ± 0.5	1.8 ± 0.4
Cu	1301.5 ± 8.3	19.5 ± 1.8	31.0 ± 2.6
Pb	3146.5 ± 19.0	123.6 ± 3.5	137.8 ± 3.2

†Only σ_4 is 70%. The differences $\sigma_4-\sigma_2$ and $\sigma_2-\sigma_1$ are determined from the 100% TAS data.

The errors listed in the above tables for the D4 partial cross sections are the quadratic combinations of the statistical errors, the accidentals correction errors and the uncertainties arising from disagreements between the two monitor normalizations. For the liquid targets the systematic errors discussed in section B of this chapter have also been included. For the solid targets an additional 0.3% error has been included to account for the impurities in those targets and uncertainties in their densities.

The statistical errors were obtained in the usual way; i.e.,

$$\Delta\sigma_4 = \left\{\left[\sum_{j=1}^{n}(\langle\sigma_4\rangle-\sigma_{4,j})\right]\Big/\left[n(n-1)\right]\right\}^{\frac{1}{2}} ,$$

where $\Delta\sigma_4$ is the statistical error, $\langle\sigma_4\rangle$ is the average

value of σ_4 determined from n measurements of σ_4, and $\sigma_{4,j}$ is the jth such measurement.

The errors listed for the partial cross section differences $\sigma_4-\sigma_2$ and $\sigma_2-\sigma_1$ take into account all the sources of uncertainty listed in the last paragraph, except, of course, the monitor normalization uncertainties, which are exactly zero for these differences. There is an additional systematic error which is not included and which is large compared to the tabulated errors. This error arises from backscattering and is discussed in Appendix E. We will account for this error by assuming an additional uncertainty in our inferred total cross sections equal to the difference between our experimentally determined D4 partial cross section defects and the expected ones listed in Table 6.

In Table 10 we list some examples of the D4 partial cross section defects determined from the data of Table 7. The box heading "Method I" means that the parametrization of $(d\sigma/d\Omega)$ given by equation (IV.8) was used in obtaining the defects. "Method II" means that the parametrization of equation (IV.9) was used. The errors quoted under these headings are statistical only. The final column of the table lists our estimates of the real errors in these defects. These estimates, as explained above, are given by the differences between the experimentally determined defects and those listed in Table 6.

TABLE 10

EXPERIMENTAL D4 PARTIAL CROSS SECTION DEFECTS DETERMINED FROM THE DATA OF TABLE 7.

Element	$\sigma_T - \sigma_4$ (mb)		Estimated Net Error (mb)
	Method I	Method II	
C	0.7 ± 0.4	0.7 ± 0.4	0.4
Al	3.2 ± 0.4	3.1 ± 0.4	1.8
Cu	7.8 ± 0.5	7.6 ± 0.5	2.8
Cd	19.1 ± 2.6	18.8 ± 2.6	7.7
W	30.2 ± 5.2	29.9 ± 5.1	6.9
Pb	47.2 ± 3.8	44.2 ± 3.8	18.4

CHAPTER V

RESULTS AND CONCLUSIONS

A. THE MEASURED TOTAL CROSS SECTIONS

Table 11 lists the total cross sections we have obtained following the analysis of our data by the procedures discussed in the preceding chapter. A discussion of the means used to obtain the mean neutron momenta, $\overline{P}$, listed in the table's box headings is given in Appendix A.

TABLE 11

NEUTRON-NUCLEUS TOTAL CROSS SECTIONS

Element	Total Cross Section (mb)		
	$\overline{P}$ = 11.8 GeV/c	$\overline{P}$ = 16.9 GeV/c	$\overline{P}$ = 25.4 GeV/c
$_1H^1$	39.2 ± 0.5	38.5 ± 0.5	38.8 ± 0.9
$_1D^2$		73.6 ± 0.4	
$_4Be^9$			265.7 ± 6.0
$_6C^{12}$	342.7 ± 2.1	342.2 ± 1.8	328.8 ± 5.3
$_{13}Al^{27}$			656.4 ± 10.9
$_{29}Cu^{64}$	1304 ± 9	1267 ± 8	1258 ± 20
$_{48}Cd^{112}$			1914 ± 31
$_{74}W^{184}$			2745 ± 48
$_{82}Pb^{207}$	3166 ± 25	3113 ± 25	3065 ± 44

B. COMPARISON WITH OTHER EXPERIMENTS

The results of our measurements of the np total cross section together with those of other experimenters are shown in Figure 13. The solid line is a hand fit to the data on the pp total cross section.[17-26] Except for the data of Denisov *et al.*[20], which was obtained by a (pd - pp) subtraction with corrections for shadowing, the points are all direct np measurements. Our data are in excellent agreement with those of Engler *et al.*,[13] and of Denisov *et al.* These three sets of measurements are consistent with $\sigma_T(np)$ being equal to $\sigma_T(pp)$ from 8 GeV/c to 60 GeV/c. The data of Kreisler *et al.*[2]) are somewhat lower in the 15 GeV/c to 22 GeV/c region, but the discrepancy is probably not statistically significant. (Furthermore, these authors have indicated that there were possibly poorly understood systematic effects that could have influenced these data.)

For deuterium our datum at 17 GeV/c is consistent, when compared with the proton data of Bellettini *et al.*,[27] Galbraith *et al.*[19] and Denisov *et al.*, with $\sigma_T(nd) = \sigma_T(pd)$, as was suggested in Chapter II from charge symmetry. The nd data of Parker *et al.*[15] and the pd data of Bugg *et al.*[17] and of Galbraith *et al.* at lower energies exhibit the same equality. It is difficult to compare the 27 GeV/c nd datum of Kreisler *et al.* with the pd data. While it certainly disagrees with the results of Denisov *et al.*, it would appear to agree with the data of Galbraith *et al.* ex-

trapolated to higher momenta.

To show how our neutron-heavy nucleus cross sections compare with those of other investigators, we present all of these data in Figures 15 through 19 for those elements for which a substantial amount of data has been reported in the literature. (The dashed and dashed-dotted lines in the figures are theoretical predictions which we will discuss in the next section of this chapter.) Again our results and those of Engler et al.[14] agree very well indeed. The data of Jones et al. [1] were taken in the same experiment as those of Kreisler et al. previously mentioned. They are in distinct disagreement with our results, but again we note that these authors have stated that larger systematic errors may be present than those indicated by the error bars shown with their data. The earlier data of Engler et al.[11] (shown as "Engler et al. I" in the figures) have been moved from a momentum of 10 GeV/c as originally published to 9 GeV/c as recently amended by those authors.[14] When extrapolated back to lower energies our results and those of Engler et al. would appear to agree with the 5.7 GeV/c measurements of Parker et al.

Before we compare our neutron-heavy nucleus total cross sections with the proton-heavy nucleus total nuclear cross sections of Bellettini et al.[34], we note that we found it necessary to correct the latter data for Coulomb-nuclear interference effects which these authors had taken to be negligible. The corrections are discussed in Appendix

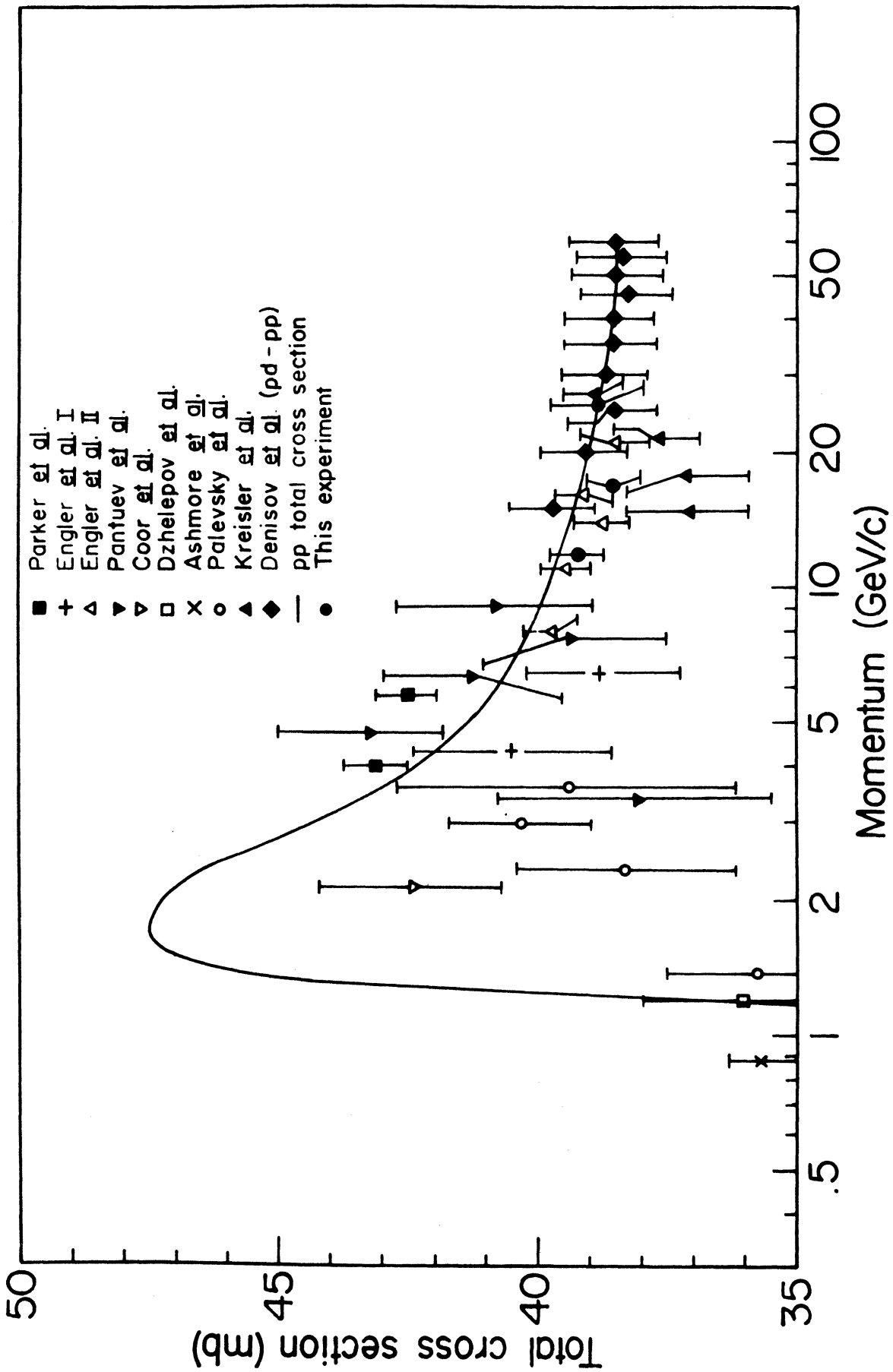

Fig. 13.--Nucleon-proton total cross sections

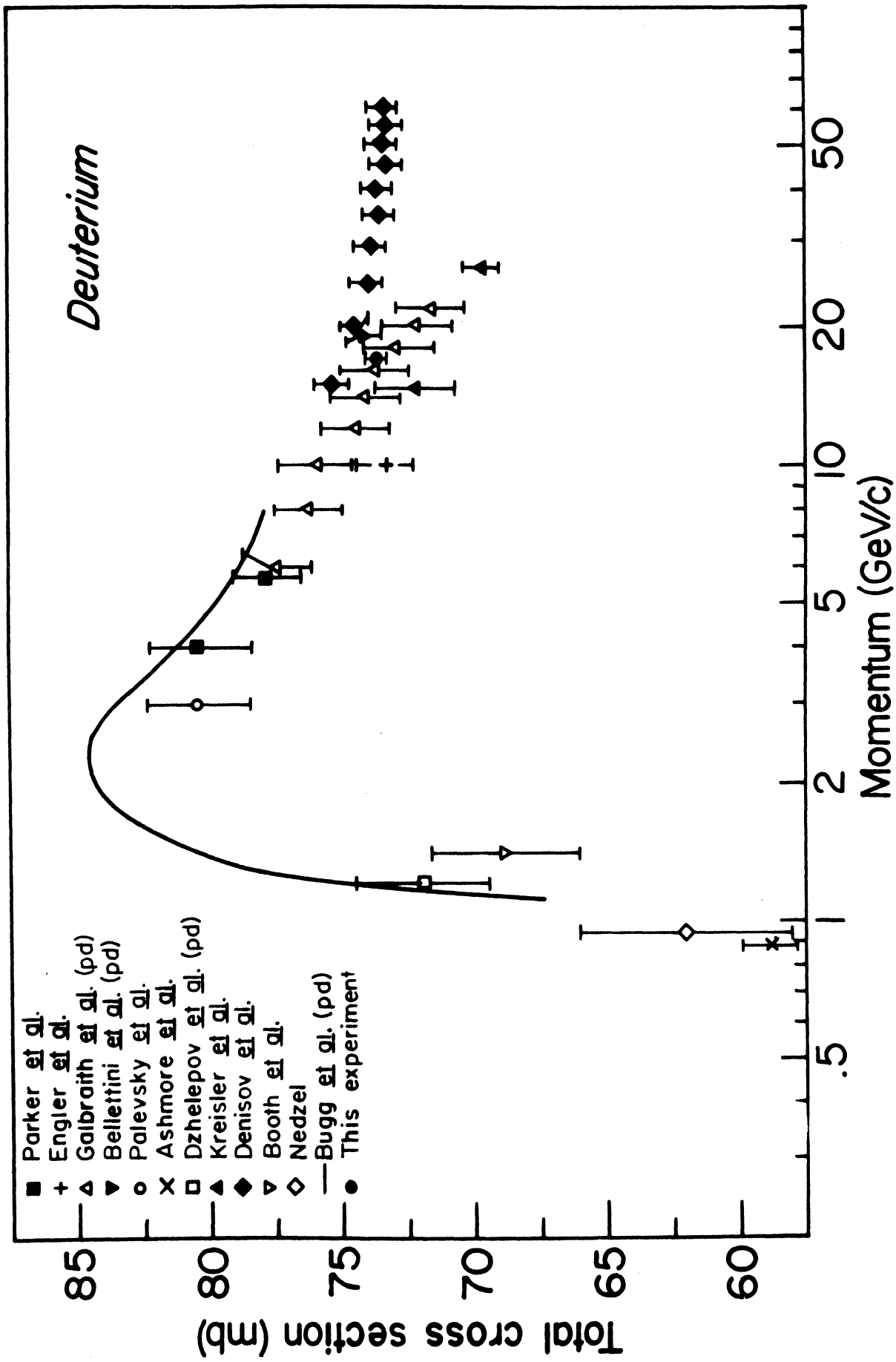

Fig. 14.--Nucleon-deuteron total cross sections

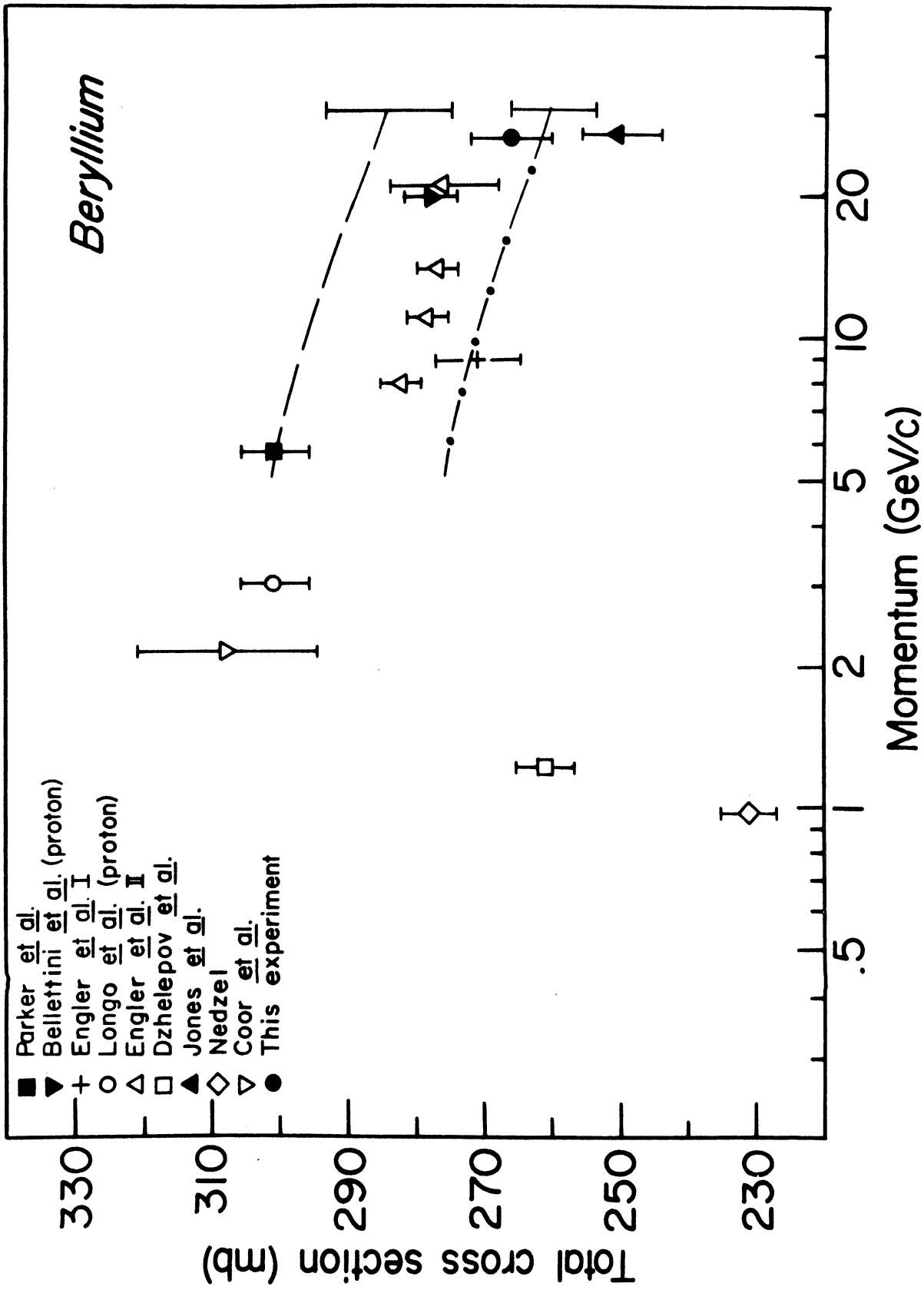

Fig. 15.--Nucleon-beryllium total cross sections

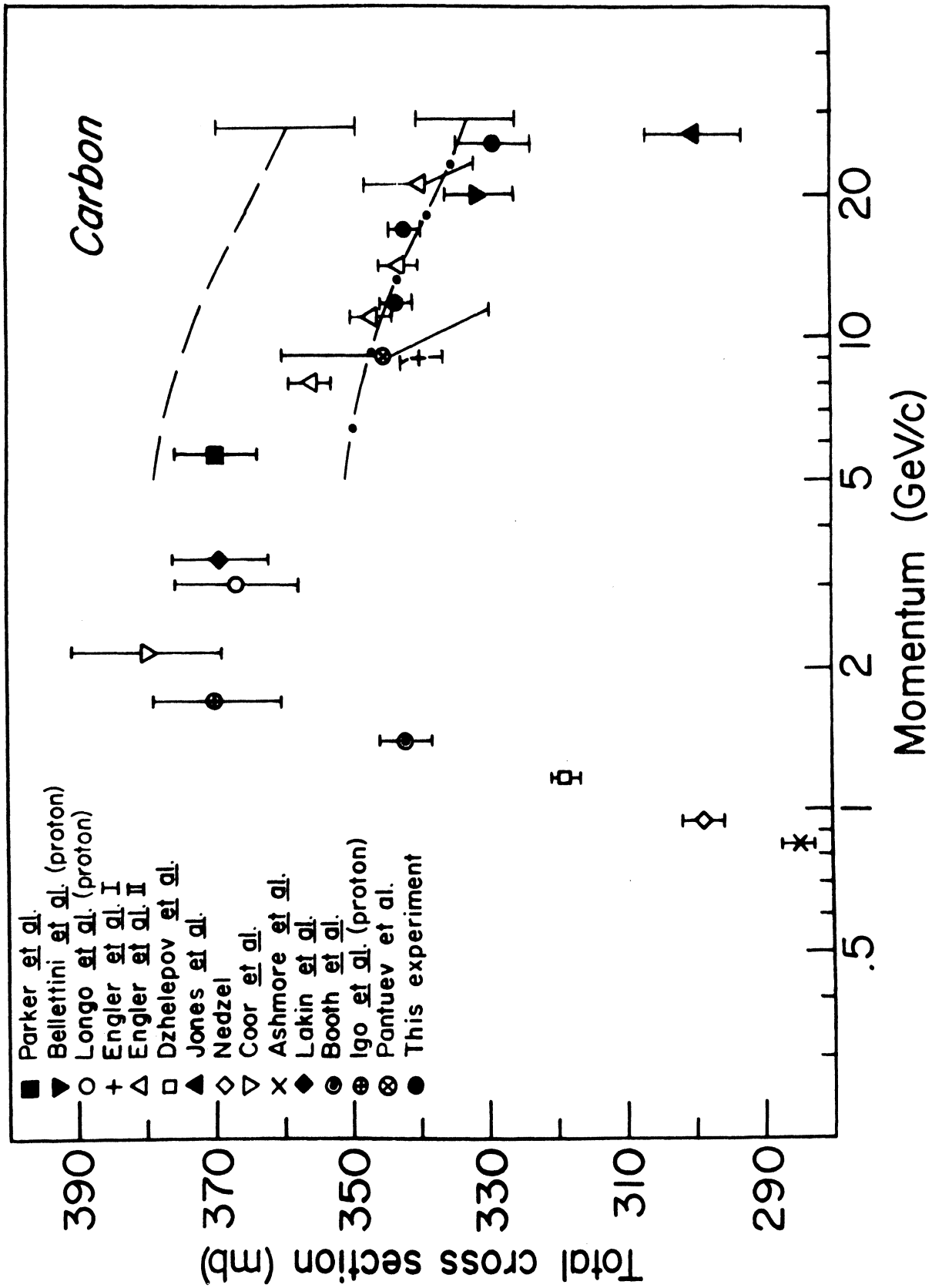

Fig. 16.--Nucleon-carbon total cross sections

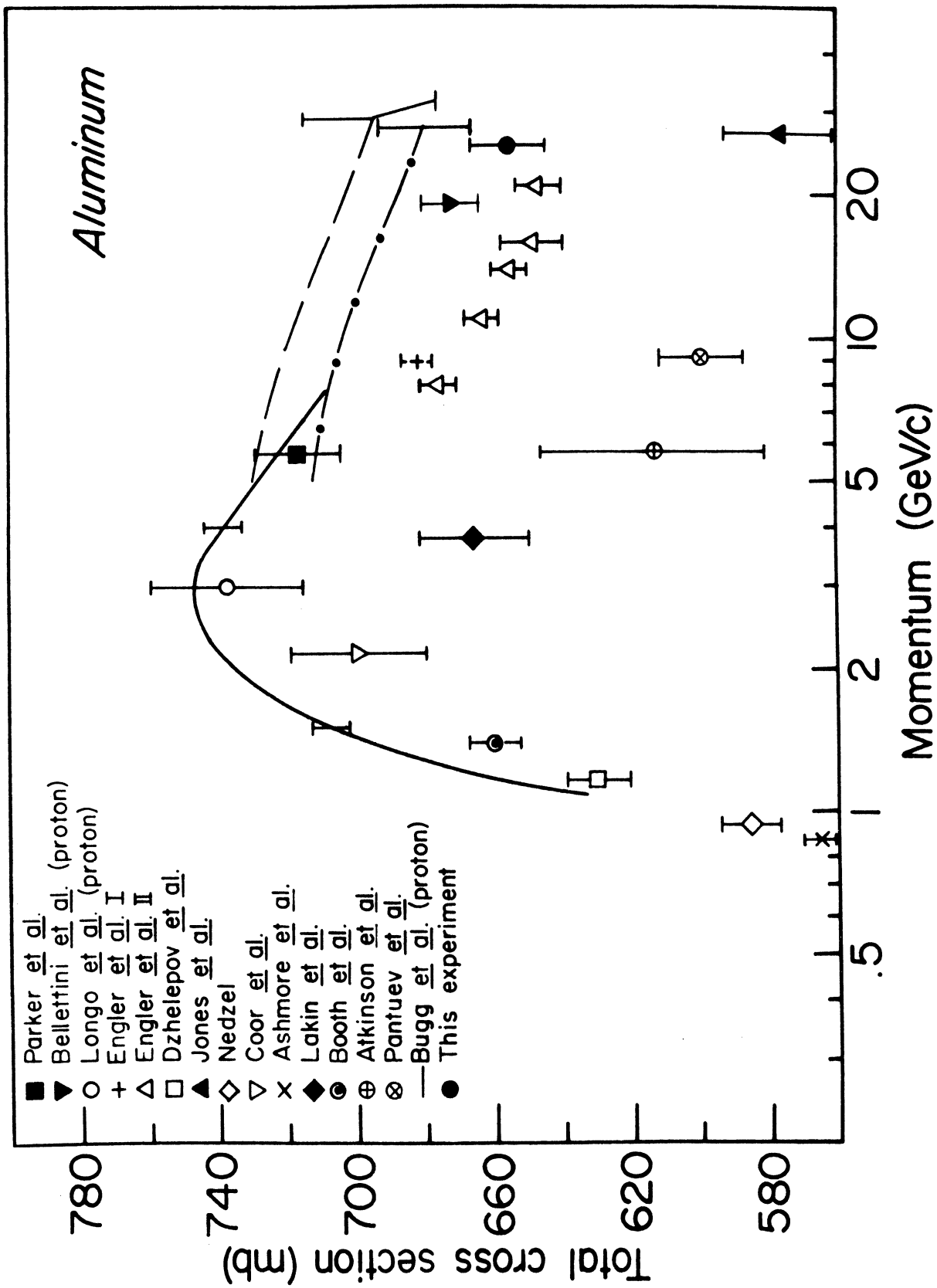

Fig. 17.--Nucleon-aluminum total cross sections

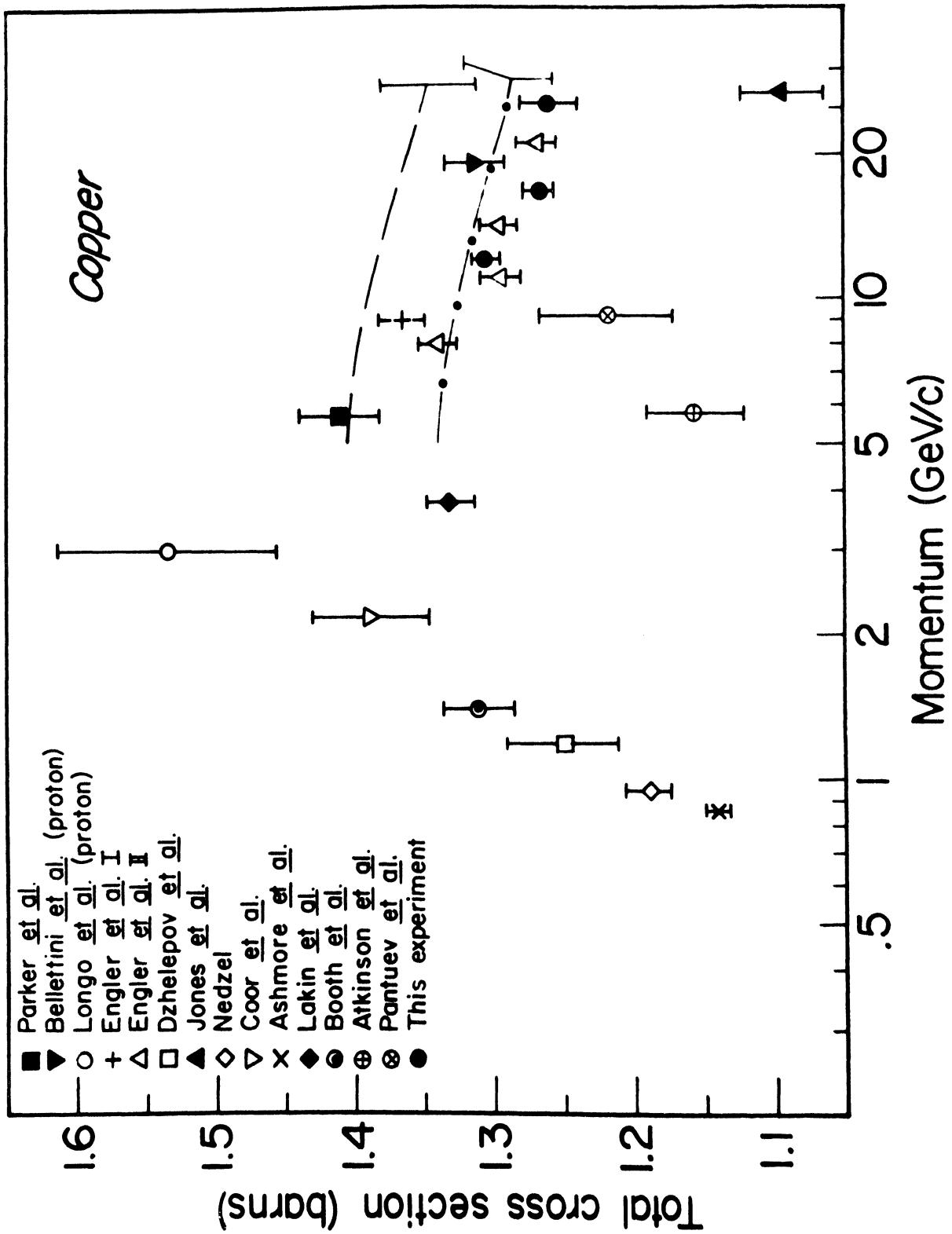

Fig. 18.--Nucleon-copper total cross sections

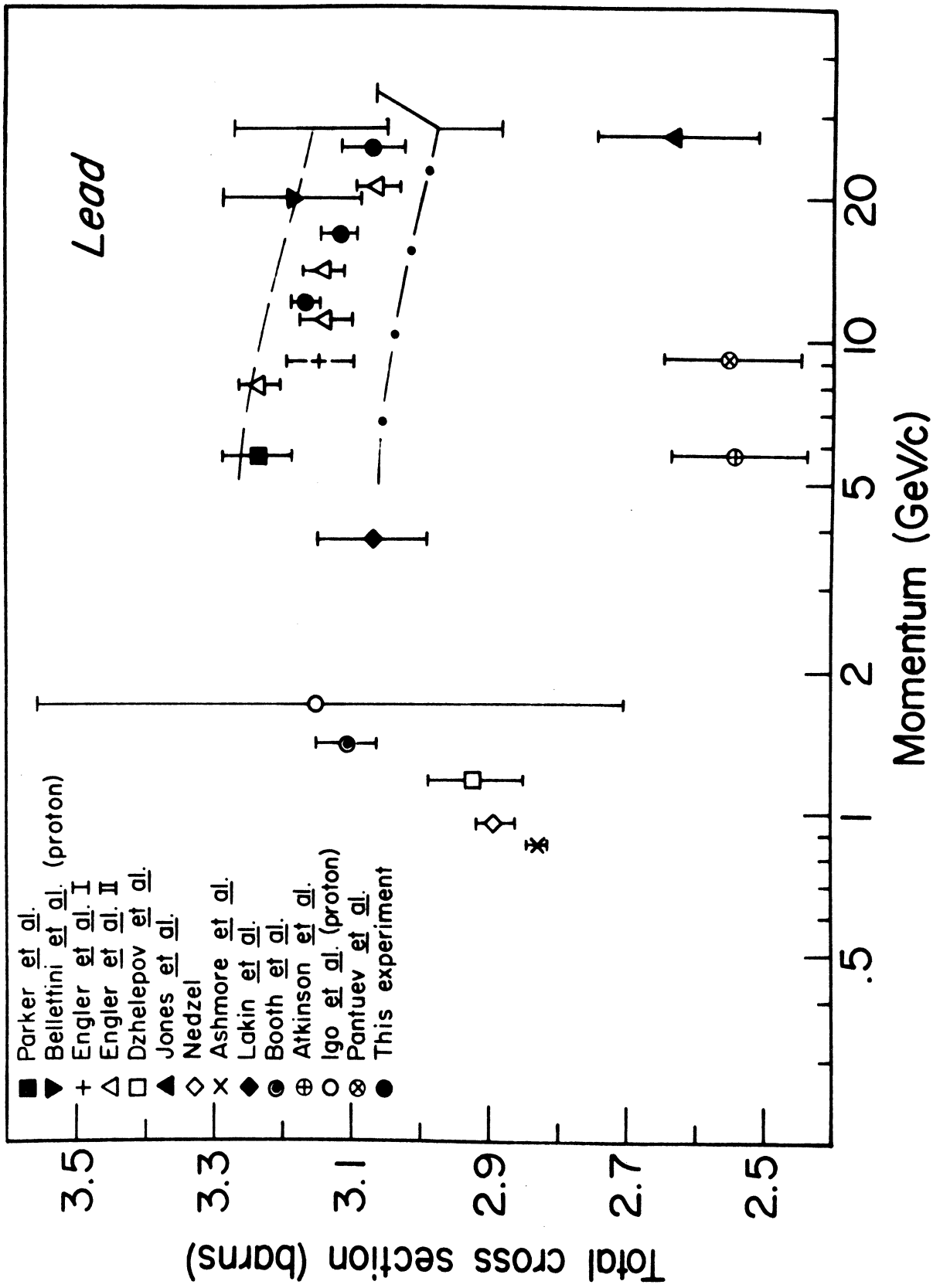

Fig. 19.--Nucleon-lead total cross sections

F. The proton data shown in the figures as "Bellettini *et al.*" include our corrections. The proton cross sections are almost consistent with being equal to the neutron cross sections, a not surprising result in view of the approximate equalities of the pp and np total cross sections.

C. COMPARISON WITH THEORY

In Figures 15 through 19 we also show the results of our calculations of total cross sections using equation (II.10) with Woods-Saxon nuclear density distributions. We shall refer to these calculations as "Glauber-Franco" calculations. The dashed line in each figure is the result of the calculation when the "strong interaction" Woods-Saxon parameters of Table 1 are used. The dashed-dotted line is the result of the calculation when the "electromagnetic" Woods-Saxon parameters are used. The other parameters--σ_N, α and β--were obtained from the proton-proton scattering data of references 17, 18 and 28. (We took σ_N to be equal to the pp total cross section in the spirit of our discussion of the apparent equalities of the pp and np total cross sections at high energies. We have, however, assigned σ_N a net error of 0.6 mb in our calculations to account for the uncertainties in the np total cross section and its slight differences from the pp total cross section.) At the ends of the theoretical curves are shown the average error to be assigned to these curves over the momentum range of the calculations. These uncertainties were found by varying

one at a time each of the five input parameters by one standard deviation to obtain the corresponding variation in the calculated result. These five latter variations were then added in quadrature to give the net uncertainty. We found that the largest source of error came from the uncertainties in the nuclear density parameters, which contributed about 90% of the net error.

Clearly, the figures show that, within errors, the Glauber-Franco calculations compare favorably with the experimental results. Unfortunately, the errors on the theoretical predictions are large--larger than on much of the experimental data--so that the favorable comparison is not so strongly convincing of the validity of the model as one would wish. Better-measured nuclear density distributions are certainly needed to tighten up the theoretical results. (We note here that in a recently circulated preprint[57] V. Franco has collected nuclear density parameters other than those which we have used and has employed them in doing calculations such as we have done. While the results of his calculations using these data are closer to the experimental results than are ours, the errors on his predictions are just as large as on ours, so that no better comparison of the model with the measured data is obtained.)

In view of the remarks in the last paragraph, it is clear that it will be difficult to assess the worth of any

refinement of the Glauber-Franco model, such as the inclusion of nuclear correlations. Further it will be hard to confirm any fundamental departures from the basic Glauber amplitude--such as those introduced by regenerative effects--unless these departures are rather large: on the order of 8% or more. Keeping these remarks in mind, let us proceed to look into the effects we have just mentioned.

In Table 12 we list for several elements at 12.0 GeV/c and 25.6 GeV/c the corrections, $\Delta\sigma_c$, that must be added to the Glauber-Franco model cross sections shown in Figures 15 through 19 in order to take into account a nonzero pair correlation length R_c. We give the results for R_c = +0.056 fm, as calculated from Figure 6, and for R_c = -0.4 fm as given by Bochmann and Margolis[48] as a reasonable upper limit on the correlation length. The calculations were done using Woods-Saxon density distributions, for which the parameters were taken from the "Strong Interaction" column of Table 1. Just as one would expect the corrections are not dependent on energy. Clearly the effect of nuclear correlations can not be seen at the current statistical levels of the experimental data and the theoretical calculations. One should probably add another uncertainty of about two percent to those shown on the theoretical predictions in Figures 15 through 19 to take into account our uncertain knowledge of the size of the correlation effects.

TABLE 12

EXAMPLES OF CHANGES IN THE CALCULATED TOTAL CROSS SECTIONS CAUSED BY NUCLEAR CORRELATIONS FOR TWO DIFFERENT CORRELATION LENGTHS

Element	$\Delta\sigma_c$ (mb)			
	R_c = +0.056 fm		R_c = -0.4 fm	
	11.8 GeV/c	25.4 GeV/c	11.8 GeV/c	25.4 GeV/c
Be	-1.0	-1.0	+7.0	+6.9
C	-1.4	-1.3	+9.7	+9.5
Al	-2.8	-2.7	+19.3	+18.6
Cu	-4.9	-4.8	+33.0	+31.9
Cd	-6.3	-6.1	+41.8	+40.4
W	-7.2	-7.3	+45.6	+46.1
Pb	-7.8	-7.8	+50.2	+50.6

In Table 13 we list for various elements at several momenta the corrections, $\Delta\sigma_R$, that must be added to the Glauber-Franco cross sections of Figures 15 through 19 to account for regenerative effects. We include calculations done with both the Bochmann and Margolis model and the Pumplin and Ross model, the latter by the improved calculational method we described in Section D of Chapter II. Three assumptions had to be made about the input that was required by these models because of lack of the necessary experimental data. The first was that the intermediate inelastic states couple only to the nucleon but not to each

TABLE 13

EXAMPLES OF CHANGES IN THE CALCULATED TOTAL CROSS SECTIONS CAUSED BY REGENERATIVE EFFECTS

Model	Momentum (GeV/c)	$\Delta\sigma_R$ (mb)		
		C	Cu	Pb
Pumplin and Ross	15.0	-16.6	-71	-123
	30.0	-20.5	-99	-179
Bochmann and Margolis	10.0	-3.6 ± 0.5	-17 ± 3	-32 ± 5
	15.0	-4.4 ± 0.6	-21 ± 3	-42 ± 6
	20.0	-4.7 ± 0.9	-24 ± 5	-49 ± 10
	25.0	-7.5 ± 2.1	-37 ± 10	-77 ± 22
	30.0	-9.4 ± 3.2	-46 ± 16	-100 ± 36

other, so that three-step processes like

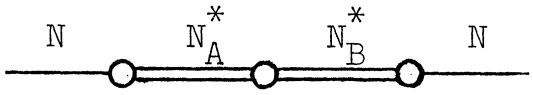

were not allowed. Such processes tend to make the calculated changes in the total cross sections slightly smaller in magnitude. The second assumption was that the phase of $N + N \rightarrow N + N^*$ was equal to that of NN elastic scattering. As long as the amplitudes for these processes are mostly imaginary, the results are not overly sensitive to this assumption. The third assumption was that the amplitude for $N + N^* \rightarrow N + N^*$ was the same as for $N + N \rightarrow N + N$. The amplitudes for $N + N \rightarrow N + N^*$ were obtained from the data

of reference 47. We list these amplitudes in Table 14. Only the amplitudes at t=0 are given, since we used equation (II.20) for the optical potential. To get the amplitudes at momenta other than those listed in the table, we interpolated linearly in momentum. A Woods-Saxon nuclear density was employed which used the "Strong Interaction" parameters of Table 1. No errors are quoted with the Pumplin and Ross predictions, as we did not know what the errors were on the data of Figures 4 and 5. It is probably reasonable to assign these predictions the same fractional errors as those on the Bochmann and Margolis results, since the data of Figures 4 and 5 came from the same experiment as the data of Table 14.

Clearly, because of the size of the uncertainties on the theoretical curves shown in Figures 15 through 19, a single measurement is insufficient as a test of the predictions of Table 13. However, the point-to-point errors on the Glauber-Franco predictions are much smaller, since the uncertainties in the nuclear density parameters--the chief source of errors in the calculations--can then be ignored. Moreover, the corrections for the regenerative effects show a marked energy dependence. Thus a comparison of the momentum dependence of our data with that of the theoretical predictions provides a better check for the presence of regenerative effects. We list in Table 15 the differences between the total cross sections we measured at 11.8 GeV/c and at 25.4 GeV/c and the differences predicted by the var-

TABLE 14

AMPLITUDES FOR $N + N \rightarrow N + N^*$ AT t=0

Mass of N^* (GeV)	Momentum (GeV/c)	Absolute Value of Amplitude (fm)
1.40	10	3.92 ± 0.32
	15	5.49 ± 0.51
	20	7.46 ± 0.94
	30	15.52 ± 3.70
1.52	10	0.99 ± 0.15
	15	1.39 ± 0.15
	20	1.96 ± 0.20
	30	3.13 ± 0.43
1.68	10	1.80 ± 0.07
	15	3.17 ± 0.16
	20	4.14 ± 0.28
	30	7.00 ± 0.56
2.19	20	1.96 ± 0.22
	30	2.73 ± 0.50

ious models. Within errors any of the models is consistent with the data. The regenerative effects--if they are present at all--are too small to be resolved at these energies.

TABLE 15

MEASURED AND PREDICTED DECREASES IN TOTAL CROSS SECTIONS BETWEEN 11.8 GEV/c AND 25.4 GEV/c

	Decrease (mb)		
	C	Cu	Pb
This Experiment	14 ± 6	46 ± 22	101 ± 50
Glauber-Franco	10 ± 5	35 ± 15	62 ± 29
Glauber-Franco plus Bochmann-Margolis	14 ± 6	54 ± 19	104 ± 42
Glauber-Franco plus Pumplin-Ross	14	60	113

The trend, indicated in Table 13, of increasingly larger drops in the total cross sections with increasing momentum from regenerative effects is expected by J. S. Trefil[58,59] to continue at higher energies. However, he points out that cosmic ray experiments[60,61] show that the inelastic cross section for protons on protons is constant up to about 10^3 GeV and presumably above. Thus the regenerative effects should saturate at some energy. Making some definite assumptions about how the total inelastic cross section available is shared among the possible inelastic states as a function of mass, Trefil predicts that the saturation will occur before 400 GeV with the total cross sections decreasing about 10% from their values at 30 GeV.[59] The former energy will be available soon at National Accelerator Laboratory, so that a total cross section experiment done there may clarify the situation with respect to

regenerative effects.

D. CONCLUSIONS

We have measured the np total cross section at average neutron momenta of 11.8 GeV/c, 16.9 GeV/c and 25.4 GeV/c with accuracies of 1.3%, 1.3% and 2.3% respectively. The values obtained are consistent with $\sigma_T(np) = \sigma_T(pp)$ and thus indicate that the imaginary parts of the I=0 and I=1 amplitudes are equal at zero degrees at these momenta.

Our single measurement of the neutron-deuteron total cross section at an average momentum of 16.9 GeV/c to an accuracy of about 0.6% agrees very well with the proton-deuteron cross section at nearby energies. Thus we see no evidence for any violation of charge independence--nor, therefore, of the weaker principle of charge symmetry--in nucleon-nucleon interactions.

The Glauber model, even with the simplifying assumptions of spherically symmetric nuclei and no correlations among nucleons in a nucleus is capable of reproducing the experimental data on neutron-nucleus cross sections well. The accuracies of this model's predictions are, however, limited by the uncertainties in the available data on the sizes of nuclei. On the other hand, the experimental results are also consistent with the modification of this model by the inclusion of either nuclear correlations or regenerative effects--in the latter case even when we couple not only resonances to the nucleon but also the non-

resonant background. With respect to this last point we note again that, though the original calculations of Pumplin and Ross[46] appeared to give decreases in the neutron-nucleus total cross sections which were too large to agree with the experimental results, we have shown in a more careful calculation that the expected decrease is consistent with the experimental measurements.

As discussed in Appendix A, the use of a total absorption spectrometer in this experiment provided a modest improvement--about 30%-- in the neutron energy resolution at 28 GeV over that which could have been obtained without the use of a TAS. At 14.5 GeV the improvement even for a 10% TAS cut--which is about the smallest cut one would use, considering the combination of low rates to which the experiment must be restricted and the running times reasonably available--is about 25%. However, this last figure corresponds to only about a 1 GeV decrease in the FWHM of the effective neutron spectrum. Taking into account the difficulties a TAS introduces--a sizeable rate effect that necessitates running at low intensities, and backscattering--one might conclude that it is not clear that it is worthwhile to employ such a device at these energies, especially since the total cross sections are only slightly energy dependent. However, one did not know a priori that there was not a large number of low energy neutrons ($\leq$1 GeV) in the beam. The cross section of these neutrons is very different from that at high energies. Some energy discrimination was cer-

tainly necessary so that we could be confident that our results were not biased by such a source.

APPENDIX A
TAS RESPONSE

It would have been desirable to investigate the energy response of the TAS with monoergic beams of protons, which could have been expected to produce hadronic showers in the device very similar to those yielded by neutrons. Since our beam was taken off the SEB target at 0°, however, the Health Physics Group at the AGS were steadfastly opposed to protons being sent down our line for fear that the entire internal beam might somehow be dumped down that line. As a result it was necessary to try to determine the TAS response indirectly by measuring the TAS pulse height spectra for our neutron beam at several AGS internal energies, thence unfolding the response function from these data and a knowledge of the neutron spectra incident on the TAS. This method is not completely satisfactory, because one makes simplifying assumptions about the expected TAS response function, and because the neutron spectrum from the SEB beryllium target is not known so well as one would like.

The most satisfactory neutron spectrum tried in the unfolding process was measured by one of the previously mentioned experiments performed in the same neutron beam upstream of our experiment[62]. This spectrum is shown in Figure A.1. This spectrum was obtained for an AGS internal beam energy of 28.14 GeV/c. To obtain the neutron spectra at the other AGS energies, we scaled this plot according to those momenta. This procedure is not without justification.

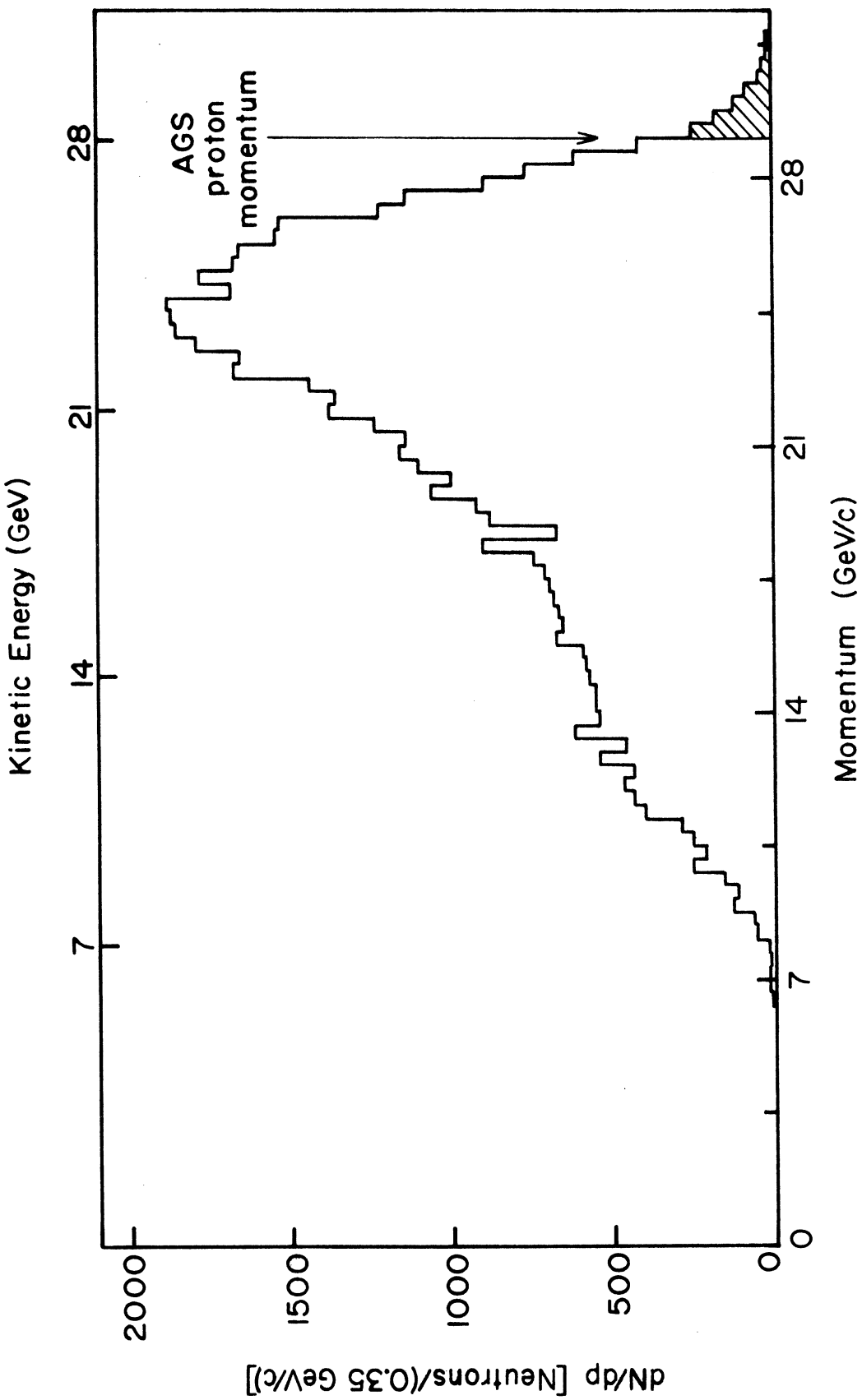

Fig. A.1.--Incident neutron spectrum for AGS proton energy of 28.1 GeV.

A compilation of secondary particle spectra by Hagedorn and co-authors[3] indicates that such a scaling rule holds very well over a broad range of momenta.

The model we chose for the TAS response function was based on data obtained from direct measurements - with mono-energetic protons - of the response of a very similar device used by Engler et al. Their results were that the full width at half maximum (FWHM) of the pulse height spectra from their TAS was a constant, that the response function was approximately Gaussian in shape at energies greater than the FWHM, and that the pulse height increased linearly with energy. At energies comparable to the FWHM and below it their pulse height spectra are no longer symmetric about the peak in those spectra. The distortion is such that the FWHM still is the same as at higher energies[63].

We built the findings discussed in the last paragraph into our model for the unfolding fit and obtained the following equation

$$N_{ob}(E_{ob}) = \frac{2\eta}{\sqrt{\pi}}\int_0^{E_P} N_{in}(E)\Big\{\Big[\exp[-(E-E_{ob})^2 \ln 2/\Gamma_1(E)^2]\,\theta(E_{ob}-E)$$

$$+\exp[-(E-E_{ob})^2 \ln 2/\Gamma_2(E)^2]\,\theta(E-E_{ob})\Big]\sqrt{\ln 2}/$$

$$\Big[\Gamma_1(E) + \Gamma_2(E)\,\mathrm{erf}\big(E\sqrt{\ln 2}/\Gamma_2(E)\big)\Big]\Big\}dE, \qquad (A.1)$$

where E_P is the AGS proton beam energy;

$N_{in}(E)$ is the neutron spectrum from the SEB target;

$N_{ob}(E_{ob})$ is the observed energy spectrum from the TAS;

η is a normalization constant, $\eta = \int N_{ob}(E)dE/\int N_{in}(E)dE$;

$\Gamma_1(E)$ is the half width at half maximum (HWHM) of the resolution function on the high energy side at incident energy E;

$\Gamma_2(E)$ is the HWHM of the resolution function on the low energy side at incident energy E;

$\theta(\tau)$ is the function $\theta(\tau) = 1$ if $\tau > 0$ and $\theta(\tau) = 0$ if $\tau < 0$;

erf(x) is the error function.

Recalling the discussion in the last paragraph, we also require

$$\Gamma_1(E) + \Gamma_2(E) = 2\Gamma,$$

where 2Γ, the FWHM, is a constant to be determined from the fit. Further, we require that

$$E_{ob} = aP_{ob} + b,$$

where P_{ob} is the pulse height observed in the TAS and a and b are constants to be determined from the fit. We also require that

$$\Gamma_2 = \Gamma_1 = \Gamma, \text{ if } \Gamma_1 \leq \tfrac{1}{2}E, \text{ or}$$

$$\Gamma_2 = E/2, \text{ if } \Gamma_1 > \tfrac{1}{2}E.$$

Equation (A.1) then becomes

$$N_{ob}(E_{ob}) = \frac{2\eta}{\sqrt{\pi/\ln 2}}\int_0^{E_P} N_{in}(E)\Big\{\Big[\exp[-(E-aP_{ob}-b)^2\ln 2/\Gamma^2]\times$$

$$\theta(E-2\Gamma)/\Gamma[1 + \mathrm{erf}(E\sqrt{\ln 2}/\Gamma)]\Big] +$$

$$\Big[\exp[-(E-aP_{ob}-b)^2\ln 2/(2\Gamma-E/2)^2]\theta(aP_{ob}+b-E) +$$

$$\exp[-(E-aP_{ob}-b)^2 \ln 2/(E/2)^2]\theta(E-aP_{ob}-b)\Big]\theta(2\Gamma-E)/$$

$$\Big[(2\Gamma-E/2) + (E/2)\mathrm{erf}(2/\sqrt{\ln 2})\Big]\Big\}dE. \qquad (A.2)$$

Having determined the fit variables from a non-linear maximum likelihood procedure using equation (A.2) and the observed TAS pulse height and incident neutron spectra, we then can determine what the effective neutron spectrum participating in a cross section measurement was for a specified cut on the TAS pulse height. This spectrum is easily shown to be given by

$$N_{eff}(E) = \frac{N_{in}(E)}{\sqrt{\pi/4\ln 2}} \int_{aP_{cut}+b}^{\infty} \Big\{\exp[-(E'-E)^2 \ln 2/\Gamma^2]\theta(E-2\Gamma)/$$

$$\Gamma[1 + \mathrm{erf}(E\sqrt{\ln 2}/\Gamma)] + \Big[\exp[-(E'-E)^2 \ln 2/(2\Gamma-E/2)^2$$

$$+ \exp[-(E'-E)^2 \ln 2/(E/2)^2\Big]\theta(2\Gamma-E)/\Big[(2\Gamma-E/2) +$$

$$(E/2)\mathrm{erf}(2/\sqrt{\ln 2})\Big]\Big\}dE', \qquad (A.3)$$

where $N_{eff}(E)$ is the effective neutron spectrum; and

P_{cut} is the minimum pulse height required from the TAS.

P_{cut} is determined by solving the equation

$$\frac{\int_{aP_{cut}+b}^{\infty} N_{ob}(E_{ob})dE_{ob}}{\int_{b}^{\infty} N_{ob}(E_{ob})dE_{ob}} = \text{Fraction of TAS counting rate passing the discriminator.} \qquad (A.4)$$

In Table A.1 we show the results of the fits at the three AGS internal beam energies used in the experiment.

TABLE A.1

VALUES OF THE PARAMETERS DETERMINED FROM THE PULSE HEIGHT SPECTRUM FITS

Parameter	AGS Kinetic Energy		
	14.5 GeV	21.3 GeV	28.1 GeV
2Γ (GeV)	11.3 ± 0.11	11.0 ± 0.2	11.3 ± 0.15
a (GeV)	0.50 ± 0.01	0.41 ± 0.01	0.44 ± 0.01
b (GeV)	0.68 ± 0.16	1.49 ± 0.19	0.25 ± 0.18

In Table A.1, if our model for the fit is correct, the quantities 2Γ (the FWHM), a and b should be the same at all three energies. This requirement holds well for 2Γ, but not so well for a and b. In all cases a and b turned out to be highly correlated in the fit (correlation coefficient ≈ 0.9), and b was strongly influenced by the low end of the input spectra where the neutron spectrum of Figure A.1 is most poorly determined.[62]

Table A.2 shows a variety of effective spectra parameters for different TAS pulse height cuts at the three AGS energies. Figure A.2 shows plots of the effective spectra at the highest AGS energy for several pulse height cuts. The pulse height spectra that were used in the fitting process are shown in Figure A.3.

Actually the process we have used for determining the effective neutron spectrum is not entirely satisfactory. χ^2 for the fits using equation (A.2) was very poor--the con-

TABLE A.2

THE AVERAGE BEAM MOMENTUM, $\overline{P}$, AND THE FWHM IN GEV/c FOR VARIOUS TAS PULSE HEIGHT CUTS

TAS Cut	AGS Internal Beam Energy					
	28.1 GeV		21.3 GeV		14.5 GeV	
	$\overline{P}$	FWHM	$\overline{P}$	FWHM	$\overline{P}$	FWHM
10%	25.8	4.8	19.3	4.0	12.4	2.8
20%	25.4	5.3	19.0	4.4	12.3	2.9
40%	24.7	5.9	18.4	4.8	12.1	3.6
60%	23.9	6.6	17.9	5.1	11.9	3.8
70%	23.5	6.8	17.6	5.3	11.8	3.9
90%	22.3	8.3	16.9	6.3	11.6	4.4
100%	21.5	8.4	16.4	6.4	11.4	4.5

fidence levels for the fits were $\leqslant$ 1%. Moreover, it is not clear whether this last result is due to poor knowledge of the incident neutron spectrum or to a poor choice of a model for the TAS resolution function. There was almost certainly a bias in the measurement of the spectrum of Figure A.1, such that the spectrum is untrustworthy below about 10 GeV/c.[64] We tried allowing modifications of this spectrum in our fits by multiplying it by a Chebyshev polynomial series with parameters to be determined in the fitting process. The results were unsatisfactory. Essentially what we found is that one can not determine both the incident spectrum and the TAS resolution function from the pulse height spectrum--a result which is not unreasonable.

Having made the remarks of the last paragraph, we now point out that the determination of the intermediate parameters of Table A.1 is not our primary goal. Rather, what we seek to determine are the effective spectrum parameters of Table A.2. Fortunately, for any reasonable choice of incident neutron spectrum these parameters do not change much from the values given in Table A.2. For example, we also employed in our fitting procedure the zero degree secondary proton spectrum predicted by the thermodynamical model of Hagedorn et al.[3] As these authors do not know how to cut off this spectrum as the kinematical limit of the primary proton energy is approached, we required that their spectrum fall off near that limit like the spectrum in Figure A.1. The resulting effective spectrum parameters are given in Table A.3. They do not differ significantly from those given in Table A.2.

TABLE A.3

AS IN TABLE A.2, BUT WITH THE INCIDENT NEUTRON SPECTRUM GIVEN BY THE MODEL OF HAGEDORN ET AL.

TAS Cut	AGS Internal Beam Energy					
	28.1 GeV		21.3 GeV		14.5 GeV	
	$\overline{P}$	FWHM	$\overline{P}$	FWHM	$\overline{P}$	FWHM
10%	25.7	4.1	19.4	3.4	12.4	2.7
20%	25.3	4.7	19.1	3.8	12.4	2.9
40%	24.7	5.5	18.6	4.4	12.2	3.3
60%	24.0	6.5	18.1	5.0	12.0	3.8
70%	23.6	7.0	17.8	5.4	11.9	4.0
90%	22.5	8.3	17.1	6.3	11.7	4.4
100%	21.6	8.9	16.5	6.8	11.5	4.7

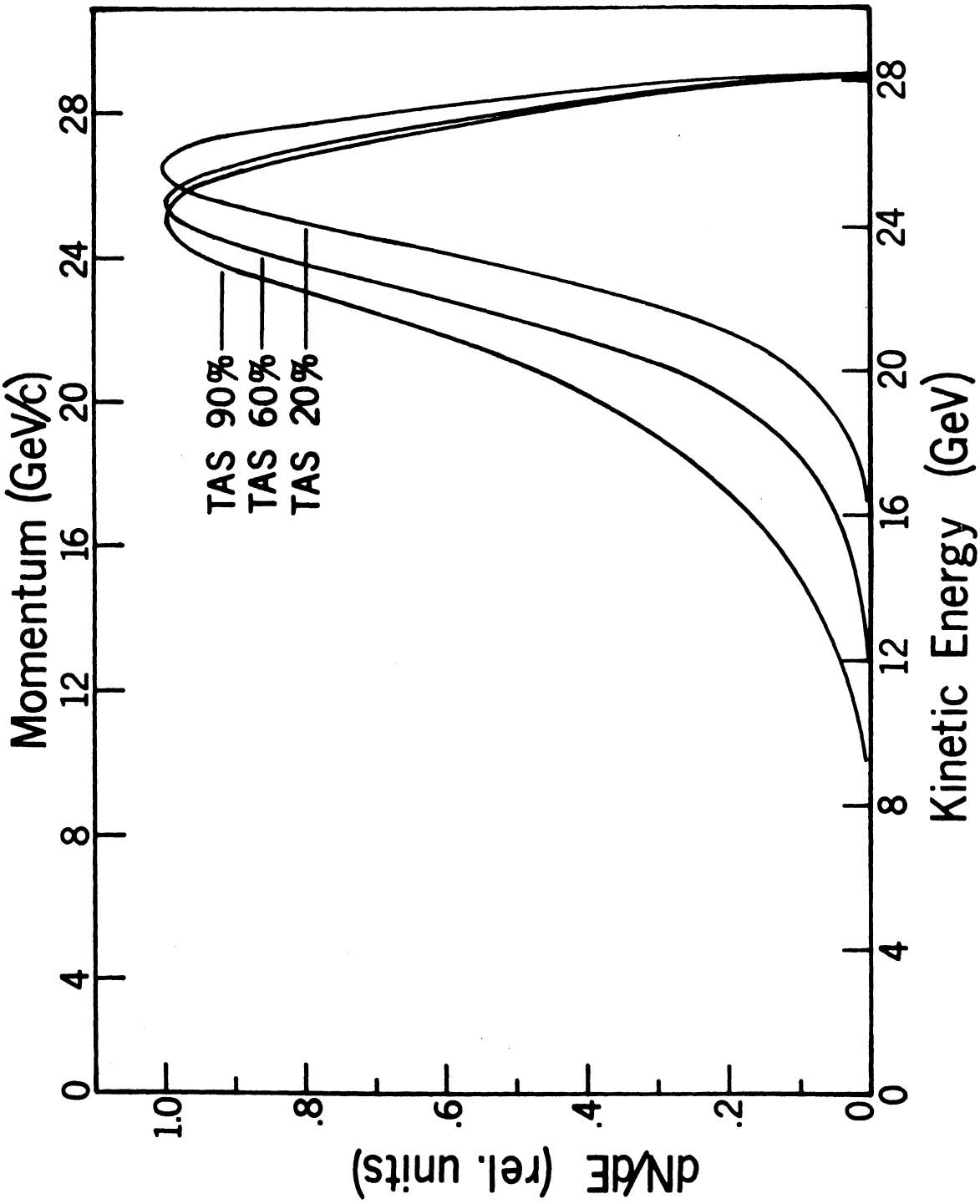

Fig. A.2--Effective neutron spectra at an AGS proton energy of 28.1 GeV for various pulse height cuts

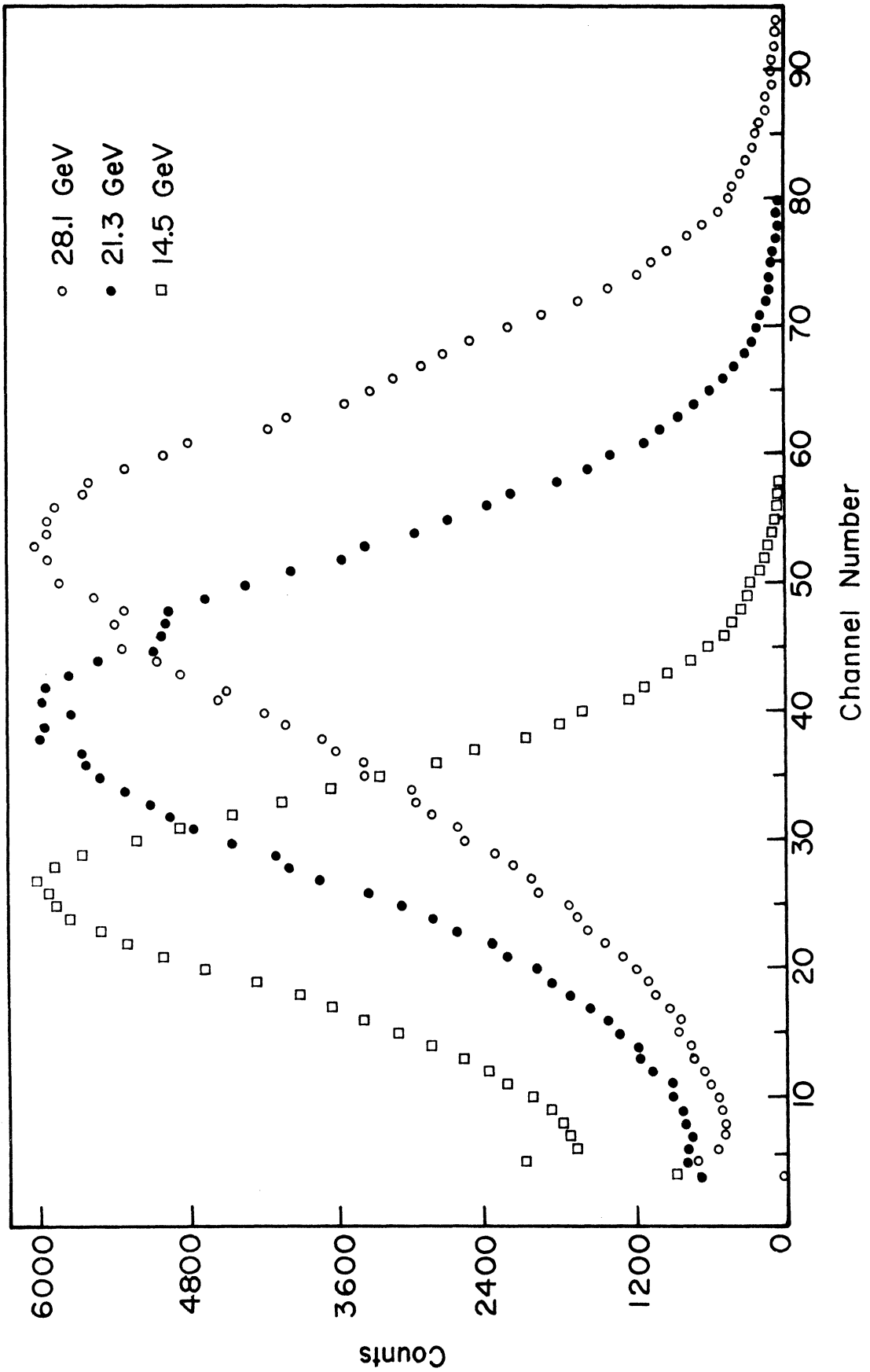

Figure A.3.--TAS Pulse height spectra for AGS proton energies of 14.5 GeV, 21.3 GeV and 28.1 Gev.

APPENDIX B

GEOMETRICAL EFFICIENCY OF THE TRANSMISSION COUNTERS

In this appendix we derive an expression for the geometrical efficiency of a transmission counter. The diagram below was copied from reference 50. (Our result differs from that given in reference 50.)

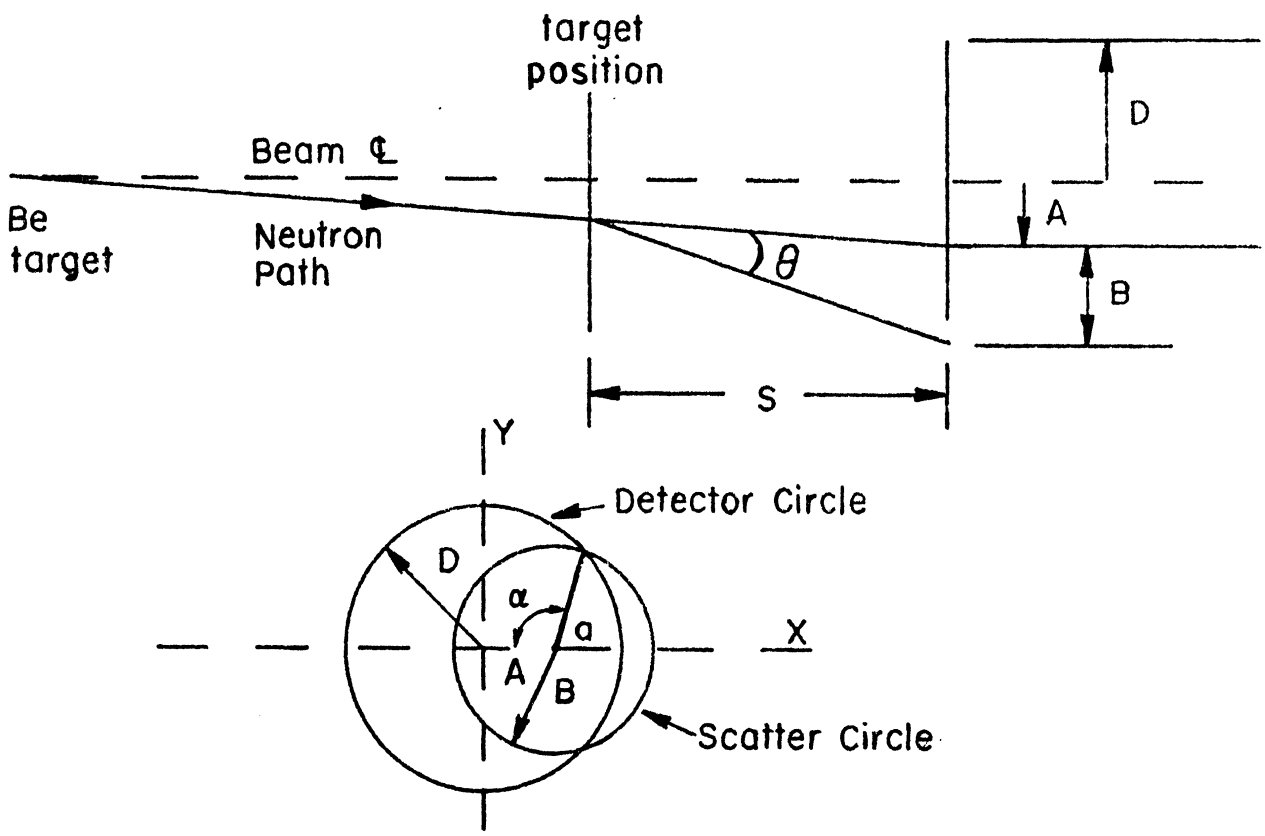

We want to know the probability, $E_i(\theta,R)$, that a neutron in a beam whose radius is R at the ith transmission counter will strike that counter when scattered through an angle θ by the experimental target. (We also call $E_i(\theta,R)$ the geometrical efficiency of the ith transmission counter.) In the diagram S is the target-counter distance; D is the

radius of the counter; A is the distance between the center of the counter and the point, a, on the counter where the neutron strikes it; $B=\theta S$ is the radius of the scatter circle. The probability that the neutron will strike the counter is

$$P(\theta,A) = \begin{cases} 1, & B\leq(D-A) \\ \alpha/\pi, & (D-A)<B\leq(D+A) \\ 0, & (D+A)<B \end{cases},$$

where the angle α is shown in the diagram.

If $(D-A)<B\leq(D+A)$, the scatter and detector circle intersect at the point

$$\left(x,y\right) = \left((A^2-B^2+D^2)/2A, \sqrt{2(A^2B^2+A^2D^2+B^2D^2)-A^4-B^4-D^4}/2A\right),$$

so that

$$\cos(\alpha) = (A-x)/B = (A^2+B^2-D^2)/2AB.$$

Thus,

$$P(\theta,A) = \Theta(D-A-B) + \Theta(B-D-A)\Theta(D+A-B)\frac{1}{\pi}\cos^{-1}[(A^2+B^2-D^2)/2AB],$$

where $\Theta(\tau)$ is the theta function $\Theta(\tau)=1$ if $\tau>0$, and $\Theta(\tau)=0$ if $\tau<0$.

If we assume a uniform intensity beam spot, then the probability for an unscattered neutron to strike the counter in the annulus of inner radius A and outer radius A+dA is

$$dP'(A) = (2A\cdot dA/R^2)\Theta(R-A).$$

Then

$$E_i(\theta,R) = \int P(\theta,A)dP'(A),$$

or

$$E_i(\theta,R) = \int_0^R \Big\{\pi\Theta(D-A-B) + \Theta(B-D+A)\Theta(D+A-B)\cos^{-1}[(A^2 + B^2-D^2)(2AB)^{-1}]\Big\} 2A(\pi R^2)^{-1} dA,$$

or

$$E_i(\theta,R) = \begin{cases} 1 & B<D-R \\ \int_0^R \Big\{\pi\Theta(D-A-B) + \Theta(B-D+A)\Theta(D+A-B) \\ \quad \times\cos^{-1}[(A^2+B^2-D^2)/2AB]\Big\}(2A/\pi R^2)dA & D-R<B<D+R \\ 0 & D+R<B. \end{cases}$$

Figure B.1 shows the geometrical efficiency for the smallest transmission counter for beam spots of various radii.

Clearly the geometrical efficiency, $F(\theta,R)$, for the annulus of scintillator lying between counters i and j is then

$$F(\theta,R) = |E_i(\theta,R) - E_j(\theta,R)|.$$

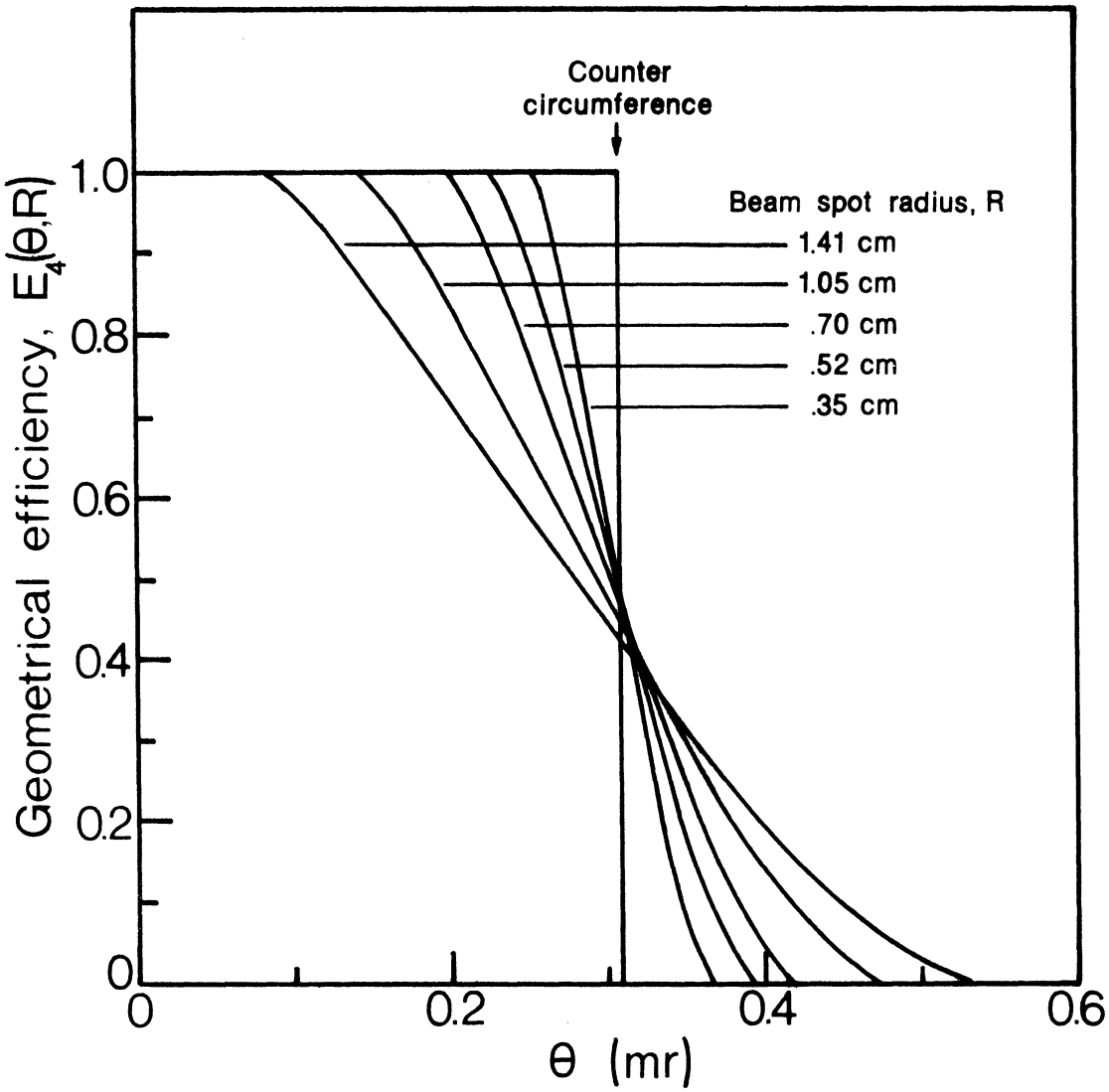

Fig. B.1--Geometrical efficiency for transmission counter D4 for beam spots of various radii

APPENDIX C

CORRECTIONS FOR COULOMB SCATTERING OF NEUTRONS

Because the neutron has a magnetic moment (an anomalous one equal to -1.913 Bohr magnetons), it can be scattered by the electric charge of a nucleus. However, one expects that the differential cross section for such Coulomb scattering should be small in comparison to that for nuclear scattering until one reaches very small momentum transfers and large atomic numbers. The momentum transfers involved in this experiment are small enough that we must make corrections--albeit small ones--for the Coulomb scattering of neutrons by our heavy targets. In this appendix we derive an approximate expression for the differential cross section for such scattering.

We start by assuming that the nucleus can be replaced by a static point charge of -Ze units, where Z is the atomic number of the nucleus, and e (<0) is the charge on an electron. We will multiply the resulting cross section by $F_C^2(A,q^2)$, the square of the Coulomb form factor of the nucleus to account for the spatial extent of the nucleus. A is the mass number of the nucleus, and q^2 is the square of the momentum transferred to the nucleus. (We warn the reader to distinguish between $v^2 \equiv |\vec{v}|^2$ and $v \cdot v \equiv v^\nu v_\nu$, where v is the four-vector $v = (v_0, \vec{v})$.) With these assumptions we can then simply lift equation (7.11) of Bjorken and Drell's book[65] for the differential cross section for the scat-

tering of electrons by a static charge -Ze:

$$\frac{d\sigma_C}{d\Omega} = \frac{4Z^2\alpha^2M^2}{|\vec{q}|^4} |\bar{u}(p_f,s_f)\gamma^0 u(p_i,s_i)|^2, \qquad (C.1)$$

replace the electron current by that for the neutron:

$$\bar{u}(p_f,s_f)\gamma^0 u(p_i,s_i) \rightarrow$$

$$\bar{u}(p_f,s_f)\left[\frac{i}{2M}\sigma_{0\nu}q^\nu \varkappa_N F_2(q^2)\right]u(p_i,s_i),$$

and multiply the result by $F_C^2(A,q^2)$ to get

$$\frac{d\sigma_C}{d\Omega} = \frac{Z^2\alpha^2}{|\vec{q}|^4}\left[\varkappa_N^2 F_2^2(q^2)F_C^2(A,q^2)\right]|\bar{u}(p_f,s_f)\sigma_{0\nu}q^\nu u(p_i,s_i)|^2. \qquad (C.2)$$

In the above expressions α is the fine structure constant, M is the mass of the neutron, $\varkappa_N$ is the magnetic moment of the neutron in units of Bohr magnetons, $F_2(q^2)$ is the neutron form factor (defined such that $F_2(0)=1$), and as usual $\sigma^{\mu\nu} = \frac{i}{2}[\gamma^\mu,\gamma^\nu]$.

We average (C.2) over initial spins and sum over the final spins to get

$$\frac{d\sigma_C}{d\Omega} = \frac{Z^2\alpha^2}{4|\vec{q}|^4}\left[\varkappa_N^2\, F_C^2(A,q^2)F_2^2(q^2)\right]S, \qquad (C.3)$$

where

$$S \equiv \frac{1}{2}\sum_{s_i}\sum_{s_f} |\bar{u}(p_f,s_f)[\gamma_0,\gamma_\nu]q^\nu u(p_i,s_i)|^2. \qquad (C.4)$$

Let us reduce the spin sum (C.4).

$$S = \tfrac{1}{2}\sum_{s_i}\sum_{s_f} |\bar{u}(p_f,s_f)\gamma_0\gamma_\nu q^\nu u(p_i,s_i) - \bar{u}(p_f,s_f)\gamma_\nu\gamma_0 q^\nu u(p_i,s_i)|^2.$$

But $\gamma_\nu\gamma_0 q^\nu = 2g_{0\nu}q^\nu - \gamma_0\not{q} = -\gamma_0\not{q}$, since $g_{0\nu}q^\nu = 0$ for elastic scattering. Then

$$S = 2\sum_{s_i}\sum_{s_f} |\bar{u}(p_f,s_f)\gamma_0\not{q}u(p_i,s_i)|^2$$

$$S = 2\sum_{s_i}\sum_{s_f} \bar{u}_\alpha(p_f,s_f)(\gamma^0\not{q})_{\alpha\epsilon}u_\epsilon(p_i,s_i)[\not{q}u(p_i,s_i)]^\dagger_\tau\gamma^{0\dagger}_{\tau\delta}u_\delta(p_f,s_f)$$

$$S = 2\sum_{s_i}\sum_{s_f} \bar{u}_\alpha(p_f,s_f)(\gamma^0\not{q})_{\gamma\epsilon}u_\epsilon(p_i,s_i)\bar{u}_\lambda(p_i,s_i)\not{q}_{\lambda\tau}\gamma^0_{\tau\delta}u_\delta(p_f,s_f)$$

$$S = 2\sum_{s_f} \bar{u}_\alpha(p_f,s_f)(\gamma^0\not{q})_{\alpha\epsilon}(2M)^{-1}(\not{p}_i+M)_{\epsilon\lambda}\not{q}_{\lambda\tau}\gamma^0_{\tau\beta}u_\beta(p_f,s_f)$$

$$S = \tfrac{1}{2}M^{-2}(\not{p}_f+M)_{\beta\alpha}[\gamma^0\not{q}(\not{p}_i+M)\not{q}\gamma^0]_{\alpha\beta}$$

$$S = \tfrac{1}{2}M^{-2}\mathrm{Trace}[\gamma^0\not{q}(\not{p}_i+M)\not{q}\gamma^0(\not{p}_f+M)]$$

$$S = \tfrac{1}{2}M^{-2}\mathrm{Trace}[\gamma^0\not{q}\not{p}_i\not{p}\gamma^0\not{p}_f + M^2\gamma^0\not{q}\not{q}\gamma^0]$$

$$S = 2M^{-2}\left\{M^2q\cdot q - E^2q\cdot q - [2(q\cdot p_i)(q\cdot p_f) - q^2p_f\cdot p_i] - E^2q\cdot q\right\}$$

where $E \equiv E_i = E_f$, and where $q\cdot q = q^\nu q_\nu \le 0$. Now $q\cdot p_i \approx 0 \approx q\cdot p_f$, since $\vec{q}$ is $\sim\perp\vec{p}_i$ and also $\sim\perp\vec{p}_f$, so that

$$S = 2M^{-2}q\cdot q(M^2 - 2E^2 + p_f\cdot p_i) = 2M^{-2}q\cdot q[-p^2(1+\cos\theta)],$$

where θ is the laboratory scattering angle. Then finally,

$$S = 4M^{-2}|\vec{q}|^2 p^2 \cos^2(\tfrac{1}{2}\theta), \qquad (C.5)$$

where we have used $q\cdot q = q^\nu q_\nu = -|\vec{q}|^2$. Then from (C.3)

$$\frac{d\sigma_C}{d\Omega} = Z^2\alpha^2 M^{-2} q^{-2} p^2 \varkappa_N^2 \, F_C^2(A,q^2) F_2^2(q^2)\cos^2(\tfrac{1}{2}\theta). \qquad (C.6)$$

For small scattering angles, $q^2 \approx p^2\theta^2$, so that we have

$$\frac{d\sigma_C}{d\Omega} \underset{\theta\to 0}{=} Z^2\alpha^2\varkappa_N^2 M^{-2}\theta^{-2} F_C^2(A,q^2) F_2^2(q^2) \qquad (C.7)$$

We now ask what the change is in the partial cross section measured by a transmission counter because some neutrons which should strike the counter do not because of their being Coulomb scattered. For the ith counter this change is

$$\delta\sigma_i = \int_0^{2\pi}\int_0^{\pi} (d\sigma_C/d\Omega)[1 - E_i(\theta,R)]\sin\theta\, d\theta\, d\varphi, \qquad (C.8)$$

where $E_i(\theta,R)$ is the geometrical efficiency for detection by the ith counter of a neutron scattered at an angle θ from a beam whose radius is R at the counter. The expression for $E_i(\theta,R)$ is given in Appendix B.

For small angles the form factors are fairly well represented by gaussian forms:[66]

$$F_C(A,q^2) = \exp[-\langle R_C^2(A)\rangle q^2/6], \qquad (C.9)$$

$$F_2(q^2) \approx \exp[-(.80\ \text{fm})^2 q^2/6], \qquad (C.10)$$

where $\langle R_C^2(A)\rangle^{\frac{1}{2}}$ is the root mean square Coulomb radius of the

nucleus whose mass number is A. Table C.1 gives the rms charge radii for the elements we have used in this experiment. We derived these numbers from the electromagnetic Woods-Saxon density parameters of Table . They are much the same as those given by Herman and Hofstadter.[66]

TABLE C.1

ROOT MEAN SQUARE CHARGE RADII FOR ELEMENTS USED IN THIS EXPERIMENT

Element	Z	A	rms radius fm
Be	4	9	2.192 ± 0.107
C	6	12	2.371 ± 0.101
Al	13	27	3.230 ± 0.099
Cu	29	64	3.880 ± 0.092
Cd	48	112	4.473 ± 0.095
W	74	184	5.283 ± 0.119
Pb	82	207	5.398 ± 0.105

With (C.9) and (C.10) expression (C.8) becomes

$$\delta\sigma_i \approx 2\pi Z^2\alpha^2\varkappa_N^2 M^{-2}\int_0^{\pi} [1 - E_i(\theta,R)]\cdot$$

$$\cdot\exp\left\{-[\langle R_C^2(A)\rangle + 0.64\mathrm{fm}^2]p^2\theta^2/3\right\}\frac{d\theta}{\theta} ,$$

where we have used small angle approximations for functions of θ. It is convenient to split this integral into two parts:

$$\delta\sigma_i \approx 2\pi Z^2\alpha^2\varkappa_N^2 M^{-2}\left\{\int_{(\theta_i-R/S)}^{(\theta_i+R/S)} [1-E_i(\theta,R)]\exp\left[-[\langle R_C^2(A)\rangle\right.\right.$$

$$\left.+0.64\mathrm{fm}^2]p^2\theta^2/3\right]\frac{d\theta}{\theta} + \int_{(\theta_i+R/S)}^{\infty}\exp\left[-[\langle R_C^2(A)\rangle\right.$$

$$\left.\left.+0.64\mathrm{fm}^2]p^2\theta^2/3\right]\frac{d\theta}{\theta}\right\}. \qquad (C.11)$$

We have made use of the facts that $E_i(\theta,R) = 1$ for $\theta<\theta_i-R/S$ and that $E_i(\theta,R)=0$ for $\theta>\theta_i+R/S$, where S is the target-TAS distance; we have also replaced the upper limit of π on the second integral by ∞. We then have

$$\delta\sigma_i \approx 2\pi Z^2\alpha^2\varkappa_N^2 M^{-2}\left\{\int_{(\theta_i-R/S)}^{(\theta_i+R/S)} [1-E_i(\theta,R)]\exp\left[-[\langle R_C^2(A)\rangle\right.\right.$$

$$\left.+0.64\mathrm{fm}^2]p^2\theta^2/3\right]\frac{d\theta}{\theta} - \tfrac{1}{2}\mathrm{Ei}\left[-[\langle R_C^2(A)\rangle+0.64\mathrm{fm}^2]\cdot\right.$$

$$\left.\left.\cdot p^2(\theta_i+R/S)^2/3\right]\right\} , \qquad (C.12)$$

where Ei(x) is the exponential integral function of x,

$Ei(x) = C_E + \ln|x| + \sum_{k=1}^{\infty} x^k/(k\cdot k!)$. C_E is Euler's constant, $C_E \approx 0.577215$. In our experiment $|x|$ was always less than 0.3, so that the series converged rapidly.

The integral in (C.12) must be done numerically. However, as an example, let us assume that R = 0--so that the integral is zero--and that we want to find $\delta\sigma_i$ for a lead target at p = 12 GeV/c = 60.8 fm^{-1} for our smallest transmission counter. We find that

$$\delta\sigma_4 = -9.33\ GeV^{-2}\cdot(-2.54) = 23.7\ GeV^{-2} = 9.2\ mb.$$

Thus we must subtract 9.2 mb or about (1/3)% from the cross section measured by the smallest transmission counter in this case.

To be really rigorous, we should average $\delta\sigma_i$ weighted by the effective neutron spectrum, N(p), over all momenta to obtain the true correction, $\delta\sigma_i^T$; i.e.,

$$\delta\sigma_i^T = \int_0^\infty \delta\sigma_i N(p)dp \Big/ \int_0^\infty N(p)dp. \qquad (C.13)$$

However, if we use for p in (C.12) the spectrum averaged neutron momentum, then $\delta\sigma_i$ differs from $\delta\sigma_i^T$ by a negligible amount--less than 10% in several cases we tried--so we have followed this latter approach in doing our calculations in order to simplify them.

As a final point we mention that, unlike the case when protons are the projectile particles, one does not expect to first order to have any Coulomb-nuclear inter-

ference term in the expression for the net differential scattering cross section. This result is true, however, only so long as Pomeron exchange between neutron and nucleus has a zero helicity-flip amplitude.

APPENDIX D

RATE MEASUREMENT AND RATE EFFECT

We noted in Chapter IV that we used the quantity TAS 100%·TAS $100\%_{delayed}$/(TAS 100% singles) as the measure of beam rate or real intensity. To see what we mean by rate and why this just mentioned quantity is a reasonable measure of it, consider the following two diagrams.

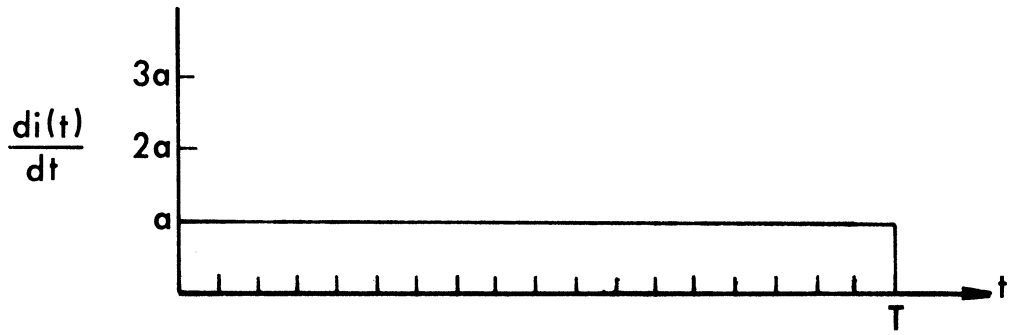

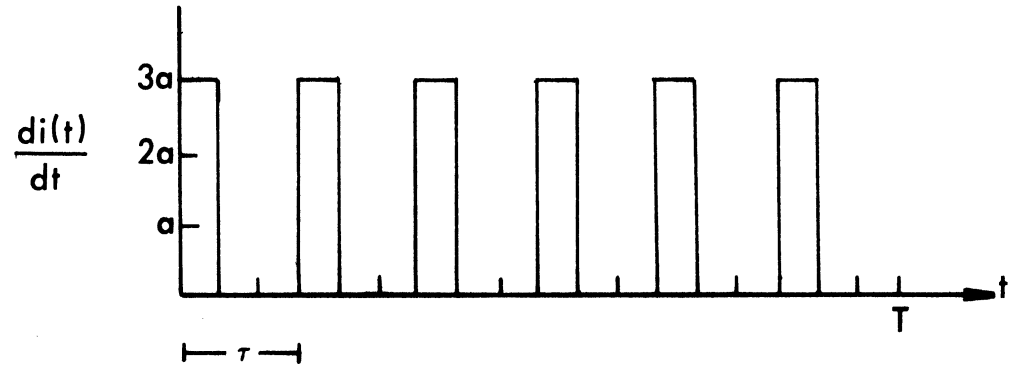

In the first diagram the beam intensity di(t)/dt is a constant with time t. In the second diagram the intensity comes in bursts, but the total area under this curve is the same as that under the first, so that from time t=0 to time

t=T the same number of particles will be counted in both cases. However, in the second case a detector counting the particles in the beam counts at times at three times the rate it does in the first case. Therefore, the total number of particles counted from t=0 to t=T,

$$N \equiv \int_0^T \frac{di(t)}{dt}\, dt \ ,$$

is not a good measure of the rate at which a detector counts during that interval. N in our case is proportional to TAS 100% singles.

Now consider the integral

$$M \equiv \int_0^T \left[\frac{di(t)}{dt}\right]^2 dt \ .$$

For the first diagram

$$R_1 \equiv (M/N) = (a^2T)/(aT) = a \ ;$$

whereas for the second diagram

$$R_2 \equiv (M/N) = (9a^2T/3)/(3aT/3) = 3a.$$

Thus the ratio

$$R = \int_0^T \left[\frac{di(t)}{dt}\right]^2 dt \ / \int_0^T \frac{di(t)}{dt}\, dt$$

gives a reasonable measure of the rate at which the detector must count.

By requiring the coincidence $TAS \cdot TAS_{delayed}$ we re-

quire the joint probability of a count at time t and one at time $t+\tau$, where τ is the delay time. Thus $TAS \cdot TAS_{delayed}$ measures the quantity

$$\int_0^T \frac{di(t)}{dt} \frac{di(t+\tau)}{dt} dt$$

during the period t=0 to t=T. To a very good approximation

$$\int_0^T \frac{di(t)}{dt} \frac{di(t+\tau)}{dt} dt = \int_0^T \left[\frac{di(t)}{dt}\right]^2 dt \ .$$

This relationship will hold exactly if the intensity varies randomly in the interval 0 to T, or if the intensity is periodic with period τ/(positive integer). The latter case is, of course, just that of the second diagram.

During our experiment the beam intensity was characterized by large peaks at intervals of 220 nanoseconds, the RF period of the AGS. There was other structure in the intensity with much longer periods--on the order of milliseconds--but the RF structure was predominant. We therefore used a delay time of 220 nanoseconds in forming the coincidence $TAS \cdot TAS_{delayed}$. Random structure in the beam intensity is, as noted above, detected regardless of the delay time chosen.

We now ask how the measured partial cross sections are affected by the neutron detector's counting at different rates during the target-in and target-out data collection periods. Let the number of neutrons counted by the detector during a target-out period be denoted by I'_{out},

and that during a target-in period by I'_{in}. In general, for reasons we mentioned in Chapter , these quantities will be functions of the rate; i.e., $I'_{out} = I'_{out}(R_{out})$ and $I'_{in} = I'_{in}(R_{in})$. Let us assume that we work at sufficiently low rates that we may expand in series of powers of R and keep only the first two terms; i.e.,

$$I'_{out} = I_{out}(1+\beta R_{out}) \tag{D.1}$$

and

$$I'_{in} = I_{in}(1+\beta R_{in}) \ ,$$

where the true partial cross section the counter measures as the rate approaches 0 is

$$\sigma_r \equiv \frac{1}{nx} \ln(I_{out}/I_{in}) \ ,$$

where for the sake of simplicity we have assumed that the number of monitor counts during out and in periods are the same. The measured partial cross section is, of course,

$$\sigma_m = \frac{1}{nx} \ln(I'_{out}/I'_{in})$$

$$\sigma_m = \frac{1}{nx} \ln\left\{[I_{out}/(1+\beta R_{out})]/[I_{in}/(1+\beta R_{in})]\right\}$$

$$\sigma_m = \sigma_r + \frac{1}{nx} \ln[(1+\beta R_{in})/(1+\beta R_{out})]$$

$$\sigma_m \approx \sigma_r + \frac{\beta}{nx}(R_{in}-R_{out})$$

$$\sigma_m \approx \sigma_r + \frac{\beta}{nx} R_{out}(R_{in}/R_{out}-1) \ . \tag{D.3}$$

If $I_{out} = \varkappa I_{in}$, then we should have

$$R_{out}/R_{in} = \left\{\int \varkappa^2\left[\frac{di(t)}{dt}\right]^2 dt \Big/ \int \varkappa \frac{di(t)}{dt}\, dt\right\}$$

$$\Big/\left\{\int\left[\frac{di(t)}{dt}\right]^2 dt \Big/ \int \frac{di(t)}{dt}\, dt\right\}$$

or

$$R_{out}/R_{in} = \varkappa = I_{out}/I_{in} ,$$

on the assumption that the structure in the intensity is the same during target-out and target-in periods. Then (D.3) becomes

$$\sigma_m \approx \sigma_r + \frac{\beta}{nx} R_{out}(I_{in}/I_{out}-1) ,$$

$$\sigma_m \approx \sigma_r + \frac{\beta}{nx} R_{out}[\exp(-nx\sigma_r)-1] ,$$

$$\sigma_m \approx \sigma_r + \frac{\beta}{nx} R_{out} \sum_{j=1}^{\infty}(-nx\sigma_r)^j/j! ,$$

$$\sigma_m \approx \sigma_r\left\{1-\beta R_{out}\left[1 - (nx\sigma_r)/2 + (nx\sigma_r)^2/6 - \ldots\right]\right\}.$$

For the targets we used, the sum in square brackets varied from 0.83 for our most attenuating target (lead) to 0.91 for our least attenuating target (hydrogen). Since the βR_{out} term was on the order of 0.01 to 0.02 for most of our running, we will ignore the expression inside the square brackets and write

$$\sigma_m \approx \sigma_r(1+\alpha R_{out}) ,$$

where the constant α is to be determined from the data by measuring σ_m at different rates.

APPENDIX E

BACKSCATTERING FROM THE TAS AND THE CONVERTER PLATE

The TAS constituted an enormous amount of material in in the beam immediately behind the transmission counters. One would expect that many of the particles formed in the neutron-originated showers in this material would be backward-going and pass through one or more of the transmission counters. Some such particles, in addition to ones similarly formed in the copper converter plate, would also pass through anti-counter A4. Thus some of the pulses from these counters would be spurious.

To give an idea of how the counting rates were affected by backscattering, we note that for the 28 GeV AGS energy running $D1 \cdot TAS\ 100\% / D1 \cdot \overline{A} \cdot TAS\ 100\% = 1.29$, $D1 \cdot D2 \cdot TAS\ 100\% / D1 \cdot D2 \cdot \overline{A} \cdot TAS\ 100\% = 1.41$, $D1 \cdot D2 \cdot D3 \cdot TAS\ 100\% / D1 \cdot D2 \cdot D3 \cdot \overline{A} \cdot TAS\ 100\% = 1.45$, and $D1 \cdot D2 \cdot D3 \cdot D4 \cdot TAS\ 100\% / D1 \cdot D2 \cdot D3 \cdot D4 \cdot A \cdot TAS\ 100\% = 1.50$. These data were taken with the vacuum pipe between the target area and the TAS still in place, so that practically all of the counts in A4 were from backscattering from the TAS or the converter plate. Further we note that when we moved the A4-converter plate-transmission counter assembly forward 0.6 meters from its previous position flush against the TAS the $D1 \cdot \overline{A} \cdot TAS\ 100\%$ counting rate decreased by 43%, the $D1 \cdot D2 \cdot \overline{A} \cdot TAS\ 100\%$ rate by 28%, the $D1 \cdot D2 \cdot D3 \cdot TAS\ 100\%$ rate by 23% and the $D1 \cdot D2 \cdot D3 \cdot D4 \cdot TAS\ 100\%$ rate by 21%. The

first set of data would suggest that the backscattered radiattion had a substantial soft component, which was easily stopped by a few of our 0.64 cm thicknesses of transmission counter scintillator. The latter set may suggest that the radiation was peaked near 180 degrees.

The question in which one is really interested, however, is how large an effect the backscattered radiation has on the total cross section inferred from the measured partial cross sections. Let us oversimplify the situation first by assuming that all the targets did was to attenuate the beam, so that we saw no scattered neutrons from the targets in our transmission counters. In this case, if we make the very reasonable assumption that the number of backscattered particles passing through a counter is proportional to the number of particles incident on the counter, we would expect the backscattering to have no effect on the partial cross section measured by a transmission counter. This result follows immediately from consideration of the all important ratio of target-out counts to target-in counts:

$$\frac{I'_{out}}{I'_{in}} = \frac{I_{out} + rI_{out} - sI_{out}}{I_{in} + rI_{in} - sI_{in}} = \frac{I_{out}}{I_{in}} , \qquad (E.1)$$

where I'_{out} is the number of target-out counts measured by a transmission counter, I'_{in} is the measured number of in counts, r the fraction of the incident intensity giving rise to backscttered particles from the TAS that trigger the

transmission counter, s is the fraction of the incident intensity giving rise to backscattered particles from the TAS or from the converter plate that trigger anti-counter A4, and I_{out} and I_{in} are respectively the actual number of target-out and target-in counts that the transmission counter should count. Then from the equality (E.1) we see immediately that the measured partial cross section is unaffected by backscattering.

In the real situation we must take into account the angular distribution of neutrons scattered from the target. Of course, as we explained in Chapter IV, it is exactly this distribution which we seek to determine by using the several transmission counters so that we can infer the total cross section from the D4 partial cross section. Thus, the question of how the inferred total cross section is affected by backscattering is for us really two questions. First, how is the D4 partial cross section affected by backscattering? And second, what is the effect of backscattering on the measured angular distribution of neutrons scattered by the target? Rather than following a convoluted computational course here, we have taken a strictly empirical one.

The answer to the first of the two questions we have just asked turns out to be that to within statistics we found no effect on the D4 partial cross section. For example, for lead in the 100% TAS channel during the 28 GeV AGS energy running, we found the D4 partial cross section to be 3044 ± 20 mb when the vacuum pipe was up, the trans-

mission counters were flush against the TAS and A4 was turned off. Under the same conditions but with A4 in operation, this number was 3063 ± 14 mb. With the vacuum pipe taken down, A4 in operation and the transmission counters moved forward 0.6 meters from the TAS, this cross section was 3050 ± 26 mb. For copper the three measurements were 1237 ± 17 mb, 1243 ± 6 mb, and 1253 ± 13 mb respectively. For aluminum we measured 639 ± 20, 649 ± 6 mb, and 653 ± 7 mb.

The answer to the second question is that we did see some dependence of the angular distribution of scattered neutrons on backscattering, but that the resulting effect on the inferred total cross section was not large. We most clearly saw a statistically significant dependence for the heaviest targets, as one would expect. For example, for lead in the same three situations mentioned above, the differences between the D4 and D2 partial cross sections were 272 ± 10 mb, 335 ± 8 mb, and 286 ± 6 mb respectively. The differences between the D2 and D1 partial cross sections were 441 ± 14 mb, 367 ± 6 mb, and 316 ± 6 mb respectively. In the three cases these results imply that 37 ± 2 mb, 53 ± 2 mb, or 45 ± 2 mb must be added to the D4 partial cross section to obtain the total cross section. Using the differential cross sections measured by Bellettini et al.,[34] one would expect to have to add 29 mb. Clearly then in this case, if we make no prejudgements about which of our measurements should be most nearly correct or whether we should expect to agree with the result derived from the Bellettini

data, we have a full spread in the amount to be added to the D4 partial cross section of about 0.8%. We have presented the worst case here. As one goes to lighter elements and lower neutron energies the fractional uncertainty in the total cross sections from backscattering decreases. That this result should be so follows simply from the fact that the transmission counters collect fewer scattered particles with decreasing atomic mass and energy. Estimates of the uncertainties due to backscattering for our data at an AGS energy of 28 GeV are given in the final table of Chapter IV.

APPENDIX F

CORRECTING THE BELLETTINI DATA FOR COULOMB-NUCLEAR INTERFERENCE

The proton-nucleus total cross sections published by Bellettini et al.[34] were obtained from a measurement of one partial cross section plus extensive measurements of the differential elastic scattering cross section. Their data were analyzed on the assumption that the real part of the nuclear scattering amplitude was zero for heavy elements--beryllium and heavier--although they note their data could have been consistent with a real part of between about 5% to 10%. Admittedly one expects that as one goes to heavier nuclei the real part of the scattering amplitude should decrease in magnitude relative to the imaginary part. For a totally absorbing nucleus the real part must be exactly zero, as is easily seen by considering the ususal partial wave expansion of the scattering amplitude. However, even lead is not a completely black nucleus, so we should expect some real part for the scattering amplitudes for physical nuclei. We will talk about how we obtain these real parts a little further on. Right now we will discuss the method of correcting Bellettini's data with the assumption that we know the real parts.

The net differential cross section observed in the experiment is

$$\frac{d\sigma}{d\Omega} = |f_n(\theta)+f_C(\theta)|^2$$

$$\frac{d\sigma}{d\Omega} = |f_N(\theta)|^2 + |f_C(\theta)|^2 + 2\Big\{\mathrm{Im}[f_N(\theta)]\mathrm{Im}[f_C(\theta)] + \\ + \mathrm{Re}[f_N(\theta)]\mathrm{Re}[f_C(\theta)]\Big\}, \qquad (F.1)$$

where $f_N(\theta)$ is the nuclear elastic scattering amplitude and $f_C(\theta)$ is the Coulomb scattering amplitude for scattering at an angle θ. The Coulomb amplitude for proton scattering--ignoring magnetic moment scattering--from a nucleus of atomic number Z and atomic mass A is[67]

$$f_C(\theta) \approx e^{2i\eta(\theta)}(-2\alpha Z)(\beta p\theta^2)^{-1}F_1(|t|)F_C(A,|t|), \qquad (F.2)$$

where α is the fine structure constant, β is the velocity, p is the momentum, $F_1(|t|)$ is the proton form factor, $F_C(A,|t|)$ is the Coulomb form factor of the nucleus (see Appendix C), and $\eta(\theta)$ is the Coulomb phase shift. The nuclear scattering amplitude is

$$f_N(\theta) = (4\pi)^{-1}\sigma_T pF_N(A,|t|)[i+\rho(\theta)]e^{2i\zeta(\theta)}, \qquad (F.3)$$

where σ_T is the total cross section, $F_N(A,|t|)$ is the form factor for nuclear scattering by the nucleus, $\rho(\theta) \equiv \mathrm{Re}[f_N(\theta)e^{-2i\zeta(\theta)}]/\mathrm{Im}[f_N(\theta)e^{-2i\zeta(\theta)}]$ and $\zeta(\theta)$ is the Coulomb phase shift for nuclear scattering.[67] Clearly, only the difference $[\eta(\theta)-\zeta(\theta)] \equiv \delta(\theta)$ is important rather than either $\eta(\theta)$ or $\zeta(\theta)$ alone. The expression for $\delta(\theta)$ is given in reference 67 as

$$\delta(\theta) \approx \frac{Z\alpha}{\beta} \ln[1.060p^{-1}\langle R_C^2\rangle^{-\frac{1}{2}}\theta^{-1}], \qquad (F.4)$$

where $\langle R_C^2\rangle^{\frac{1}{2}}$ is the rms Coulomb radius of the nucleus. (See Appendix C for a table of $\langle R_C^2\rangle^{\frac{1}{2}}$.) (The derivation given in reference 67 for $\delta(\theta)$ seems unsatisfactory for high energies and large nuclei. The author of that reference tells us that $\delta(\theta)$ is to be set to zero beyond some angle, but does not specify how to determine what the angle is. We will present results obtained using $\delta(\theta) = 0$ and $\delta(\theta)$ as given by equation (F.4).)

A partial cross section, σ_P, will be related to the total cross section, σ_T, by

$$\sigma_P = \sigma_T - 2\pi\int_0^{\theta_o} |f_N(\theta)|^2 \sin(\theta)d\theta + 2\pi\int_{\theta_o}^{\pi} |f_C(\theta)|^2 \sin(\theta)d\theta$$

$$+ 4\pi\int_{\theta_o}^{\pi} \mathrm{Im}[f_N(\theta)]\left\{\rho(\theta)\mathrm{Re}[f_C(\theta)]+\mathrm{Im}[f_C(\theta)]\right\}\sin(\theta)d\theta, \qquad (F.5)$$

where θ_o is the angle that the perimeter of the transmission counter makes with the center of the target--1.5 milliradians in this case[34]--and where we have ignored complications introduced by a nonzero radius beam spot at the transmission counter. We do not have the partial cross sections of Bellettini et al. However, we do have their total cross sections and their angular distributions.[68] Since these authors ignored Coulomb-nuclear interference--including interference via the Coulomb phase shift difference

$\delta(\theta)$--they ignored the third term in (F.1) and the third integral in (F.5), so we can write

$$\sigma_T = \sigma_T' - \Delta_1 + \Delta_2 \ , \qquad \text{(F.6)}$$

where σ_T' is the total cross section reported by Bellettini et al., and

$$\Delta_1 = 4\pi\int_{\theta_o}^{\pi} \mathrm{Im}[f_N(\theta)]\left\{\rho(\theta)\mathrm{Re}[f_C(\theta)] + \mathrm{Im}[f_C(\theta)]\right\}\sin(\theta)d\theta$$

$$\Delta_2 = 2\pi\int_0^{\theta_o}\left\{|f_N(\theta)|^2 - |f_N'(\theta)|^2\right\}\sin(\theta)d\theta \ ,$$

where $|f_N'(\theta)|^2$ is the differential cross section for nuclear scattering obtained by Bellettini et al. in their analysis. Parametrizing the form factors as

$$F_N(A,|t|) \approx J_1(R_N|t|^{\frac{1}{2}})/(R_N|t|^{\frac{1}{2}}/2), \qquad \text{(F.7)}$$

$$\approx \exp(-R_N^2|t|/8), \ R_N|t|^{\frac{1}{2}} << 1 \qquad \text{(F.8)}$$

$$F_C(A,|t|) \approx \exp(-\langle R_C^2\rangle|t|/6), \qquad \text{(F.9)}$$

$$F_1(|t|) \approx \exp(-0.64\mathrm{fm}^2|t|/6), \qquad \text{(F.10)}$$

(see Appendix C) where J_1 is the first order Bessel function of the first kind and R_N is the equivalent uniform density radius of the nucleus, we find after a little algebra that

$$\Delta_1 \approx -2\sigma_T\alpha Z\beta^{-1}\int_{\theta_o}^{\pi}\left\{\left[\rho(\theta)\cos[2\delta(\theta)] + \sin[2\delta(\theta)]\right]\right.$$

$$\times \exp\left[-[R_N^2/8 + (\langle R_C^2\rangle + 0.64\text{fm}^2)/6]p^2\theta^2\right]\Big\}\frac{d\theta}{\theta} \tag{F.11}$$

and

$$\Delta_2 \approx (16\pi)^{-1}p^2[\sigma_T^2 - (\sigma_T')^2]\theta_o^2, \tag{F.12}$$

where we have used small angle expansions for functions of θ. We used (F.1) to determine R_N for each element for use in (F.11) and then solved (F.6) for σ_T.

The real parts of the nuclear elastic scattering amplitudes were calculated from the Glauber model. Carrying equation (II.1) through the same steps that lead to equation (II.10), we find the elastic scattering amplitude to be given by

$$F_{ii}(q') = ip\int_0^\infty J_0(q'b)\Big\{1-\Big[1-(1-i\alpha)(4\pi)^{-1}\sigma_N\int_0^\infty J_0(qb)$$

$$\times\ S(q)\exp(-\tfrac{1}{2}\beta q^2)qdq\Big]^A\Big\}bdb\ , \tag{F.13}$$

where the notation is the same as in equation (II.10). The Woods-Saxon nuclear density model was used to calculate $S(q)$ with parameters taken from Table 1. (The "Strong Interaction" set were used.) In Table F.1 we show $\rho(\theta=0)$ for five elements at the momenta at which the Bellettini <u>et al</u>. total cross sections were measured. As we expected, $\rho(0)$ decreases with increasing A. However, in equations (F.1) and (F.11) we need $\rho(\theta)$ over a range of θ values, not

just at 0. $\rho(\theta)$ turns out to exhibit a strong angular dependence for the heaviest elements. For example, we list in Table F.2 some values of $\rho(\theta)$ for beryllium and lead over the θ range that contributed ~99.9% of the value of the integral in (F.11) for each of these elements.

TABLE F.1

THE RATIO OF THE REAL PART OF THE ELASTIC NUCLEAR SCATTERING AMPLITUDE TO THE IMAGINARY PART AT ZERO DEGREES AS A FUNCTION OF ATOMIC MASS NUMBER

Element	A	Momentum (GeV/c)	$\alpha^{\dagger}$	$\rho(0)$
Be	9	19.3	-0.210	-0.167
C	12	21.5	-0.187	-0.141
Al	27	19.3	-0.210	-0.132
Cu	64	19.3	-0.210	-0.104
Pb	207	19.3	-0.210	-0.069

$^{\dagger}\alpha = \mathrm{Re}[f_{NN}(0)]/\mathrm{Im}[f_{NN}(0)]$ obtained from reference 18.

We list in Table F.3 the values of σ_T', the total cross sections uncorrected for Coulomb-nuclear interference reported by Bellettini et al., and the corrected total cross sections, σ_T, which we have determined. We have maintained the published error in the latter case. As we mentioned earlier, we present σ_T calculated using $\delta(\theta) = 0$ and $\delta(\theta)$ as given by equation (F.4). A really large discrepancy between these two values of σ_T shows up only in lead. The lower

TABLE F.2

$\rho(\theta)$ FOR BE AND PB OVER SELECTED ANGULAR RANGES
PROTON MOMENTUM = 19.3 GEV/c

Beryllium		Lead	
θ (mr)	$\rho(\theta)$	θ (mr)	$\rho(\theta)$
0.00	-0.167	0.00	-0.069
4.11	-0.162	1.90	-0.059
5.81	-0.156	2.68	-0.047
7.12	-0.149	3.29	-0.032
8.22	-0.141	3.79	-0.011
9.19	-0.131	4.24	+0.021
10.06	-0.119	4.64	+0.079
10.87	-0.103	5.02	+0.225
11.63	-0.084	5.37	+1.551
12.33	-0.075	5.69	-0.598
13.00	-0.017	6.00	-0.300

value, obtained by using $\delta(\theta)$ from equation (F.4), seems unreasonable, in view of the fact that for the lighter elements the proton-nucleus total cross sections are practically equal to the neutron-nucleus cross sections. We will arbitrarily assume therefore that the calculations using $\delta(\theta) = 0$ are more nearly correct. Clearly though the proton-lead total cross section is not very certain.

TABLE F.3

CORRECTED AND UNCORRECTED VALUES OF THE TOTAL CROSS SECTIONS OF BELLETTINI ET AL. FOR PROTONS ON NUCLEI

Element	Momentum (GeV/c)	σ_T' (mb)	σ_T (mb)	
			$\delta(\theta)=0$	$\delta(\theta)$ Via (F.4)
Be	19.3	278 ± 4	275	275
C	21.5	335 ± 5	331	331
Al	19.3	687 ± 10	671	676
Cu	19.3	1360 ± 20	1320	1339
Pb	19.3	3290 ± 100	3184	2788

APPENDIX G

REMARKS ON THE MODEL OF PUMPLIN AND ROSS

In this appendix we show that the model of Pumplin and Ross, the content of which is given by equation(II.25), can be derived from equations (II.21). We first rewrite (II.21) here for convenience:

$$\frac{d}{dz}\varphi_\alpha(\vec{b},z) = \frac{1}{2ip_\alpha}\sum_\beta U_{\alpha\beta}(\vec{r})\exp[i(p_\beta-p_\alpha)z]\varphi_\beta(\vec{b},z). \tag{G.1}$$

We recall that $\alpha=1$ denotes the incident particle.

Let us ignore the couplings of the resonances to each other and assume that they couple only to the incident particles. Then for either $\alpha\neq1$ or $\beta\neq1$, $U_{\alpha\beta}=0$ for $\alpha\neq\beta$. We then propose as a solution to (G.1) for $\alpha\neq1$ the expression

$$\varphi_{\alpha\neq1}(\vec{b},z) = \varphi_1(\vec{b},z)(2ip_\alpha)^{-1}\int_{-\infty}^{z}\exp[i(p_\alpha-p_1)z']U_{\alpha1}(b,z')dz'. \tag{G.2}$$

Differentiating (G.2) with respect to z we obtain

$$\frac{d}{dz}\varphi_{\alpha\neq1}(\vec{b},z) = (2ip_\alpha)^{-1}\Big\{\exp[i(p_\alpha-p_1)z]U_{\alpha1}(\vec{b},z)\varphi_1(\vec{b},z) + \frac{d}{dz}\varphi_1(\vec{b},z)\int_{-\infty}^{z}\exp[i(p_\alpha-p_1)z']U_{\alpha1}(\vec{b},z')dz'. \tag{G.3}$$

We thus see that (G.3) is just equation (G.1) for $\alpha\neq1$ if

$$\frac{d}{dz}\varphi_1(\vec{b},z) = \frac{1}{2ip_\alpha} U_{\alpha\alpha}(\vec{b},z)\varphi_1(\vec{b},z). \qquad (G.4)$$

Then (G.2) is indeed a solution of (G.1) for $\alpha \neq 1$. We see that (G.4) is approximately equation (G.1) if we may assume that: 1) $U_{\alpha\alpha} \approx U_{11}$, i.e., the amplitude for elastic scattering of the resonance α is the same as that for the incident particle; 2) $p_\alpha \approx p_1$--which is true for p_1 large and the mass, m_α, not too different from the mass, m_1, of the incident particle (see equation (II.18)); and 3) the coupling terms in (G.1) are small. With these assumptions, using (G.2) in (G.1), we obtain

$$\frac{d}{dz}\ln[\varphi_1(\vec{b},z)] = \frac{1}{2ip_1}\sum_{\beta\neq 1}\Big\{U_{1\beta}(\vec{b},z)\exp[i(p_\beta-p_1)z](2ip_\beta)^{-1}$$

$$\times \int_{-\infty}^{z}\Big[\exp[i(p_1-p_\beta)z']U_{\beta 1}(\vec{b},z')\Big]dz'\Big\}$$

$$+ \frac{1}{2ip_1} U_{11}(\vec{b},z). \qquad (G.5)$$

This equation is integrated to give

$$\varphi_1(\vec{b},z) = \exp\Big\{\frac{1}{2ip_1}\int_{-\infty}^{z} U_{11}(\vec{b},z')dz' + \frac{1}{2ip_1}\int_{-\infty}^{z}\sum_\beta \frac{1}{2ip_\beta}$$

$$\times\ U_{1\beta}(\vec{b},z')\exp[i(p_1-p_\beta)z']\int_{-\infty}^{z'}\exp[i(p_1-p_\beta)z'']$$

$$\times\ U_{\beta 1}(\vec{b},z'')dz''dz' \qquad (G.6)$$

Now the amplitude at momentum transfer $\vec{q}$ for outgoing par-

ticle 1 is[43]

$$f_1(q) = \frac{-1}{4\pi} \int \exp[+i(\vec{q}\cdot\vec{r})\Big[\sum_\beta U_{1\beta}(\vec{b},z)\exp[i(p_\beta - p_1)z]$$

$$\times\ \varphi_\beta(\vec{b},z)\Big]d^3r. \qquad (G.7)$$

Using (G.2) and the optical theorem gives

$$\sigma_T = \frac{-1}{p_1} \mathrm{Im}\Big\{\int \varphi_1(\vec{b},z)\Big[U_{11}(\vec{b},z) + \Big(\sum_{\beta\neq 1}(2ip_\beta)^{-1}U_{1\beta}(\vec{b},z)$$

$$\times\ \exp[i(p_\beta - p_1)z]\int_{-\infty}^{z} \exp[i(p_1 - p_\beta)z']$$

$$\times\ U_{\beta 1}(\vec{b},z')dz'\Big)\Big]d^3r\Big\}, \qquad (G.9)$$

where $\varphi_1(\vec{b},z)$ is given by (G.6). Had we ignored the couplings to the resonances altogether, we obviously would have gotten for the total cross section

$$\sigma_T^\circ = \frac{-1}{p_1} \mathrm{Im}[\int \varphi_1^\circ(\vec{b},z)U_{11}(\vec{b},z)d^3r] \qquad (G.10)$$

where

$$\varphi_1^\circ(\vec{b},z) = \exp\Big\{\frac{1}{2ip_1}\int_{-\infty}^{z} U_{11}(\vec{b},z')dz'\Big\}. \qquad (G.11)$$

$\Delta\sigma_{regn} \equiv \sigma_T^\circ - \sigma_T$ is therefore the change in the total cross section due to regeneration of the incident particle from the intermediate inelastic states. If, as above, we assume that the coupling terms in (G.6) are small, we may take $\varphi_1(\vec{b},z) \approx \varphi_1^\circ(\vec{b},z)$, so that from (G.9) and (G.10) we get

$$\Delta\sigma_{regn} \approx \frac{+1}{p_1} \mathrm{Im}\Big\{\int \overset{\circ}{\varphi}_1(\vec{b},z)\Big[\sum_{\beta\neq 1}\Big((2ip_\beta)^{-1}U_{1\beta}(\vec{b},z)\exp[i(p_\beta-p_1)z]$$

$$\times \int_{-\infty}^{z} \exp[i(p_1-p_\beta)z']U_{\beta 1}(\vec{b},z')dz'\Big)\Big]d^3r\Big\} \qquad (G.12)$$

For the potentials we use expression (II.20):

$$U_{\alpha\beta}(\vec{r}) = -4\pi A\rho(r)f_{\alpha\beta}(0), \qquad (G.13)$$

and assume a uniform density

$$\rho(r) = (4\pi R^3/3)^{-1}\theta(R-r), \qquad (G.14)$$

where R is the radius of the nucleus with mass number A, $r = |\vec{r}|$, and $\theta(R-r)$ is the theta function $\theta(R-r) = 1$ for $R > r$ and $\theta(R-r) = 0$ for $R < r$. Then (G.11) becomes

$$\varphi_1^{\circ}(\vec{b},z) = \exp\Big\{-3(2ip_1R^3)^{-1}f_{11}(0)\Big[(R^2-b^2)^{\frac{1}{2}}[1+\theta(r-R)]$$

$$+z\theta(R-r)\Big]\Big\}. \qquad (G.15)$$

Using this last equation in (G.12) we get

$$\Delta\sigma_{regn} \approx -(9/2)A^2R^{-6}p_1^{-1}\mathrm{Im}\Big\{\sum_{\beta\neq 1} ip_\beta^{-1}f_{1\beta}(0)f_{\beta 1}(0)\int d^3r\int_{-\infty}^{z} dz'$$

$$\times \Big[\theta(R-r)\theta(R-r')\exp\Big(-i[\Delta_{1\beta}(z-z')]-\lambda D(b,z)/2\Big)\Big]\Big\}$$

$$(G.16)$$

where $\vec{r}' = \vec{b}' + \vec{z}'$, $\lambda = -3iAf_{11}(0)(p_1R^3)^{-1}$, and $D(b,z) = z + (R^2-b^2)^{\frac{1}{2}}$. $\Delta_{1\beta} = p_1-p_\beta$ is given by (II.18). The integrations are easily done and yield

$$\Delta\sigma_{regn} = -18\pi A^2 R^{-6} p_1^{-1} \mathrm{Im}\Big\{ \sum_{\beta\neq 1} (p_\beta \Delta_{\beta 1})^{-1} f_{\beta 1}(0) f_{1\beta}(0)$$

$$\times\ [\zeta(\lambda)-\zeta(\lambda+2i\Delta_{1\beta})]\Big\}\ , \qquad (G.17)$$

where $\zeta(a) \equiv [(1+aR)e^{-aR}-1+\frac{1}{2}a^2R^2]a^{-3}$. Then we see that for predominantly positive imaginary amplitudes $f_{\beta 1}(0)f_{1\beta}(0)$ is predominantly real and negative. λ is then also predominantly positive real, so that $[\zeta(\lambda)-\zeta(\lambda+2i\Delta_{1\beta})] \approx 2i\Delta_{1\beta}(d\zeta/d\lambda)|_{\lambda+2i\Delta_{1\beta}}$ is mostly negative imaginary, since for real λ, $d\zeta/d\lambda$ is less than zero. Thus, in this case, $\Delta\sigma_{regn} = \sigma_T^o - \sigma_T$ is positive, and the total cross section is decreased by the regenerative effects.

From (II.1)

$$f_{\beta 1}(0) = (i+\eta_{\beta 1})(1+\eta_{\beta 1}^2)^{-\frac{1}{2}} p_\beta \pi^{-\frac{1}{2}} \{d\sigma_{\beta 1}/d|t|)|_{t=0}\}^{\frac{1}{2}}, \qquad (G.18)$$

$$f_{1\beta}(0) = (i+\eta_{1\beta})(1+\eta_{1\beta}^2)^{-\frac{1}{2}} p_\beta \pi^{-\frac{1}{2}} \{d\sigma_{1\beta}/d|t|)|_{t=0}\}^{\frac{1}{2}} \qquad (G.19)$$

where $\eta_{\alpha\beta} \equiv \mathrm{Re}[f_{\alpha\beta}(0)]/\mathrm{Im}[f_{\beta\alpha}(0)]$. Let us ignore complications introduced by spins so we may take $f_{1\beta}(0) = f_{\beta 1}(0)$. We define $\eta_\beta \equiv \eta_{1\beta} = \eta_{\beta 1}$. Then using $(i+\eta_\beta)^2/(1+\eta_\beta^2) = -(1-i\eta_\beta)/(1+i\eta_\beta)$, we get from (G.17)

$$\Delta\sigma_{regn} = +\sum_\beta (d\sigma_{1\beta}/d|t|)_0 F_\beta(p) \qquad (G.20)$$

where

$$F_\beta(p) = 18A^2R^{-6}\Delta_{\beta 1}^{-1}\mathrm{Im}\{[\zeta(\lambda)-\zeta(\lambda+2i\Delta_{1\beta})](1-i\eta_\beta)(1+i\eta_\beta)^{-1}\}, \tag{G.21}$$

and $(d\sigma_{1\beta}/d|t|)_0 \equiv (d\sigma/d|t|)_{t=0}$. To get Pumplin and Ross's result quoted in Chapter II as equation (II.25), we let

$$\sum_{\beta\neq 1} \rightarrow \int dm_{N\pi} ,$$

$$(d\sigma_{1\beta}/d|t|)_0 \rightarrow (d^2\sigma/d|t|dm_{N\pi})_0 ,$$

and make the obvious change in notation

$$F_\beta(p) \rightarrow F(p,m_{N\pi}).$$

Since (G.20) is only an approximate solution for $\Delta\sigma_{regn}$, we tested it by solving the set of differential equations (G.1) numerically for σ_T and σ_T^o to get $-\sigma_{inel}$. Since we are coupling only the discrete resonances to the incident neutron, this latter calculation is that of the Bochmann and Margolis model. Identical input was used in both cases, except that the more realistic Woods-Saxon density was used in solving the differential equations. For listings of the values of $f_{\alpha\alpha}(0)$ and $f_{\alpha 1}(0)$ and the phases used, see Section C of Chapter V.) The calculations were done for p_1 = 15 GeV/c and p_1 = 30 GeV/c. The results are listed for beryllium and lead in Table G.1. The box headings "Via Equations (II.21)" and "Via Equations (G.20)" mean that equations (II.21) and (G.20) were used respectively to obtain the listed results. Clearly these results

show that (G.20) is a very poor approximate solution to the differential equations.

TABLE G.1

COMPARISON OF APPROXIMATE AND EXACT SOLUTIONS FOR $\Delta\sigma_{regn}$ FOR THE DISCRETE RESONANCE CASE

Element	$\Delta\sigma_{regn}$ (mb)			
	Via Equations (II.21)		Via Equation (G.2)	
	p_1=15 GeV/c	p_1=30 GeV/c	p_1=15 GeV/c	p_1=30 GeV/c
Be	+3.0±0.4	+6.5± 2.4	+6.9± 0.9	+12.0± 4.5
Pb	+43 ±8	+101 ±48	+140 ±20	+285 ±100

The results above indicate that when we go over to the case of including the entire cross section $(d^2\sigma/d|t|dm_{N\pi})_0$ and not just the resonant part, we should expect that equation (II.25) will overestimate $\Delta\sigma_{regn}$. We show in Table (G.2) $\Delta\sigma_{regn}$ calculated from (II.25) and by the method we have described in Section D of Chapter II, the latter under the box heading "Via Equations (II.21)". $(d^2\sigma/d|t|dm_{N\pi})_0$ was obtained from Figures 2 and 3 and all the phases were taken equal to the phase for pp→pp. Again we see the large differences in the results yielded by the two methods.

It is apparent from Tables (G.1) and (G.2) that equation(II.25), which was used by Pumplin and Ross in their original numerical calculations, greatly overestimates the effect of regeneration.

TABLE G.2

COMPARISON OF $\Delta\sigma_{regn}$ CALCULATED BY TWO METHODS FOR THE CASE OF INCLUDING THE ENTIRE CROSS SECTION $(d^2\sigma/d|t|dm_{N\pi})_0$

Element	$\Delta\sigma_{regn}$ (mb)			
	Via Equations (II.21)		Via Equation (II.25)	
	p_1=15 GeV/c	p_1=30 GeV/c	p_1=15 GeV/c	p_1=30 GeV/c
Be	+9	+15	+31	+41
Pb	+123	+180	+530	+745

APPENDIX H

THE RELATIVE MAGNITUDES OF ELASTIC AND INELASTIC DIFFERENTIAL CROSS SECTIONS AT SMALL ANGLES

Since the TAS does not provide perfect energy resolution, the transmission counters collect not only elastically scattered neutrons but also some inelastically scattered ones as well. However, it turns out that at the small values of $|t|$ seen by our transmission counters, it is unnecessary to consider explicitly inelastic scattering when we remove the D4 partial cross section defect. We can easily show this fact by considering the ratio of $(d\sigma/d\Omega)_{el}$ to $(d\sigma/d\Omega)_{inel}$, where the subscripts "el" and "inel" mean elastic and inelastic respectively. $(d\sigma/d\Omega)_{el}$ is given by equation (IV.6). To get $(d\sigma/d\Omega)_{inel}$ we note from equation (IV.1) that the change in the total cross section, $(\Delta\sigma)_{inel}$, caused by a counter's collecting a number of inelastically scattered neutrons, $(\Delta I)_{inel}$, is

$$(\Delta\sigma)_{inel} = \frac{1}{nx}\left\{\ell n[I_{out}/I_{in}] - \ell n[I_{out}/(I_{in}+(\Delta I)_{inel})]\right\}$$

$$(\Delta\sigma)_{inel} \approx \frac{1}{nx}(\Delta I)_{inel}/I_{in}.$$

The change per small solid angle, $\Delta\Omega$, is

$$(\Delta\sigma/\Delta\Omega)_{inel} \approx (nxI_{in})^{-1}(\Delta I/\Delta\Omega)_{inel}.$$

We define $(\Delta I'/\Delta\Omega)_{inel}$ to be $(\Delta I/\Delta\Omega)_{inel}/I_{int}$, where I_{int} is the number of particles interacting inelastically with

the target. Then

$$(\Delta\sigma/\Delta\Omega)_{inel} \approx \frac{1}{nx}(\Delta I'/\Delta\Omega)_{inel}(I_{int}/I_{in}).$$

Now

$$I_{int} = I_{out} - I_{out}\exp(-nx\sigma_{inel}) \approx nx\sigma_{inel}I_{out},$$

where σ_{inel} is the total inelastic (or absorption) cross section for the target. Thus,

$$(\Delta\sigma/\Delta\Omega)_{inel} \approx \sigma_{inel}(I_{out}/I_{in})(\Delta I'/\Delta\Omega)_{inel}.$$

Then

$$(\Delta\sigma/\Delta\Omega)_{el}/(\Delta\sigma/\Delta\Omega)_{inel} \approx (\sigma_T p/4\pi)^2\exp(-R^2p^2\theta^2/4)[\sigma_{inel} \times (I_{out}/I_{in})(\Delta I'/\Delta\Omega)_{inel}]^{-1}.$$

$(\Delta I'/\Delta\Omega)_{inel}$ can be estimated from theoretical secondary particle spectra published by Grote, Hagedorn and Ranft.(3) These authors give plots of $(d^2I'/dpd\Omega)$. Integrating their plots over p we can find $(dI'/d\Omega)$. For example we find at 19.2 GeV/c that

$$\frac{dI'}{d\Omega} \approx \frac{150 \text{ secondary neutrons}}{\text{sr}\cdot\text{interacting neutron}}$$

at $\theta=0$ for lead and about the same for beryllium. Let us make the assumption that our energy resolution is so poor that we count all the secondaries. Further, since $dI'/d\Omega$ does not decrease so rapidly with θ as $(d\sigma/d\Omega)_{el}$, we will

take $dI'/d\Omega$ to be constant. Then roughly at 19.2 GeV/c

$$(\Delta\sigma/\Delta\Omega)_{el}/(\Delta\sigma/\Delta\Omega)_{inel} \approx (\sigma_T p/4\pi)^2 \exp(-R^2 p^2 \theta^2/4)[150 \times (I_{out}/I_{in})\sigma_{inel}]^{-1} \qquad (H.1)$$

For our beryllium target $(I_{out}/I_{in}) \approx 1.3$. For our lead target this number is ~ 1.4. For beryllium $\sigma_{inel} \approx 0.85\sigma_T$, and for lead $\sigma_{inel} \approx 0.55\sigma_T$.[34] Then using the values of R given by Bellettini <u>et al</u>.,[34] we find at zero degrees

$$(\Delta\sigma/\Delta\Omega)_{el}/(\Delta\sigma/\Delta\Omega)_{inel} \approx 160 \text{ for Pb,}$$

$$\approx 9.5 \text{ for Be.}$$

Interestingly, the Hagedorn plots show that $dI'/d\Omega$ at 0° scales with momentum as p^2 to a very good approximation. Then the only momentum dependence in (H.1) is in the exponential. The ratio $(\Delta\sigma/\Delta\Omega)_{el}/(\Delta\sigma/\Delta\Omega)_{inel}$ will be smallest at our largest momentum. We find that for the largest value of $|t|$ seen by our transmission counters

$$(d\sigma/d\Omega)_{el}/(d\sigma/d\Omega)_{inel} \approx 80 \text{ for Pb,}$$

$$8.5 \text{ for Be.}$$

Then, even for beryllium, taking $d\sigma/d\Omega$ in (IV.3) equal to $(d\sigma/d\Omega)_{el}$ is not a bad approximation. For hydrogen and deuterium, for which this approximation would be poor, we had no measureable defect in the D4 partial cross section, so we need not worry about these light elements.

REFERENCES

1. L. W. Jones, M. J. Longo, J. R. O'Fallon and M. N. Kreisler, Phys. Letters 27B, 328 (1968).
2. M. N. Kreisler, L. W. Jones, M. J. Longo and J. R. O'Fallon, Phys. Rev. Letters 20, 468 (1968)
3. H. Grote, R. Hagedorn and J. Ranft, Atlas of Particle Production Spectra (Cern, Geneva, 1970).
4. W. L. Lakin, E. B. Hughes, L. H. O'Neill, N. J. Otis and L. Mandansky, Phys. Letters 31B, 677 (1970).
5. R. E. Mischke, T. J. Devlin, W. Johnson, J. Norem, K. Vosburgh and W. Schimmerling, Phys. Rev. Letters 25, 1724 (1970).
6. T. Coor, D. A. Hill, W. F. Hornyak, L. W. Smith and G. Snow, Phys. Rev. 98, 1369 (1955).
7. V. P. Dzhelepov, V. I. Satarov and B. M. Golovin, JETP 2, 349 (1956), J. Exper. Theoret. Phys. USSR 29, 369 (1955) .
8. A. Ashmore, R. G. Jarvis, D. S. Mather and S. K. Sen, Proc. Phys. Soc. (London) A70, 745 (1957).
9. V. S. Pantuev, M. N. Khachaturyan, I. V. Chuvilo, JNP 1, 93, (1965), J. Nucl. Physics USSR 1, 134 (1965) .
10. L. W. Jones, Technical Report No. 32, Dept. of Physics of The University of Michigan, Ann Arbor, Michigan (1968).
11. J. Engler, K. Horn, J. Koenig, F. Moennig, P. Schluedecker, H. Schopper, P. Sievers, H. Ullrich and K. Runge, Phys. Letters 28B,64 (1969).
12. J. Engler, K. Horn, J. Koenig, F. Moennig, P. Schluedecker, H. Schopper, P. Sievers, H. Ullrich and K. Runge, Phys. Letters 27B, 599 (1968).
13. J. Engler, K. Horn, F. Moennig, P. Schludecker, W. Schmidt-Parzefall, H. Schopper, P. Sievers, H. Ullrich, R. Hartung, K. Runge and Yu. Galaktionov, Phys. Letters 31B, 669 (1970).

14. J. Engler, K. Horn, F. Moennig, P. Schludecker, W. Schmidt-Parzefall, H. Schopper, P. Sievers, H. Ullrich, R. Hartung, K. Runge, Yu. Galaktionov, Phys. Letters 32B, 716 (1970).
15. E. F. Parker, H. R. Gustafson, L. W. Jones, M. J. Longo, P. V. Ramana Murthy, F. E. Ringia and B. Cork, Phys. Letters 31B, 246 (1970).
16. E. F. Parker, T. Dobrowolski, H. R. Gustafson, L. W. Jones, M. J. Longo, F. Ringia and B. Cork, Phys. Letters 31B, 250 (1970).
17. D. V. Bugg, D. C. Salter, G. H. Stafford, R. F. George, K. F. Riley and R. J. Tapper, Phys. Rev. 146, 980 (1966).
18. K. J. Foley, R. S. Jones, S. J. Lindenbaum, W. A. Love, S. Ozaki, E. D. Platner, C. A. Quarles and E. H. Willen, Phys. Rev. Letters 19, 857 (1967).
19. W. Galbraith, E. W. Jenkins, T. F. Kycia, B. A. Leontic, R. H. Phillips, A. L. Read and R. Rubinstein, Phys. Rev. 138B, 913 (1965).
20. S. P. Denisov, S. V. Donskov, Yu. P. Gorin, A. I. Petrukhin, Yu. D. Prokoshken, D. A. Stoyanova, J. V. Allaby and G. Giacomelli, Phys. Letters 36B, 415 (1971).
21. M. J. Longo and B. J. Moyer, Phys. Rev. 125, 701 (1962).
22. F. Chen, C. Leavitt and A. Shapiro, Phys. Rev. 99, 857 (1955).
23. G. von Dardel, D. H. Frisch, R. Mermod, R. H. Milburn, P. A. Piroué, M. Vivargent, G. Weber and K. Winter, Phys. Rev. Letters 5, 333 (1960).
24. G. Igo, J. L. Friedes, H. Palevsky, R. Sutter, G. Bennett, W. D. Simpson, D. M. Corley and R. L. Stearns, Nucl. Phys. B3, 181 (1967).
25. G. Bellettini, G. Cocconi, A. N. Diddens, E. Lillethun, J. Pahl, J. P. Scanlon, J. Walters, A. M. Wetherell

and P. Zanella, Phys. Letters 14, 164 (1965).

26. G. Bellettini, G. Cocconi, A. N. Diddens, E. Lillethun, J. Pahl, J. P. Scanlon, J. Walters, A. M. Wetherell and P. Zanella, Phys. Letters 19, 705 (1966).

27. G. Bellettini, G. Cocconi, A. N. Diddens, E. Lillethun, G. Matthiae, J. P. Scanlon and A. M. Wetherell, Phys. Letters 19, 341 (1965).

28. F. E. Ringia, T. Dobrowolski, H. R. Gustafson, L. W. Jones, M. J. Longo, E. F. Parker and B. Cork, Phys. Rev. Letters 28, 185 (1972).

29. H. Palevsky, J. L. Friedes, R. J. Sutter, R. E. Chrien and H. R. Muether, Cong. Intern. de Physique Nucléaire 1964, ed. Mme. P. Gugenberger (Éditions du Centre National de la Recherche Scientific, Paris, 1964) Vol. II, p. 162.

30. V. A. Nedzel, Phys. Rev. 94, 174 (1954).

31. N. E. Booth, G. W. Hutchinson and B. Ledley, Proc. Phys. Soc. (London) 71, 293 (1958).

32. J. H. Atkinson, W. N. Hess, V. Perez-Mendez and R. Wallace, Phys. Rev. 123, 1850 (1961).

33. V. S. Pantuev and M. N. Khachaturyan, JETP 15, 626 (1962).

34. G. Bellettini, G. Cocconi, A. N. Diddens, E. Lillethun, G. Matthiae, J. P. Scanlon and A. M. Wetherell, Nucl. Phys. 79, 609 (1965).

35. R. J. Glauber, in Lectures in Theoretical Physics, edited by W. E. Brittin et al. (Interscience, New York, 1959), Vol. I, p. 315.

36. R. J. Glauber, in High Energy Physics and Nuclear Structure (North-Holland, Amsterdam, 1967) p. 311.

37. V. Franco, Phys Rev. Letters 24, 1452 (1970).

38. W. Czyż and L. Leśniak, Phys. Letters 24B, 227 (1967).

39. A. Y. Abul-Magd, Nuc. Phys. B8, 638 (1968).

40. H. Alvensleben, U. Becker, W. K. Bertram, M. Chen, K. J. Cohen, T. M. Knasel, R. Marshall, D. J. Quinn, M. Rohde, G. H. Sanders, H. Schubel and S. C. C. Ting,

Phys. Rev. Letters 24, 792 (1970).

41. P. B. Jones, The Optical Model in Nuclear and Particle Physics (Interscience, New York, 1963).

42. L. Stodolsky, The Inelastic Shielding Effect, Lecture for the Herceg Novi School 1969.

43. G. von Bochmann, O. Kofoed-Hansen and B. Margolis, Phys. Letters 33B, 222 (1970).

44. K. Gottfried and D. R. Yennie, Phys. Rev. 182, 1595 (1969).

45. G. von Bochmann and B. Margolis, Nucl. Phys. B14, 609 (1969).

46. J. Pumplin and M. Ross, Phys. Rev. Letters 21, 1778 (1968).

47. E. W. Anderson, E. J. Bleser, G. B. Collins, T. Fujii, J. Menes, F. Turkot, R. A. Carrigan, Jr., R. M. Edelstein, N. C. Hien, T. J. McMahon and I. Nadelhaft, Phys. Rev. Letters 16, 855 (1966).

48. G. von Bochmann, B. Margolis and C. L. Tang, 30B, 254 (1969).

49. T. K. Fowler and K. M. Watson, Nucl. Phys. 13, 549 (1959).

50. E. F. Parker and L. W. Jones, Technical Report, Dept. of Physics, The University of Michigan, Ann Arbor, Michigan (1969).

51. V. S. Murzin, in Progress in Elementary Particle and Cosmic Ray Physics (Norht-Holland, Amsterdam, 1967) Vol. IX, p. 245.

52. R. Gibbs, AGS Target Group, Private Communication.

53. E. C. Kerr, J. Am. Chem. Soc. 74, 824 (1952).

54. R. J. Corruccini, in Pure and Applied Cryogenics (Pergamon Press, New York, 1966) Vol. 5, p. 80.

55. H. W. Woolley, R. B. Scott and F. G. Brickwedde, J. Res. Natl. Bur. Std. (U. S.) 41, 379 (1948).

56. G. Giacomelli, Total Cross Section Measurements, Progress in Nuclear Physics, Vol. 12, Part 2 (Per-

57. V. Franco, High Energy Neutron-Nuclei Total Cross Sections, preprint, Physics Department and Institute for Nuclear Theory, Brooklyn College, CUNY, Brooklyn, New York

58. J. S. Trefil, Expectations for Particle-Nucleus Cross Sections at Very High Energies and the Hadron Mass Spectrum, preprint, Physics Department, Univ. of Virginia, Charlottesville, Virginia.

59. J. S. Trefil, Predictions for Elastic and Inelastic Nucleon-Nucleus Cross Sections at High Energies, preprint, Physics Department, Univ. of Virginia, Charlottesville, Virginia.

60. L. Jones, Bull. Am. Phys. Soc. 15, 1587 (1970).

61. G. DeMeester, Ph. D. thesis, Department of Physics, The University of Michigan, Ann Arbor, Michigan.

62. D. D. O'Brien. Private Communication.

63. K. Runge. Private communication to L. W. Jones.

64. M. J. Longo. Private communication.

65. J. D. Bjorken and S. D. Drell, Relativistic Quantum Mechanics (McGraw-Hill, New York, 1964).

66. R. Herman and R. Hofstadter, High Energy Electron Scattering Tables (Stanford University Press, Stanford, California, 1960).

67. H. Bethe, Ann. Phys. 3, 190 (1958).

68. G. Cocconi. Private communication to L. W. Jones.